Thermally Boosted Concept for Improved Energy Storage Capacity of a Hydro-Pneumatic Accumulator

by

Fernando Teixeira Tavares

A dissertation submitted in partial fulfillment
of the requirements for the degree of
Doctor of Philosophy
(Mechanical Engineering)
in the University of Michigan
2011

Doctoral Committee:

Research Professor Zoran S. Filipi, Chair
Professor Albert J. Shih
Associate Professor Kevin P. Pipe
Assistant Professor Matthias Ihme

© Fernando Teixeira Tavares
2011

Dedicated to Maria Dulce and Augusto Tavares

ACKNOWLEDGEMENTS

I would like to thank my advisor, Dr. Zoran Filipi, for his help and guidance during my time as a Ph.D. student. I am especially thankful for all the conversations we have had with regards to our research and common interests. Dr. Filipi's research drive has ensured that his students are funded and properly equipped during their graduate studies, which was an immense help towards achieving my doctoral degree. Thank you to my committee members Dr. Matthias Ihme, Dr. Kevin Pipe, and Dr. Albert Shih for their time and valuable feedback on my dissertation. I would also like to thank Bosch Rexroth and Michigan's 21st Century Jobs Fund for providing financial support for my research.

I would like to thank my parents and my sister for their love and support. I am grateful for all the sacrifices that my parents have made in order for me to have good education and life. Also, I would like to thank my extended family, including my parents-in-law and brother-in-law, for their support during my graduate studies. Thank you to my Auto Lab and IOE friends for your help and support during this long research process. A special thanks to Katrina Appell, Rajit Johri, Ashwin Salvi, and Arleigh Waring.

Lastly, I would like to thank my wife, Irina Dolinskaya, who has been a huge source of comfort and help throughout my adult life. Even though we had to live apart during the final period of my graduate studies, she has always found time and ways to help me. Her incredible love and support during the difficult times are the reason that I have been able to cross the finish line.

TABLE OF CONTENTS

LIST OF FIGURES

LIST OF TABLES

LIST OF APPENDICES

ABSTRACT

Hybrid powertrain concepts provide a critical path for improving the fuel efficiency of vehicles. The energy storage capacity plays a critical role in maximizing the hybrid powertrain improvements. This is especially true for hydraulic hybrid vehicles which use a hydro-pneumatic accumulator as the energy storage device. Accumulators have great power density, but low energy density.

This dissertation first presents a fundamental thermodynamic analysis that assesses potential benefits and theoretical limitations of accumulators used as energy storage devices. This analysis suggests that isobaric accumulator operation yields the best possible energy storage capacity. The accumulator should be heated and cooled during the expansion and compression stages, respectively, to achieve isobaric operation. This idealized method of heating and cooling yields significant energy storage improvements, but requires further analysis to determine how this can be accomplished in a practical device.

A thermally boosted accumulator concept is introduced as a feasible means of improving energy storage by using excess heat from the powertrain system to act as a high temperature heat source. A customized one-dimensional computational fluid dynamics model is developed to investigate the effect of low

speed flows on heat transfer between the heat source/sink and gas. Advanced thermodynamic models are used to predict the state of the real gas under high pressure conditions. In addition, a sophisticated metal foam heat exchanger model is incorporated to capture the overall convective heat transfer characteristic.

The analysis of the thermally boosted accumulator indicates that isobaric operation can only be maintained for a brief period of time, after which the process transitions into the isentropic conditions in the constant volume chamber due to poor heat distribution. However, the transition into the isentropic conditions in the constant volume chamber can be avoided with the use of a metal foam connected to the metal shell of the accumulator to increase the localized heat capacity of the system. Ultimately the thermally boosted accumulator simulation indicates that more than 60% improvement can be achieved during high power demands, and that its energy storage capacity and efficiency are decoupled from the power demands of the system.

CHAPTER I

Introduction

Motivation

The energy needs of the world are currently growing at a rapid pace thus accelerating the consumption of the available natural resources. A key contributor to this problem is the transportation system that almost exclusively relies on fossil fuels to power passenger vehicles, buses, and trucks. One of the ways to decrease the energy consumption of the transportation sector is to hybridize vehicles and significantly improve their efficiency. This is possible due to the hybrid vehicle's ability to recover some energy from its braking events, and provide an additional degree of freedom to the powertrain, which leads to optimized engine operation.

Hybrid vehicles can be found in many configurations with electric hybrids being the most popular option. One the main advantages of an electric hybrid vehicle come from the high energy density of the battery. Furthermore, availability of batteries in various shapes and sizes makes their integration into hybrid vehicles a relatively simple task. However, batteries also have a number of disadvantages, such as, high manufacturing cost and low power density. The

power supplied by the battery is limited by its maximum current due to the low maximum operating temperatures. It is possible to address some of these issues by using a different energy conversion option, such as, the hydraulic hybrid powertrain.

In comparison, the advantages and disadvantages of hydraulic hybrids are essentially reversed to those of electric hybrids. Hydraulic hybrids use components that have high efficiency, high power density, and are cheaper to manufacture. However, hydraulic accumulators, which are used as energy storage devices, have low energy density. Hydraulic accumulators also pose a packaging challenge due to their cylindrical shape, and the need to have a sizable reservoir.

The heavy duty automotive industry has started developing hydraulic hybrid powertrains to take advantage of their high power density and low cost. However, the energy storage capacity is a concern when trying to fully utilize the advantages of the hybrid system. To address this problem, we enhance the accumulator energy storage and operation by introducing a thermally boosted concept.

In the next section, we discuss a series hydraulic hybrid powertrain and explain the role of the accumulator in the powertrain. Next, an in-depth analysis of the accumulator operation is performed to recognize the chances for improving this device. An overview of the dissertation is then given, followed by a contributions section.

Nomenclature

$A_0, B_0, C_0, a, b, C, \alpha, \gamma$	BWR constants
C_v	Specific heat capacitance at constant volume
C_v^0	Specific heat capacitance at constant volume for ideal gas
hA_w	Heat transfer coefficient between wall and gas
I	Specific internal energy
m	Mass of gas
$N_1, N_2, N_3, N_4, N_5, N_6, N_7, N_8, y$	Coefficients for the ideal gas specific heat
p	Gas pressure
R	Ideal gas constant
T	Gas temperature
T_w	Wall temperature
v	Gas specific volume
V	Gas volume

Series Hydraulic Hybrid

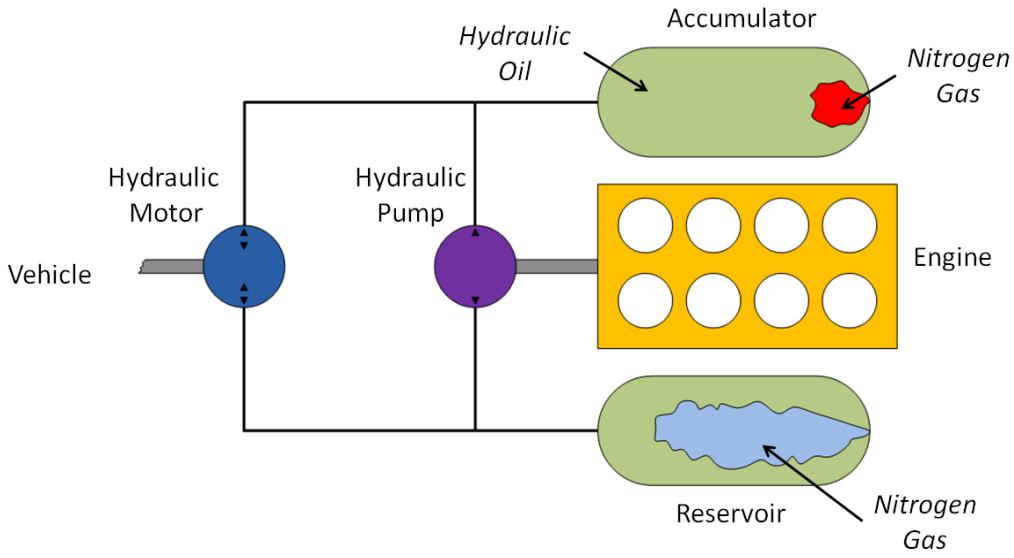

Figure 1: Series hydraulic hybrid configuration with charged accumulator and depleted reservoir

Before discussing the relevance of better energy storage capacity, it is important to understand how a hydraulic hybrid powertrain operates. The main

components of this system are a hydraulic pump, motor, accumulator, and reservoir, as shown in Figure 1, where the hydraulic pump is coupled to an internal combustion engine. The purpose of this device is to convert the mechanical rotational power of the engine to hydraulic power by pressuring the hydraulic fluid into the accumulator from the reservoir. As opposed to a standard transmission, the pump actively controls the engine operation keeping it decoupled from the vehicle operation.

The hydraulic motor is directly connected to the vehicle wheels, and it is responsible for accelerating and decelerating the vehicle. When acceleration is needed, the motor takes hydraulic oil from the high pressure accumulator and uses its energy to propel the vehicle. After the energy is extracted, the hydraulic oil is sent to the reservoir. When the vehicle needs to decelerate, the motor can absorb some of its kinetic energy by pressurizing the hydraulic fluid from the reservoir, and sending it to the accumulator. More information about hydraulic hybrid powertrains can be found in [**1**,**2**,**3**,**4**].

The accumulator and the reservoir regulate the high and low pressure of the system by compressing and expanding the gas. In the case of the accumulator, energy is stored when the gas is compressed, and it is released when the gas expands. The power in and out of the accumulator is proportional to the rate with which the gas compresses and expands. This behavior allows the accumulator to meet high power demands.

One of the drawbacks of the hydraulic hybrid technology is the need to continuously move hydraulic oil between the reservoir and the accumulator.

Since hydraulic oil can be thought of as an incompressible fluid, the reservoir must be approximately equal in volume to the accumulator. Consequently, the improvement of energy storage capacity will not only reduce the size of the accumulator, but it will also reduce the size of the required reservoir. Next, we present an analysis of the accumulator energy storage capacity.

Accumulator Energy Storage Capacity

Energy storage capacity of an accumulator is dictated by the gas thermodynamic properties and heat transfer. When the accumulator energy is being consumed the gas expands causing the pressure and temperature to drop. Likewise, the reverse process occurs during compression increasing the gas pressure and temperature. These gas temperature fluctuations cause heat to be transferred to and from the ambient, which greatly impacts accumulator performance.

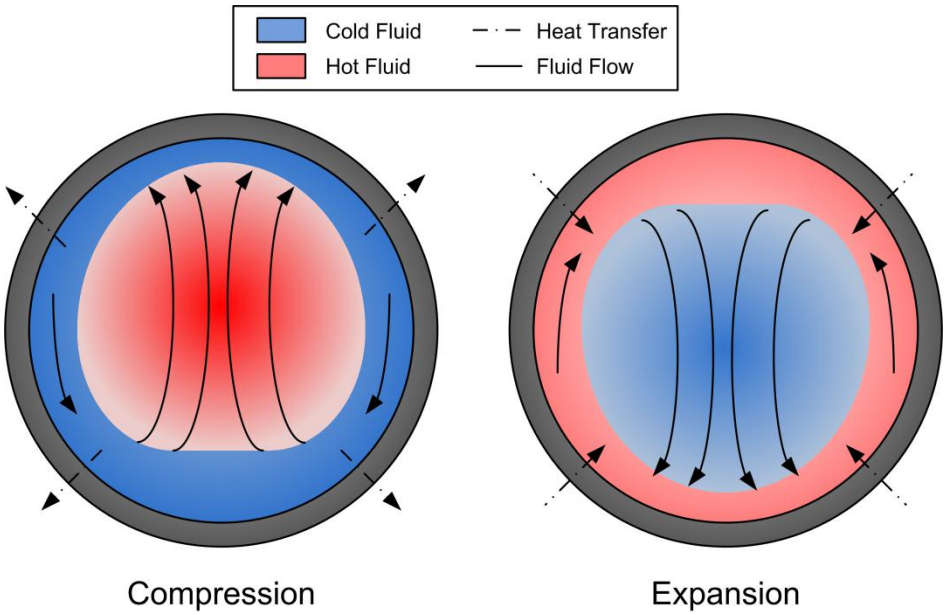

Figure 2: Natural convection heat transfer [5]

Levine and Otis [**5**] have shown that during compression and expansion of the gas, heat is transferred via natural convection, illustrated in Figure 2. In the compression scenario, low thermal conductivity of the fluid causes the gas near the walls to cool down. This temperature drop increases the localized density creating a buoyance effect. Cold fluid then moves along the cylinder towards the bottom while the hot gas in the center moves to the top to replace the dislocated fluid. This effect causes heat to move from the gas to the accumulator walls. The opposite is true for the expansion process.

An experimental thermal time constant correlation was first studied by Pourmovahed and Otis [**6**] in order to predict the heat transfer from an accumulator. An equation derived from numerical results shows that the convective heat transfer coefficient is a function of a modified Rayleigh number, geometric factor, ratio of gas temperature to wall temperature, thermal conductivity and accumulator diameter. Even though the heat transfer coefficient is a function of several parameters that change over time, the authors suggest that good accuracy can be obtained by using a constant value instead. Therefore, we use the constant value approach in our analysis to understand the overall heat transfer behavior.

The algorithm we use for computing the gas process of hydro-pneumatic accumulators was developed by Otis and Pourmovahed [**7**]. This algorithm uses the conservation of energy equation (1.1) to solve for the change in internal energy as a function of heat transfer and work. The convective heat transfer coefficient is estimated based on [**6**]. The gas temperature can be calculated

using the thermodynamic relation equation (1.2) and equations (1.3) and (1.4), which estimate the heat capacity at constant volume of the gas. With the density and temperature now known, the pressure can be estimated with equation (1.5).

$$m\frac{dI}{dt} = -p\frac{dV}{dt} - hA_w(T - T_w) \tag{1.1}$$

$$dI = C_v dT + \left[T\left(\frac{dp}{dT}\right)_v - p\right]dv \tag{1.2}$$

$$C_v = C_v^0 + \frac{6}{T^3}\left(\frac{C_0}{v} - \frac{c}{\gamma}\right) + \frac{3c}{T^3}\left(\frac{2}{\gamma} + \frac{1}{v^2}\right)e^{-\gamma/v^2} \tag{1.3}$$

$$\frac{C_v^0}{R} = \frac{N_1}{T^3} + \frac{N_2}{T^2} + \frac{N_3}{T} + (N_4 - 1) + N_5 T + N_6 T^2 + N_7 T^3 + \frac{N_8 y^2 e^y}{(e^y - 1)^2} \tag{1.4}$$

$$p = \frac{RT}{v} + \frac{B_0 RT - A_0 - \frac{C_0}{T^2}}{v^2} + \frac{bRT - a}{v^3} + \frac{a\alpha}{v^6} + \frac{C(1 + \gamma/v^2)\, e^{-\gamma/v^2}}{v^3 T^2} \tag{1.5}$$

Simulation Parameters	Initial Temperature (K)	Initial Volume (L)	Mass (kg)
Isothermal Operation	300	9.24	3.36
Isentropic Operation	300	15.86	5.76
Standard and Insulated	300	11.34	4.12

Table 1: Accumulator simulation initial conditions

We perform a simulation using SIMULINK based on the equations above to calculate the overall performance of a 30 liter nitrogen accumulator. This simulation replicates the operation of an accumulator by removing and adding energy at a constant rate, with a 10 second wait between the expansion and compression cycles. This accumulator model is cycled until it reaches steady state operation. Another simulation is performed to understand the impact of insulating the gas from the accumulator walls. The simulation initial conditions

are shown in Table 1, and the constraints are: maximum pressure is 400 bar, minimum pressure is 100 bar, and maximum volume is 30 L.

The results of simulations are summarized in Table 2, and they show that natural convection heat transfer (labeled standard accumulator) causes thermal losses to occur leading to a drop in energy storage (work out value). Higher power demands further decrease this value due to higher thermal losses between the expansion and compression cycles. Figure 3 and Figure 4 show how the accumulator pressure and temperature vary as a function of volume. These figures also show the hysteresis effect caused by thermal loss.

Ideal Nitrogen Accumulator	Work In (kJ)	Work Out (kJ)	Efficiency (%)
Isothermal Operation	375.9	375.9	100
Isentropic Operation	271.9	271.9	100
Standard Nitrogen Accumulator (hA_w = 200 W/K)			
Constant Power 10 kW	331.9	264.7	80
Constant Power 60 kW	281.7	238.3	85
Insulated Nitrogen Accumulator (hA_w= 50 W/K)			
Constant Power 10 kW	285.9	264.9	93
Constant Power 60 kW	276.7	266.4	96

Table 2: Accumulator energy storage results for various power and heat transfer scenarios

The insulated accumulator results show that, while thermal losses decrease and efficiency increases, they do not have significant impact on energy storage. By comparing these results, one can conclude that the accumulator with insulation cannot exceed the energy storage of the isentropic process. If the accumulator operates isothermally, the energy storage improvement would vary between 42 to 58%, which is a sizable improvement.

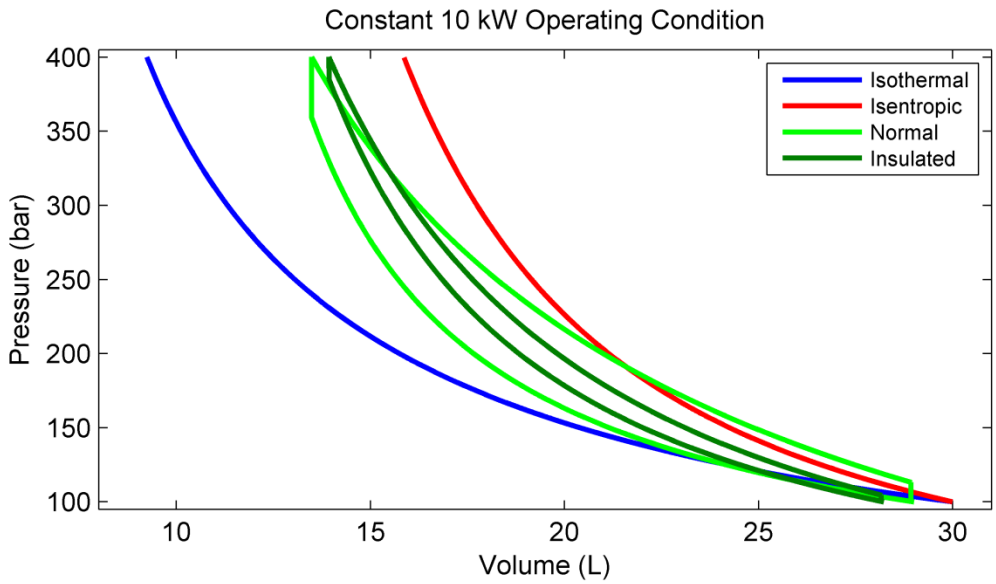

Figure 3: Accumulator bulk pressure distribution versus volume

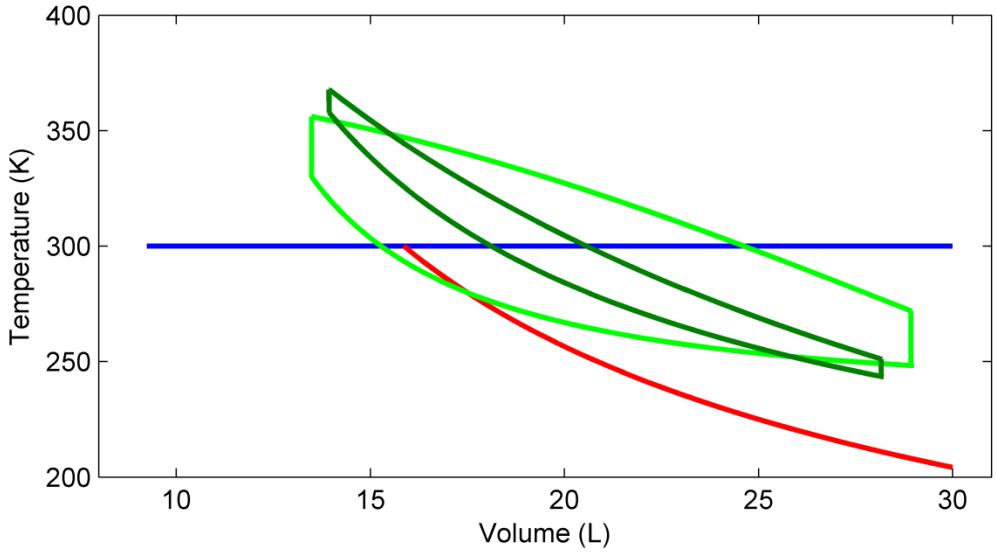

Figure 4: Accumulator bulk temperature distribution versus volume

Dissertation Overview

Chapter II

To begin, we conduct a literature review of the published work on the improvement of the hydraulic accumulator operation. First, we analyze the approach presented by Pourmovahed in [**8**] and [**9**], who suggested using an

elastomeric foam to increase the heat capacity of the accumulator system. The major drawback of this idea is the potential permanent plastic deformation of the foam during the repeated compression and expansion cycles. This requires further analysis to understand the effective heat capacity of the system following a plastic deformation of the foam.

The next concept presented in literature is called “open accumulator” and was suggested by Li et al. [**10**]. This device is focused on improving energy storage by combining hydraulic and pneumatic machines to allow air to be expanded to ambient. The key challenge of the proposed method is creating a device that can successfully harness the gas expansion from 400 to 1 (bar) efficiently. If several devices are used to accomplish this compression ratio, the efficiency of each device would be multiplied to yield a poor total efficiency. Further design improvements and analysis are needed to understand the practicality of open accumulator.

The third idea that we study is to remove the gas from the system altogether and store energy by straining a polyurethane bladder [**11**]. This design has great potential for storing energy at lower pressures. However, the bladder will most likely not be able to contain the hydraulic oil at high pressures due to the very low yield strength of the polymers.

Finally, a patent by Gray and Hellman [**12**] presents a design called the “accumulator engine”. This design is focused on using a heating and cooling network system to extract energy from the engine exhaust. The effectiveness of

this device is not known due to the nature of the patent, suggesting that a more detailed analysis needs to be performed.

Chapter III

In this chapter, we perform a fundamental thermodynamic analysis to understand the theoretical potential of an accumulator. This investigation shows that isobaric operation yields the best possible energy storage capacity. To accomplish this behavior, an idealized heating and cooling strategy is developed to comprehend the theoretical limits of the device. Our simulation results show that isobaric operation cannot be maintained for long periods of time due to heat transfer limitations and the available temperatures for the heat source and sink. Nevertheless, a significant increase in energy storage is observed even if full isobaric operation is not sustained.

To identify the needed heat transfer rates, as well as the temperatures that may be available to act as a heat source, we perform a study using a hydraulic hybrid vehicle simulation. This research shows that power demands from the accumulator during the FTP75 (Federal Testing Procedure) driving cycle do not require extreme rates of heat transfer. Furthermore, exhaust temperatures from diesel engine tests show that high enough temperatures can be obtained.

In addition, we conduct a preliminary heat transfer analysis to understand the heat transfer impact of reducing the accumulator diameter with the intention to create higher fluid velocities. This study is based on engine heat transfer literature and shows that little improvement can be expected.

Lastly, the thermally boosted accumulator concept is introduced as a practical device that may be capable of achieving some of the cooling and heating behavior previously discussed.

Chapter IV

A one-dimensional fluid dynamics analysis must be performed to accurately estimate the gas flow and pressure behavior through the system, which in turn dictates the effectiveness of convective heat transfer from a heat source to the gas in the accumulator. We perform a study considering two possible control volume schemes to determine which one offers the best advantage when modeling the thermally boosted accumulator.

The first approach is a staggered control volume scheme based on the work of Andersen at el. [**13**]. This modeling method is focused on solving the mass and energy conservation equations in one control volume, while the momentum equation is solved using an overlapping control volume. Our implementation of this scheme, presented in Chapter IV, varies from that of Andersen at el. [**13**] as it uses the equations in conservation law form. The staggered control volume scheme provides third order accuracy in space and fourth order accuracy in time using a Runge-Kutta fourth order solver. Due to the staggered nature of the scheme, this implementation is a complex endeavor.

Collocated control volume schemes can also be used to predict gas flow behavior. This is the preferred method of simulation when analyzing the wave action in engine intake and exhaust systems. However, this type of scheme requires special considerations to avoid instability conditions. To overcome this

problem, several methods have been suggested for solving the differential conservation equations simultaneously in space and time. Winterbone and Pearson [**14**] show how Lax-Wendroff and upwind type schemes, as well as Riemann solvers, can be used to model fluid dynamics of a combustion engine. An innovated scheme is proposed in this chapter, which combines a Lax-Friedrichs and a Lax-Wendroff scheme to achieve greater numerical accuracy without the numerical oscillations. Implementing collocated schemes is a simpler task since the conservation equations are solved together for one control volume. The disadvantage of using these schemes is that errors in the conservation of mass, momentum and energy occur across the control volumes with different discretization widths and pipe diameters.

We perform a shock tube simulation to compare the accuracy between collocated and staggered schemes. The exact solution of the sock tube test is found by solving the Riemann problem. These results show that a staggered scheme yields very similar accuracy to an alternating Lax-Wendroff scheme. Due to the conservation errors discussed above, we decide to use the staggered schemes to create the thermally boosted accumulator gas dynamics simulation.

Chapter V

Standard accumulators in hydraulic applications use nitrogen gas as the working fluid. However, the analysis present in this chapter shows that other gases have better properties for the heat transfer applications due to their lower heat capacity. We propose an advanced thermodynamic model to predict the temperature and pressure of the fluid based on its density and internal energy

information. This relationship is derived from the residual dimensionless Helmholtz equation derivatives as shown by Xiang and Deiters [**15**]. Other properties, such as heat capacity, thermal conductivity, speed of sound, and viscosity, are shown as a function of thermodynamic states. We also describe a sophisticated heat transfer model based on the metal foam heat exchanger characteristics presented by Lu et al. [**16**].

Chapter VI

In Chapter VI we discuss our implementation of the work presented in chapters IV and V to create the thermally boosted accumulator model. This model contains two large volumes (constant volume chamber and bladder chamber) connected via a pipe (hot or cold runners) with a metal foam heat exchanger in the middle.

A detailed analysis is presented on the transient characteristics of the system during its initial stage highlighting the brief isobaric operation of the accumulator. Next, steady state results indicate that an isentropic condition in the constant volume chamber eventually prevails and hinders the energy storage capacity due to poor heat distribution.

To improve upon this condition, the accumulator is throttled during expansion in an attempt to create a shock that would cause more fluid to interact with the heat exchanger. However, due to the high frequency of the wave the net flow rate is very small. Dissipation of these waves in the constant volume chamber could cause the temperature to increase, but there are no simple means to accomplish this.

We add a metal foam to the constant volume chamber to improve the localized heat capacity. This approach significantly improves energy storage with a bulk isothermal operating condition. The concept is further improved by connecting the metal foam to the metal shell to add extra heat capacity. This new accumulator design appears not only to improve energy storage, but also provides consistent operation regardless of power demand.

Next, we discuss the heat transfer characteristics, including natural convection between the constant volume chamber metal shell and ambient, convective heat transfer due to mixing, and heat transfer between the fluid in the bladder chamber and ambient. A detailed analysis of each phenomena shows whether they impact the energy storage capacity. The energy storage of the accumulator appears unaffected when incorporating some thermal losses into the model.

Our preliminary analysis assesses the importance of material selection from a heat transfer perspective. In particular, metals with highest conductivity should be selected to create the foam heat exchanger. Metals with low conductivity should be used in the hot runners to reduce the heat transfer between the heat source and other accumulator parts.

Contributions

Intellectual contributions of the dissertation are as follows:

- Fundamental thermodynamic analysis is performed to demonstrate the theoretical limitation of an accumulator.

- One-dimensional computational fluid dynamics model is created to successfully study all aspects of the thermally boosted accumulator design.
- Innovative heat exchanger model is implemented to enable the difficult task of heat transfer for high pressure fluids.
- Advanced thermodynamic models are used to accurately predict the nonlinear behavior of the gas.
- In-depth analysis of the thermally boosted accumulator concept is performed to understand the true potential of the system.

CHAPTER II

Literature Review

The main challenge of improving the energy storage of a hydraulic accumulator comes from the high pressure conditions under which it operates. This section discusses relevant published work that focuses on improving the accumulator energy storage capacity.

Nomenclature

C_f	Foam specific heat capacity
hA_f	Heat transfer coefficient between foam and gas
hA_w	Heat transfer coefficient between wall and gas
I	Specific internal energy
m_f	Mass of foam
m	Mass of gas
p	Gas pressure
r_0	Outer accumulator shell radius
r_i	Inner accumulator shell radius
T	Gas temperature
T_f	Foam temperature
T_w	Wall temperature
V	Gas volume
σ_a	Axial stress

$\sigma_{h,max}$	Maximum hoop stress
$\sigma_{r,max}$	Maximum radial stress

Accumulator Elastomeric Foam in the Bladder

To improve the efficiency and energy storage of a hydraulic accumulator, Pourmovahed et al. [**8**,**9**] suggests integrating an elastomeric foam insert in the accumulator bladder. This approach is meant to increase the system heat capacity due to the high surface area between the porous elastomer and the gas. Thus, heat is quickly transferred between the gas and the foam, while the foam's temperature changes slowly due to its high heat capacity value. In addition, the proposed design is intended to decrease heat transfer to the accumulator walls, since the foam is spread over the majority of the accumulator volume and the natural convection heat transfer (presented in the previous chapter) is impeded.

Two significant drawbacks exist when implementing the approach proposed by Pourmovahed et al. [**8**,**9**]. The first problem comes from the fact that the introduced elastomer occupies portion of the accumulator's volume, which cannot be used by the gas. The second potential problem occurs if the foam is plastically deformed. Pourmovahed [**8**] discusses that frequent compression and expansion of the foam may cause plastic deformation. When this occurs, the plastic will not properly expand during expansion reducing the interaction of gas with the foam.

To investigate the potential of elastomeric foam inserts in the accumulator, we created a bulk accumulator model. The conservation of energy equation (given in Chapter I) is modified to account for the foam's thermodynamics. The

heat transfer rate, hA_f, is assumed to be 3000 W/K due to its high surface area. The heat capacity of the foam is 2.3 kJ/kg-K and the mass is 1.265 kg.

$$m\frac{dI}{dt} = -p\frac{dV}{dt} - hA_f(T - T_f) - hA_w(T - T_w) \tag{2.1}$$

$$m_f C_f \frac{dT_f}{dt} = hA_f(T - T_f) \tag{2.2}$$

Foam Insert Accumulator (hA_w=50 W/K)	Work In (kJ)	Work Out (kJ)	Efficiency (%)	Improvement (%)
Constant Power 10 kW	313.7	306.6	97.7	15.8
Constant Power 60 kW	313.2	296.1	94.6	24.3

Table 3: Accumulator energy storage results using the elastomeric foam

Table 3 gives summary of the results for a foam accumulator simulation confirming that the energy storage and efficiency increase when using the elastomeric foam. Figure 5 illustrates the steady state accumulator pressure operation with a maximum expansion volume of 29 L, since the foam mass will occupy 1 L of accumulator's volume. Figure 6 demonstrates that the foam mass maintains the gas temperature closer to the ambient value of 300 K.

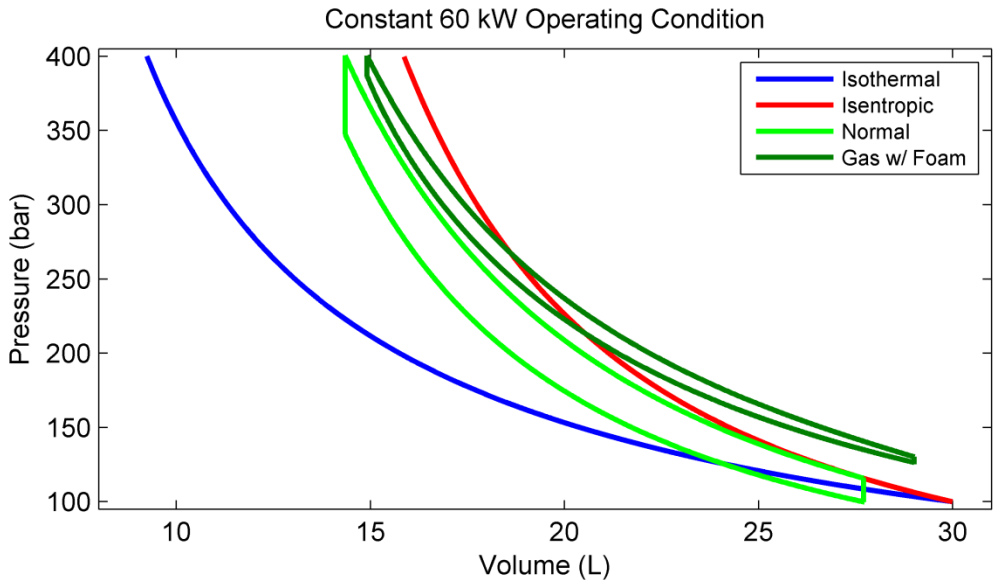

Figure 5: Accumulator with foam pressure comparison

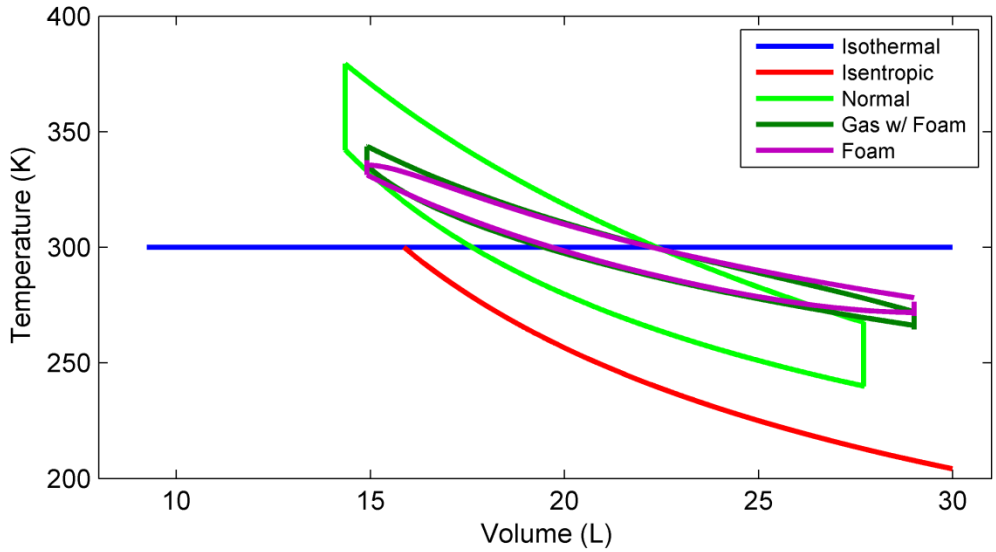

Figure 6: Accumulator with foam temperature comparison

Open Accumulator

The open accumulator design is another method to increase energy storage, which was proposed by Li et al. [**10**]. To understand the operation of this device, consider a fully charged accumulator. In the open accumulator design, this implies that the air occupies the entire volume of the accumulator. When the vehicle needs power, air is released from the accumulator to a pneumatic device that acts as an air motor. This air motor extracts work from the high pressure gas and then releases it to the ambient. Simultaneously, a hydraulic device acting as a pump uses some of the energy from the air motor to create an isothermal condition in the gas. Analogously, when excess energy needs to be stored in the accumulator, the pneumatic device operates as a compressor taking power from the shaft in order to pump the compressed ambient air into the accumulator. In such a case, the hydraulic device acts as a motor to pump fluid from the

accumulator back into the reservoir. Figure 7 illustrates how the pneumatic and hydraulic devices are connected to the open accumulator.

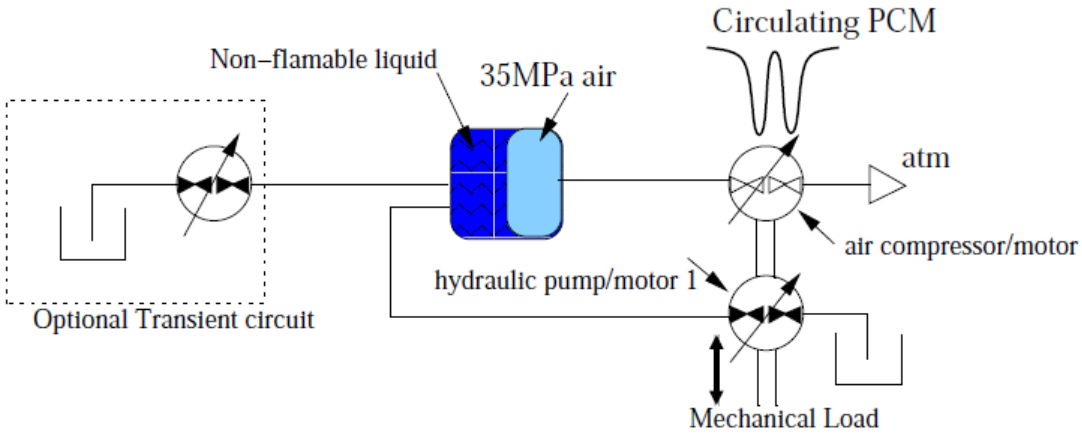

Figure 7: Open accumulator energy storage concept [10**]**

The open accumulator is capable of storing the same amount of energy as a standard accumulator, but with a smaller volume due to its ability to expand and compress the air to and from the atmosphere, respectively. In comparison, the standard hydraulic system needs a larger volume because the expansion of the gas has to be contained. The other advantage of an open accumulator comes from the fact that operating the system isothermally leads to further improvement in energy storage.

For all the benefits that this system can provide, it is not without its drawbacks. Since the open accumulator system is constantly expanding and compressing air between pressure ratios of 1:400, the gas temperature can fluctuate between 1583 K and 56 K [**10**]. These extreme temperatures are more than enough to significantly damage most parts of the pneumatic motor. To mitigate this factor, the compression and expansion of the gas might have to be staged in a series of pneumatic devices, with heating and cooling between the

stages. Li et al. [**10**] suggest using a phase changing material (PCM) to cool and heat the gas between the stages or in the compressor itself. However, depending on the heat transfer rate between the PCM and the gas, the compressor/motor efficiency could vary by 55 % to 90 % [**10**]. Staging pneumatic devices with high efficiencies would still lead to low system efficiency due to the multiplication effect of devices connected in series.

Elastic Accumulator

Pedchenko and Barth [**11**] suggest using a polyurethane bladder to store energy through strain rather than compressing and expanding a gas. The device is initially filled with fluid up to a V_{min} value, which corresponds to a desired pressure, P_{hold}. When energy needs to be stored, fluid flows inside the bladder and expands the polyurethane until the volume of the fluid has reached a value of V_{max}. During this period, the pressure is keep relatively constant since a bubble forms in the bladder creating a pressure rise, shown in Figure 9. Once the bubble starts to propagate, the pressure remains constant at a certain value, illustrated in Figure 10. This process is conceptualized in Figure 8.

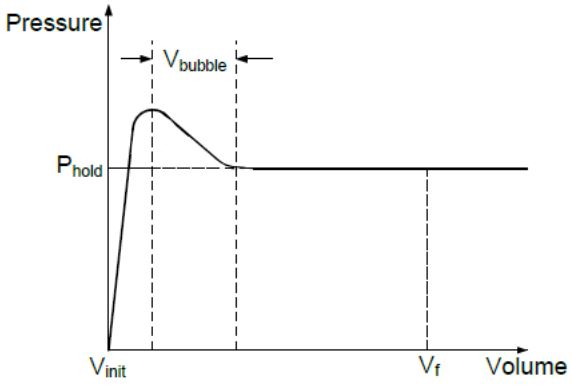

Figure 8: Conceptual pressure volume expansion behavior [11**]**

Figure 9: Bubble formation accompanied by a drop in pressure [11**]**

Figure 10: Subsequent deformation under constant pressure [11**]**

The elastic accumulator has some beneficial features, such as, low cost, design simplicity and good manufacturability. The authors of [**11**] also point out that the material to be used has a volumetric energy density between 25.6 MJ/m^3 and 45.0 MJ/m^3. However, this study does not consider the amount of elastomeric material required in order for the device not to yield under typical operating conditions.

The tensile strength of the material used for the elastic accumulator design is 14.48 MPa. Then, by analyzing the axial and hoop stress equations (2.3) and (2.4) from [**17**] one can observe that the maximum pressure of the accumulator has to be below the tensile strength. These equations are solved for the ratio of the outer over the inner radii of the bladder with the hoops stress, axial stress, and accumulator pressure. The resulting equation (2.6) indicates that the pressure cannot be greater than the tensile strength, regardless of bladder thickness.

$$\sigma_{h,max} = \frac{r_i^2 p}{(r_0^2 - r_i^2)}\left(1 + \frac{r_0^2}{r_i^2}\right) \tag{2.3}$$

$$\sigma_a = \frac{r_i^2 p}{r_0^2 - r_i^2} \tag{2.4}$$

$$\sigma_{r,max} = -p \tag{2.5}$$

$$\frac{r_0}{r_i} = \sqrt{\frac{\sigma_{h,max} + p}{\sigma_{h,max} - p}} \tag{2.6}$$

$$\frac{r_0}{r_i} = \sqrt{1 + \frac{p}{\sigma_a}} \tag{2.7}$$

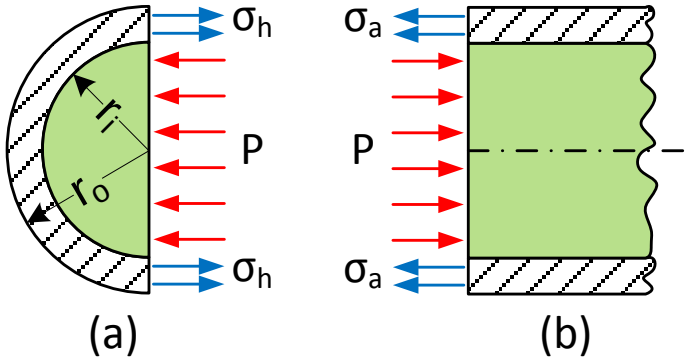

Figure 11: Stresses on a cylindrical pressure vessel: (a) hoop stresses, (b) axial stresses

If the pressure inside the accumulator is below the tensile strength of the polymer, the thickness of the bladder can be found using equations (2.6) and (2.7). Furthermore, using the von Mises yield criteria and a factor of safety indicate that the maximum pressure has to be well below that of the tensile strength. These are important considerations, which ultimately impact the final energy storage potential and accumulator volume. Figure 11 graphically illustrates how the axial and hoops stress relate to the fluid pressure.

Accumulator Engine

The last method for improving accumulator energy storage is given by a patent filled by Gray and Hellman [**12**], referred to as the “Accumulator Engine”. Figure 12 and Figure 13 are shown below and they are used to explain the behavior of this device.

It can be seen that this system contains an engine (30), a pump (36), a motor/pump (34), two accumulators (12/22 and 10/20), and a reservoir (42). When both accumulators are fully charged and power is demanded, one of the accumulators is discharged to provide the vehicle with extra energy. Once that accumulator (for example 10/20) reaches its minimum pressure, the three-way valve (43) closes as the other three-way valve (44) opens. When valve (44) opens, the accumulator (12/20) begins to discharge to continue supplying the vehicle with the needed power.

In the proposed design, engine is used to charge accumulator (10/20), and its exhaust gas is sent through valve (27) into the heat exchanger (26) to heat the discharging accumulator (12/22). Heating of (10/20) is achieved by sending exhaust gas from (30) to the heat exchanger (24) to further increase its operating pressure. In an ideal situation, the authors of [**12**] envision the accumulators to work from point H to point E (shown in Figure 13) during the compression with cooling, from point E to point G while heating at constant volume, and from point G to point J during the expansion and heating.

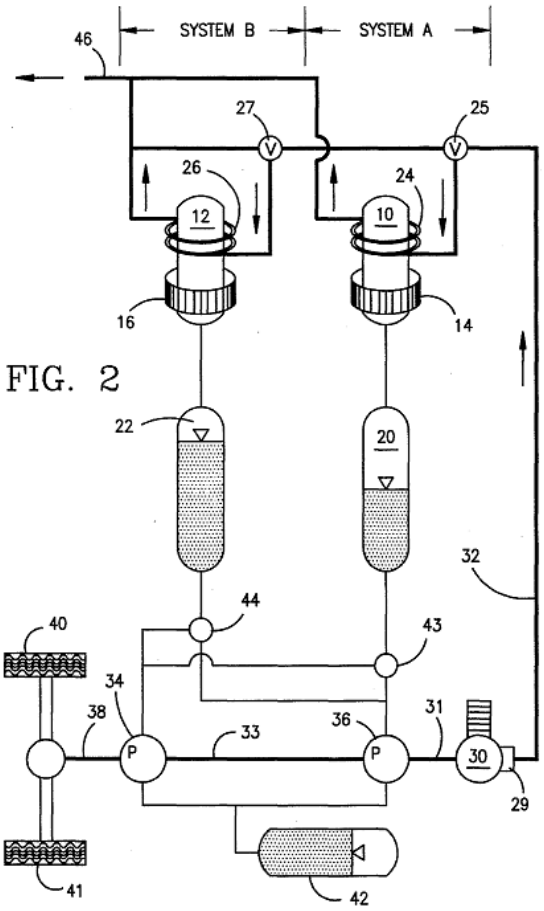

Figure 12: Diagram of an accumulator engine in a series hydraulic hybrid [12**]**

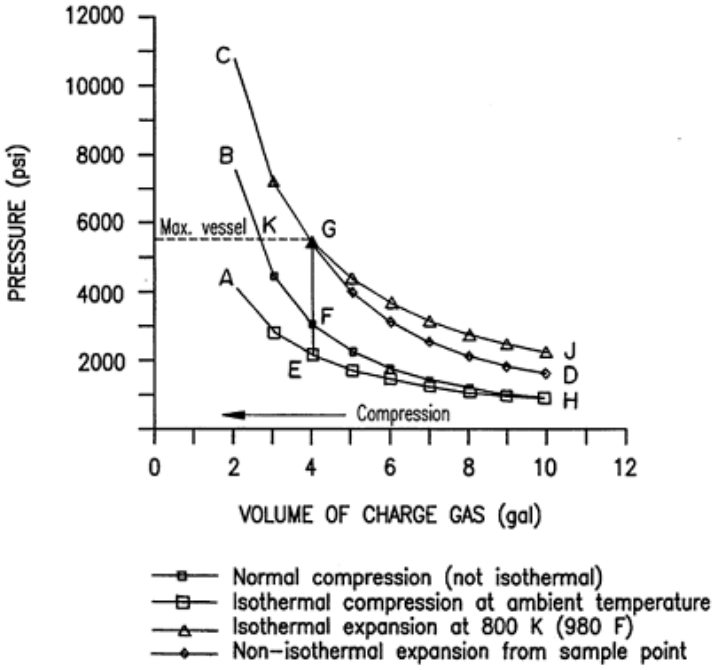

Figure 13: Pressure versus volume curves for nitrogen gas accumulator [12**]**

This is an appealing device as it offers a way to use the exhaust gas from the engine in order to produce work during the accumulator gas expansion process. However, there are some drawback characteristics of the proposed device that the authors of [**12**] do not address. First, the heat transfer rates created by an internal coil used as heat exchanger might not be sufficient. Creating such a heat exchanger might be infeasible since the coil would have to be inserted in and out of the accumulator, and would have to be able to withstand an outside pressure of up to 400 bar. In addition, the system may occupy a large volume due to the need of multiple accumulators to allow the proposed heating and cooling cycles. Finally, no other literature has been found describing an analysis required to evaluate the accumulator engine performance.

CHAPTER III

Fundamental Thermodynamic Study

Nomenclature

a, a', b, c, c_1, c_2	Empirical heat transfer coefficients
C_p	Specific heat capacity at constant pressure
C_v	Specific heat capacitance at constant volume
D	Engine bore diameter
D_h	Hydraulic diameter
I	Specific internal energy
k	Gas thermal conductivity
L	Compressibility
L_r	Fictitious connecting rod length
m	Mass of gas
Nu_c	Complex Nusselt number
Nu_i	Imaginary part of complex Nusselt number
Nu_r	Real part of complex Nusselt number
p	Gas pressure
p_0	Pressure reference values
p_m	Motoring pressure
Pe_ω	Oscillating Peclet number ($\omega D_h^2/4\alpha$)
$\dot{Q}$	Heat transfer rate
$\dot{Q}_w''$	Wall heat flux
R	Ideal gas constant
R_c	Fictitious crankshaft radius

Re	Reynolds number
s	volume/area turbulent core
S_p	Piston speed
$\bar{S}_p$	Mean piston speed
T	Gas temperature
T_0	Temperature reference values
T_H	High heat source temperature
T_L	Low heat sink temperature
T_w	Wall temperature
V	Gas volume
V_0	Volume reference values
w_p	Local mean gas velocity
α	Thermal diffusivity
α_0	Reference diffusivity
γ	Ratio of specific heats
δ	Laminar boundary layer thickness
η	Carnot efficiency
θ	Crankshaft angle
ρ	Gas density
σ	Stefan-Boltzmann constant
ψ	$(1+i)\sqrt{2Pe_\omega}/D_h$
ω	Angular velocity

Concept Formulation

In the previous chapters we discussed how accumulators are used in hydraulic hybrid vehicles, and what researchers have done to improve its energy storage. The next goal is to use this knowledge as a foundation for the creation of a new device that further enhances the energy storage capacity of the accumulator. However, a fundamental thermodynamic analysis must be

performed first to understand what the ideal accumulator operation should be. After analyzing this ideal concept, a device may be created to replicate this operation.

Thermodynamics dictates that the energy stored by a gas is equal to the area under the pressure versus volume curve. By inspecting the pressure volume diagram we can see that isobaric operation would offer the best possible energy storage capacity. The ideal gas equation (3.1) can then provide clues on how to achieve this operation. This equation shows that pressure can be kept constant by changing the temperature of the gas as the volume changes. With a heat source and sink, the temperature of the gas may be controlled by heating and cooling at the appropriate time.

$$p = \frac{mRT}{V} \tag{3.1}$$

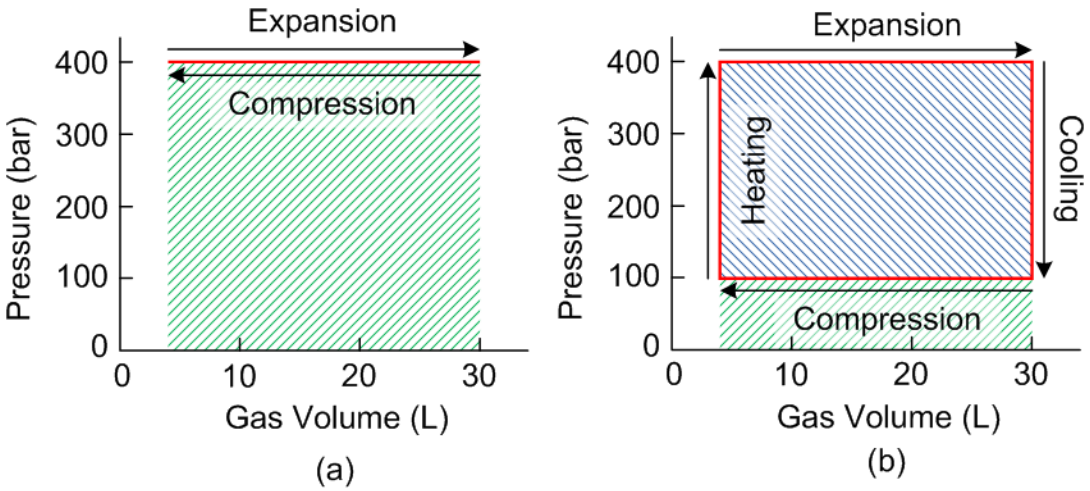

Figure 14: Ideal accumulator operation (a) maximum energy storage, (b) maximum exhaust utilization

Figure 14 shows the two optimal isobaric operating scenarios. In part (a) the isobaric expansion and compression require that the gas be heated during expansion, and cooled during compression. This method of operation leads to

the maximum energy storage possible. The other operation is shown in part (b), and it uses the accumulator to convert heat energy from the high temperature sink into useful work. This process occurs by heating the gas during expansion, cooling the gas to its minimum pressure, compressing the gas at constant pressure while cooling, and heating the gas after compression to the maximum pressure.

These methods of operation can be made possible by using the ambient air as the heat sink, and exhaust gases from the engine as the high temperature heat source. A deeper understanding of the heat transfer mechanism is needed to successfully heat and cool the accumulator.

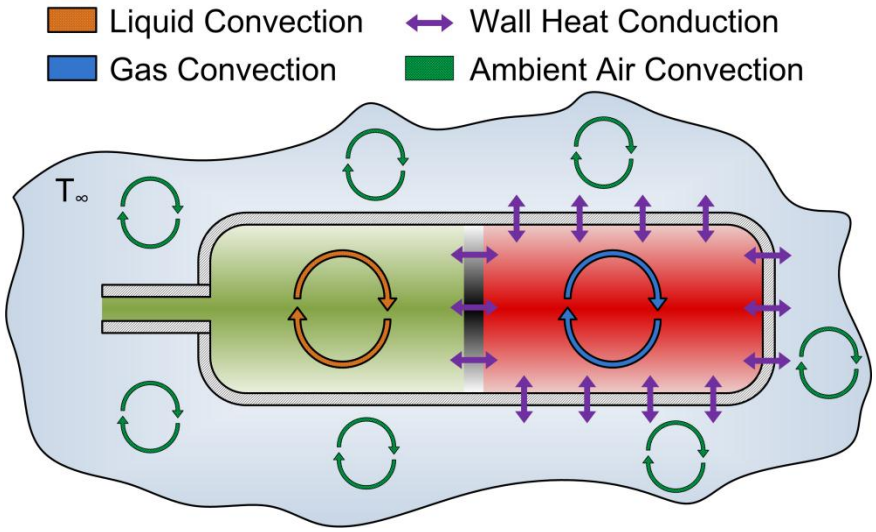

Figure 15: Modes of accumulator heat transfer

Figure 15 shows that heat due to convection travels from the gas to the accumulator walls/piston, if the gas temperature is greater than the wall or piston temperature. Afterwards, the heat passes through the wall and piston by conduction increasing the wall/piston temperature based on its heat capacity. Lastly, heat is absorbed by the hydraulic fluid and ambient air via natural

convection. These heat transfer modes are inadequate to induce isobaric operation.

Heat Transfer Simulation Case Study

Heat transfer plays a critical role in improving the accumulator energy storage capacity, discussed in the previous section. A case study is setup to understand the potential improvement of the accumulator as a function of heat transfer rates and heat sink and source temperatures. This study is realized in SIMULINK by creating an accumulator model and a flow controller shown in Figure 16. The accumulator model was set to have a maximum gas volume of 30 liters, and its initial conditions parameters are shown in Table 4. Equations (1.1) to (1.5), from the Introduction chapter, were used to model the accumulator. The accumulator operation is constrained by limits shown in Table 4.

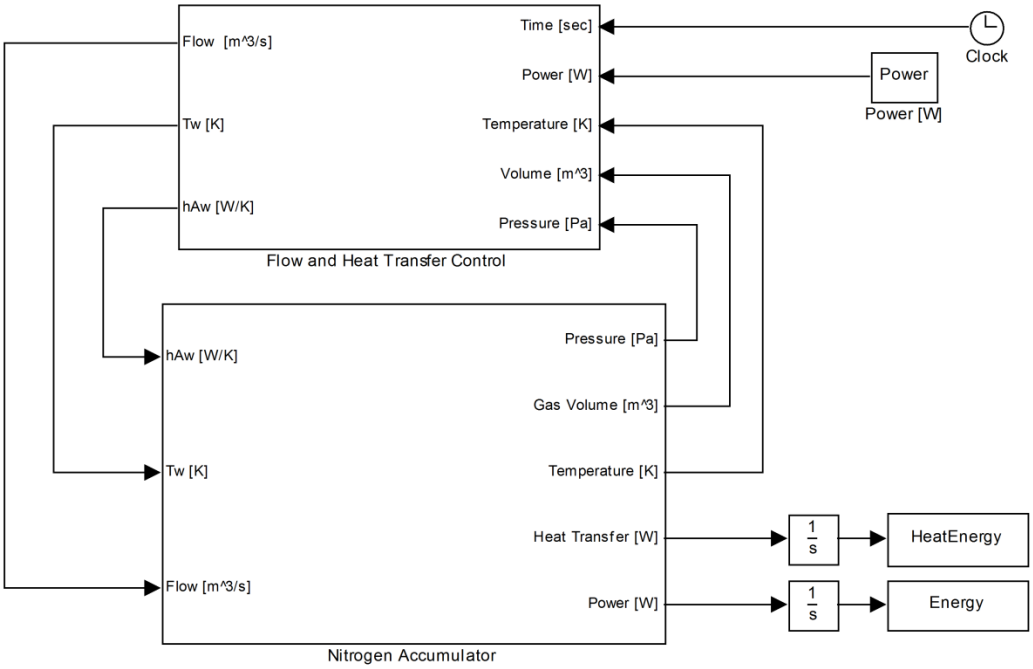

Figure 16: Accumulator thermodynamics and heat transfer SIMULINK model

	Volume (L)	Temperature (K)	Pressure (bar)
Initial Conditions	9	298	400

	Max. Volume (L)	Min. Pressure (bar)	Max. Pressure (bar)
Limits	30	100	400

Table 4: Accumulator model initial conditions and limits of operation

Model Input Parameters						
Power	(kW)	2	5	10	30	60
hA_w	(W/K)	200	600	1200	2100	3000
$T_{w,max}$	(K)	298	500	600	700	800

Table 5: Simulation parameters of the accumulator model

The simulation contains a flow control strategy to operate the accumulator at constant power. Other simulation parameters include constant temperatures for the heat sink and source, and a maximum heat transfer coefficient. These simulation input parameters are show in Table 5. The next paragraphs discuss the accumulator operation in more detail.

In the beginning of the simulation the gas is at its minimum volume and maximum pressure. As the accumulator releases energy a control algorithm, shown in Figure 16, dictates the desired heat transfer coefficient. In doing this, the heat from the temperature source flows into the accumulator to maintain constant pressure. As soon as the maximum heat transfer rate has been reached the controller cannot maintain the desired pressure. As a result, the pressure begins to drop as the flow rate increases to maintain constant power output. Once the gas reaches the limits in Table 4 (maximum gas volume or minimum gas pressure) the controller ceases to extract power from the accumulator.

After a small amount of time, the accumulator begins to be charged at the same power rate as when it was discharged. During this period the controller tries to maintain constant pressure by cooling the gas using a temperature sink, which is at constant ambient temperature of 298 K.

The heat transfer controller uses equations (3.2) through (3.5) to derive equation (3.6), which defines the heat transfer required as a function of power and gas properties for an ideal gas. Using this knowledge a feed forward controller adequately controls the accumulator pressure. The model was allowed to run for several charging and discharging cycles to reach steady state operation.

$$pV = mRT \tag{3.2}$$

$$\frac{dI}{dt} = C_v \frac{dT}{dt} \tag{3.3}$$

$$\frac{dT}{dt} = -\frac{dp}{dt} \cdot \frac{V}{Rm} + \frac{p}{mR} \cdot \frac{dV}{dt} \tag{3.4}$$

$$C_v \cdot \frac{dT}{dt} = -\frac{p}{m} \cdot \frac{dV}{dt} - \frac{\dot{Q}}{m} \tag{3.5}$$

$$-p \cdot \frac{dV}{dt} \cdot \left(\frac{C_v}{R} + 1\right) = \dot{Q} \tag{3.6}$$

Simulation Results

Using the models discussed above, it is possible to run every input scenario shown in Table 5, which lead to 125 simulation results. Some sample

results will be used to illustrate the behavior of the models, since it is not feasible to show the results for all simulations.

The sample simulation chosen has a heat transfer coefficient, $hA_{w,}$ of 600 W/K, a maximum wall temperature T_w of 500 K, and a power demand of 10 kW. Figure 17 shows how the pressure fluctuates as the accumulator power is charged or discharged. The flow rate is also shown in this figure, and it illustrates how the flow increases as the pressure decreases to maintain the constant power demand. The dashed lines in the figure show the steady state cycle used to calculate the overall improvement of the device.

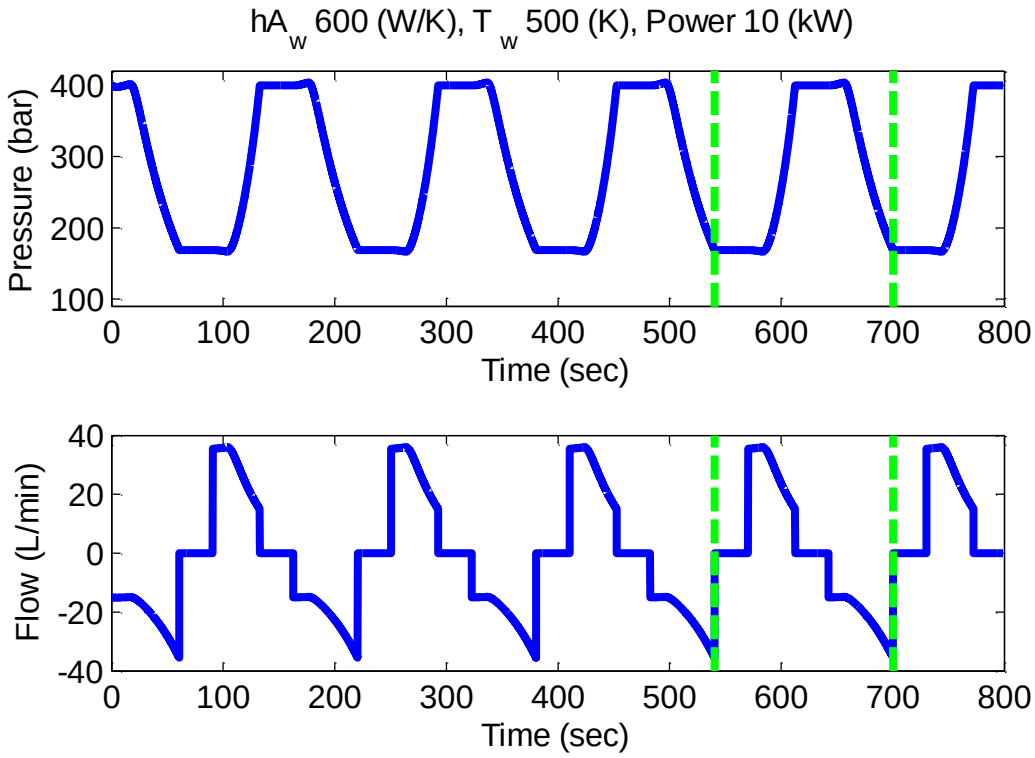

Figure 17: Pressure and flow results over time as the accumulator model is charged and discharged

In Figure 18 the gas and wall temperature correlation is shown. The gas temperature increases and decreases by varying the heat transfer coefficient hA_w to maintain constant pressure. However, once the gas temperature is near the

maximum or minimum value, the desired heat transfer cannot be sustained. As a consequence the pressure is forced to decrease or increase to satisfy the constant power condition.

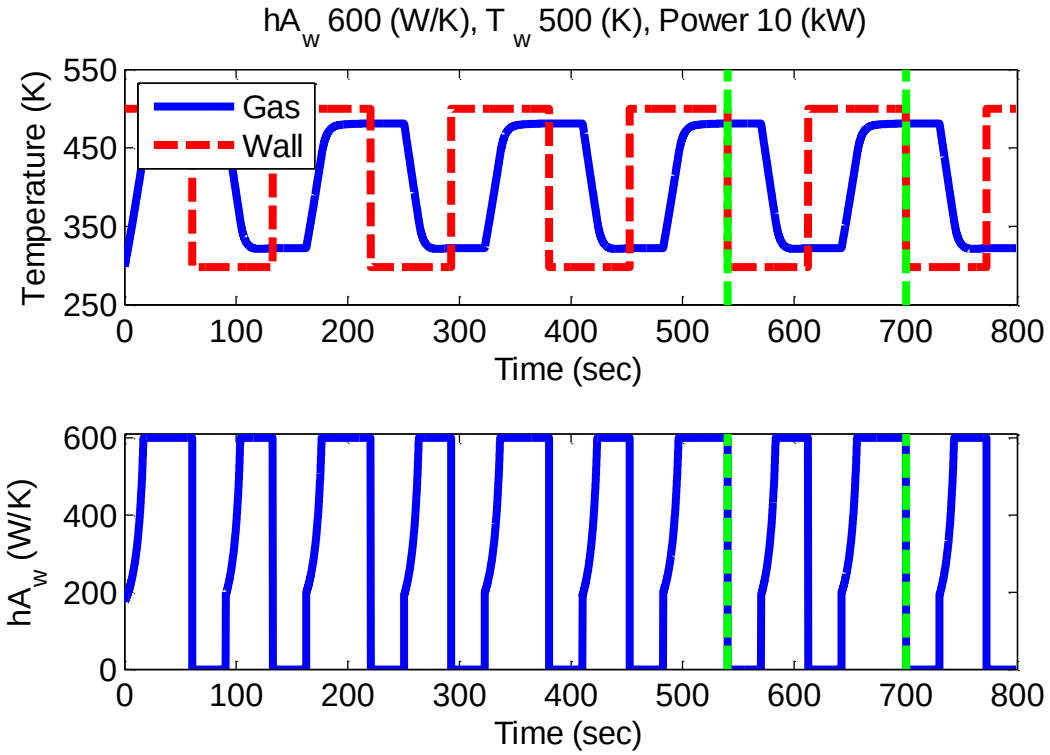

Figure 18: Gas, wall temperature, and heat transfer coefficient over time as the accumulator model is charged and discharged

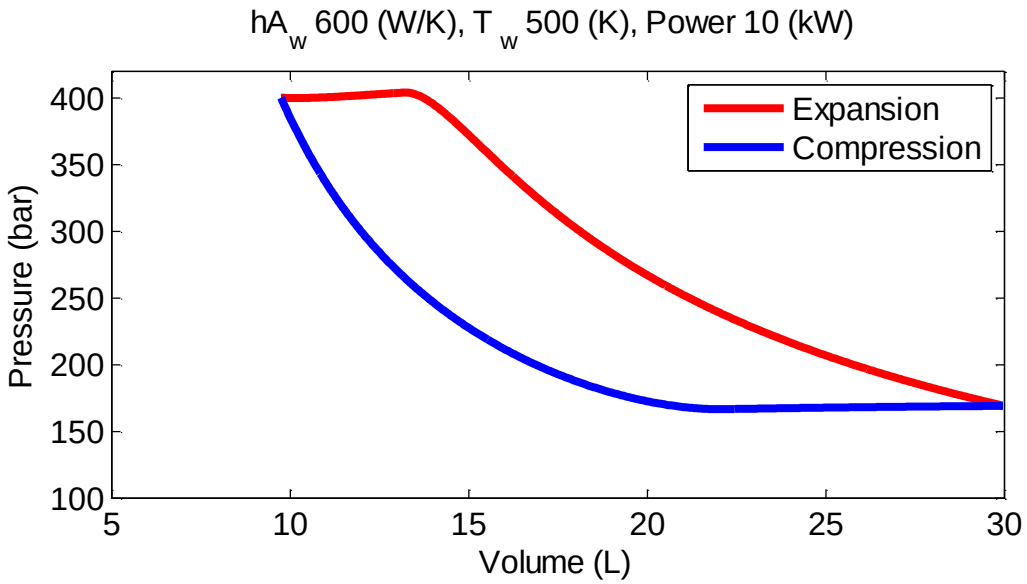

Figure 19: Pressure versus volume accumulator operation

Using these results it was possible to generate a pressure versus volume plot, shown in Figure 19. This figure shows the period in which the pressure is kept constant in both the expansion and compression process. The area under the expansion curve is equal to the amount of energy released by the accumulator. The area under the compression curve shows how much energy it was stored in the accumulator. The difference between these areas corresponds to the amount of energy obtained from the exhaust.

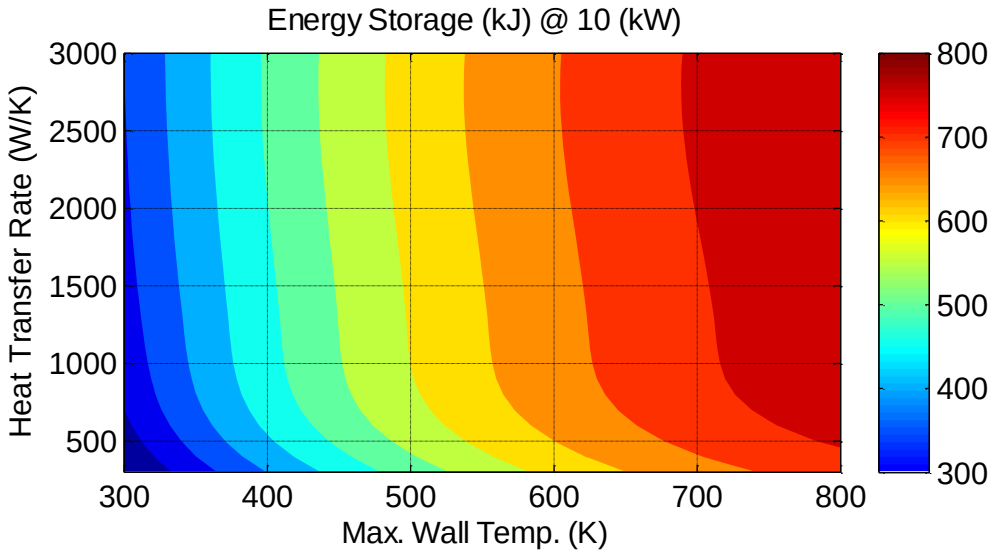

Figure 20: Energy storage as a function of heat transfer coefficient and wall temperature

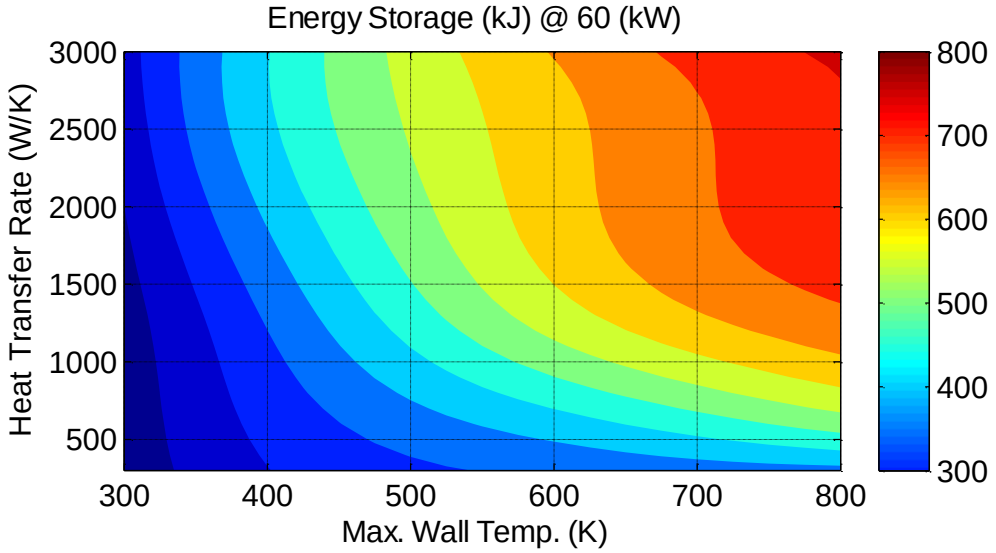

Figure 21: Energy storage as a function of heat transfer coefficient and wall temperature

Now that the accumulator operation behavior has been observed, it is necessary to summarize the results of this study. With this objective Figure 20 is used to determine how the accumulator energy storage potential changes as a function of heat transfer coefficient, and maximum wall temperature. The energy storage value of the accumulator is obtaining by calculating the energy released during steady state operation. This result shows that temperature plays a major role in obtaining the maximum energy storage possible. However, as the accumulator power demand increases the heat transfer coefficient has a more significant impact on the energy storage, as shown in Figure 21. The results for other power demands can be found in APPENDIX A – Energy Storage Results Summary.

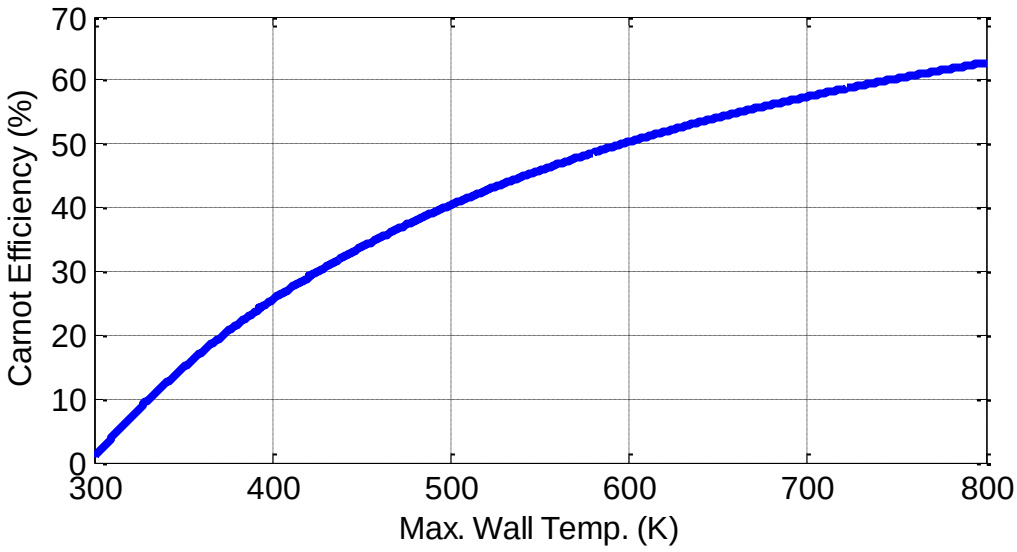

Figure 22: Carnot cycle efficiency as a function of maximum wall temperature

$$\eta = 1 - \frac{T_L}{T_H} \tag{3.7}$$

Another interesting aspect of these results is the ratio of heat which is converted into work. The Carnot cycle efficiency, (3.7), can be used to

understand the maximum efficiency of a thermodynamic cycle such as this. Figure 22 shows how the Carnot efficiency changes with the maximum wall temperature.

The efficiency of heat converted to work is show in Figure 23, and from it we can see that the efficiency does not increase monotonically with temperature. This is due to the fact that as the heat source temperature increases, the gas pressure remains constant for a longer period of time. This behavior causes the accumulator to capture more energy from the vehicle instead of converting heat into work. From these results, it is deducted that a different control strategy may lead to better exhaust heat conversion if desired. Further thermal efficiency results can be found in APPENDIX B – Accumulator Thermal Efficiency for other power demand values.

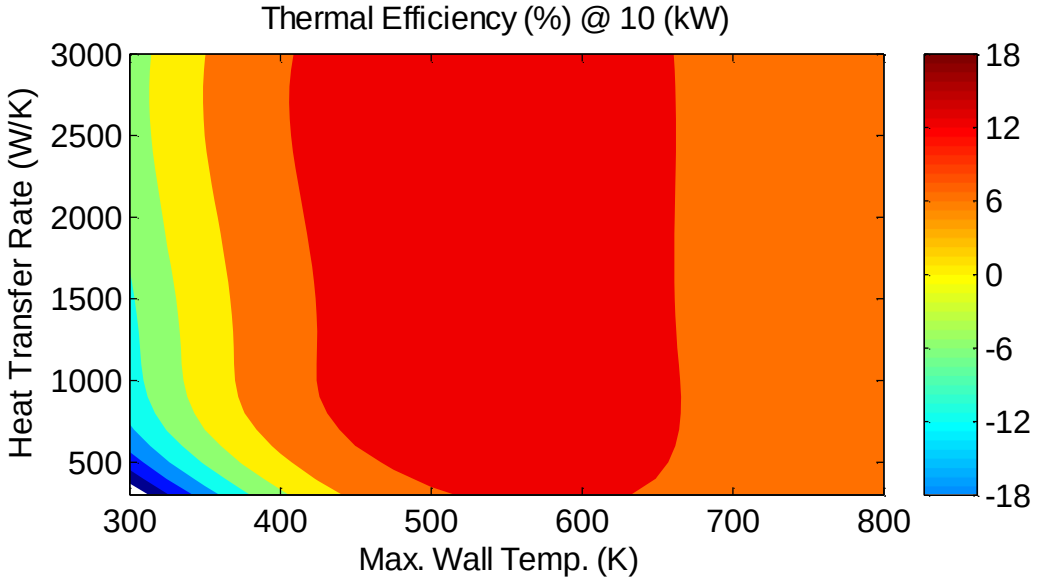

Figure 23: Accumulator thermal efficiency as a function of maximum wall temperature and heat coefficient

The results above show that the accumulator power demand significantly impacts the accumulator behavior. A hydraulic hybrid vehicle simulation is then

used to observe the power levels seen by the accumulator during operation. This simulation features a HMMVV (High Mobility Multipurpose Wheeled Vehicle) series hydraulic hybrid model driving over the FTP75 (Federal Test Procedure) cycle. The results of this simulation are shown in Figure 24, illustrating the velocity profile of the FTP75 driving cycle and the accumulator power over time.

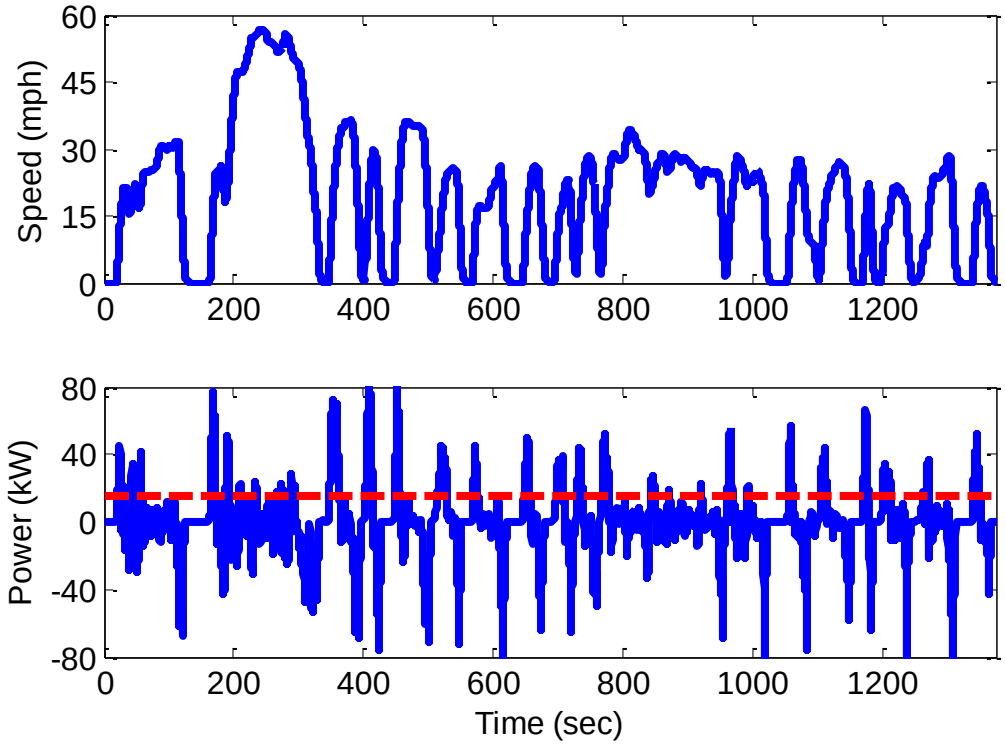

Figure 24: FTP75 driving cycle and accumulator power

The absolute value of the power data, shown in Figure 24, is used to calculate the average power and create the histogram, Figure 25. The total simulation time is 1373 seconds of which 220 seconds were spent idling (not shown in histogram). Of the remaining time, the accumulator spent 738 seconds operating below the average power of 14.98 kW. This means that 70% of the time the accumulator operated below average power. However, more realistic driving cycles may increase the accumulator average power.

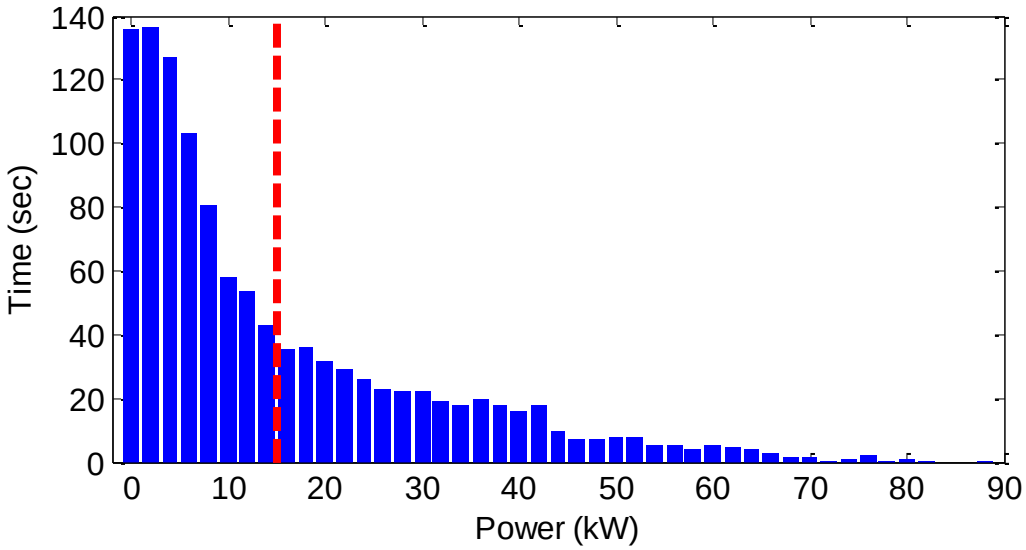

Figure 25: Histogram of accumulator power

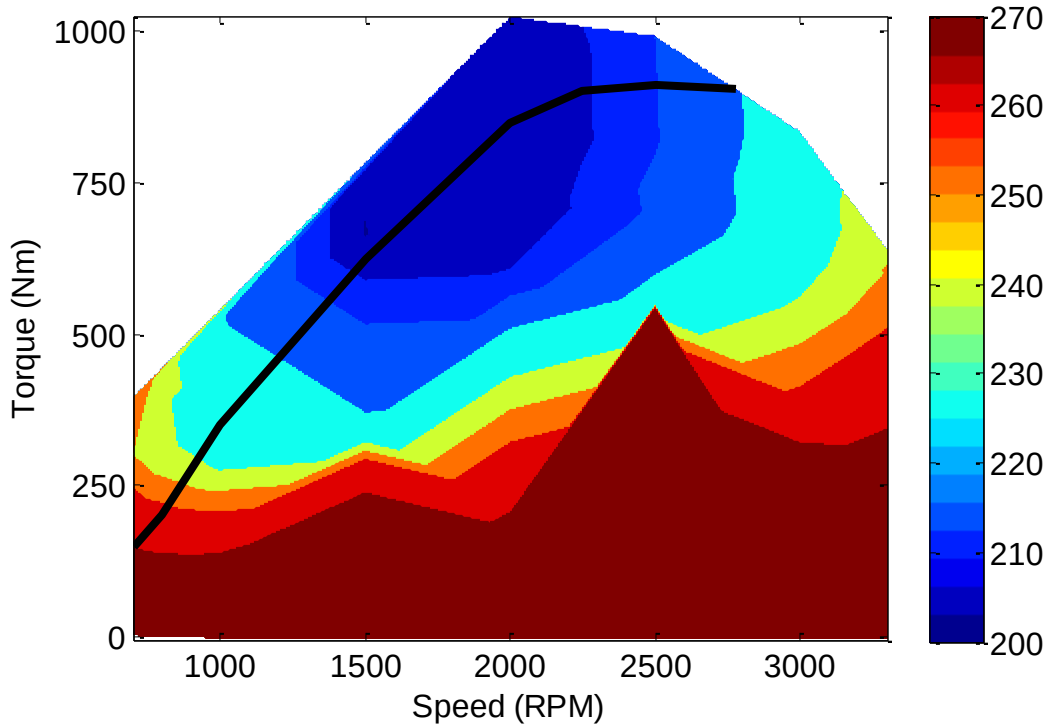

Figure 26: Ford Diesel 6.4L V8 twin-turbo BSFC map (g/kW-hr)

One of the goals of a hybrid vehicle is to operate the engine optimally. In general it means that engine operation should be around the best BSFC (Brake Specific Fuel Consumption) line. The BSFC map of this engine is shown in

Figure 26, along with the best BSFC line. This means that the hybrid powertrain would like to maintain the engine in the area of 210 (g/kW-hr). Figure 27 is created by measuring the exhaust temperature of a Ford Diesel 6.4L V8 twin-turbo engine after the second turbocharger. We can see from this figure that operating temperatures between 550 (K) and 650 (K) can be easily obtained. This means that similar wall temperatures may be possible to act as the heat source.

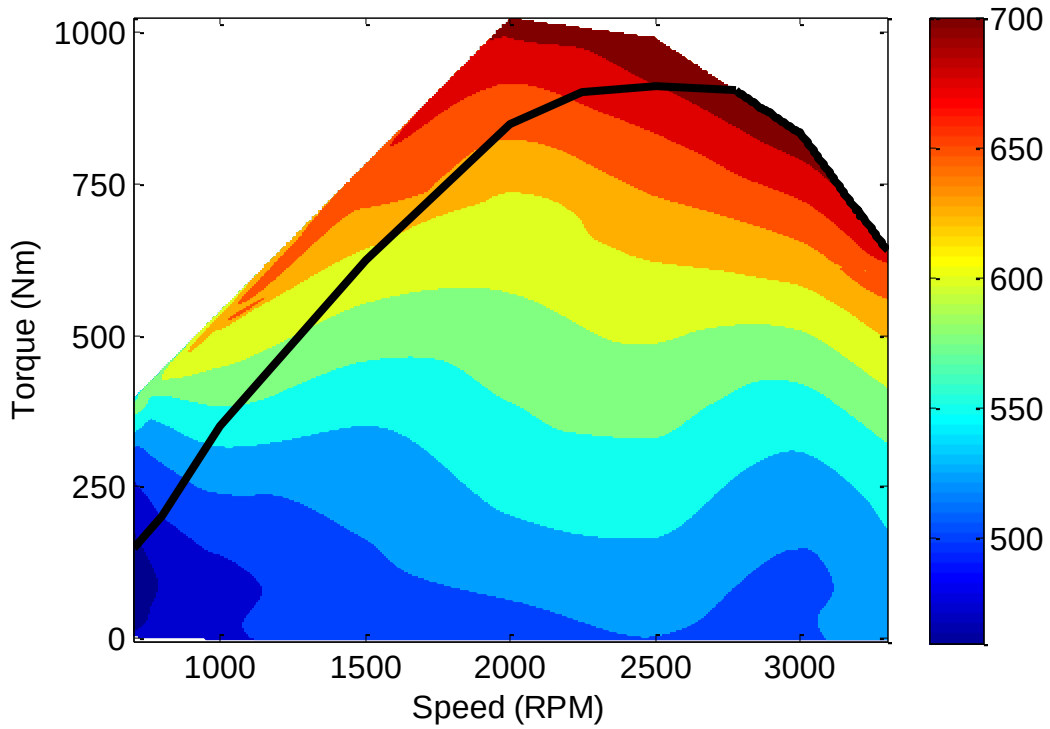

Figure 27: Engine temperature (K) after the second turbo charger

Initial Heat Transfer Analysis

With the wall temperature being dictated by the engine exhaust, the heat transfer remains the only parameter which we can control. The combustion engine literature was studied in an attempt to improve the heat transfer between

the gas and the accumulator wall. The accumulator heat transfer problem can be formulated as an engine heat transfer problem, shown in Figure 28. A fictitious crank shaft is added to relate the piston speed to the angular velocity of an engine.

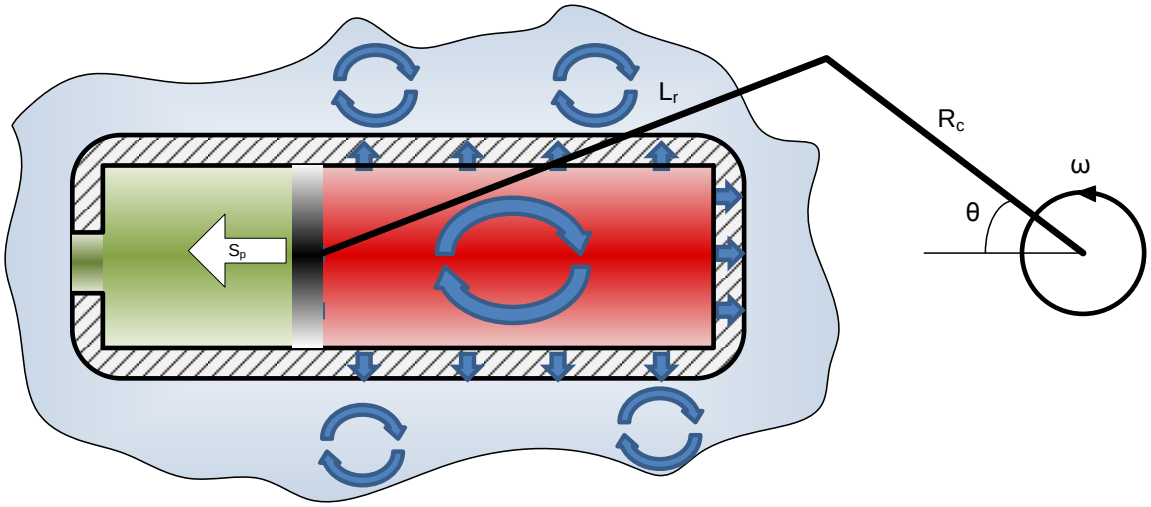

Figure 28: Accumulator representation as an engine analogy

The first heat transfer model was derived by Eichelber [**18**], who used heat transfer equation (3.8) to predict the instantaneous heat flux. However, other experimental work by [**19**] and [**20**] showed that the instantaneous heat flux was out of phase with respect to the temperature difference. This characteristic cannot be captured by using the equation below.

$$\dot{Q}''_w = 0.0105\left(\bar{S}_p\right)^{\frac{1}{3}}(p \cdot T)^{\frac{1}{2}}(T - T_w) \tag{3.8}$$

Annand [**21**] used equation (3.9) to predict the instantaneous heat transfer in an internal combustion engine. This approach cannot be used with accumulators since the coefficients change for every engine, and must be acquired experimentally. Woschni [**22**] attempted to create a universal equation to predict the engine heat transfer, show by equations (3.10), (3.11) and (3.12).

Woschni created this model by applying fundamental heat transfer theorems, and by fitting a large amount of engine data to the equation to calculate its constants. However, these equations cannot be used to predict the accumulator heat transfer due to the use of a mean piston speed ($\bar{S}_p$), which in an accumulator would require several seconds to calculate causing it to not be instantaneous. The second drawback is that the empirical coefficients may not apply to the accumulator, even if c_2 is made zero to remove the combustion heat transfer effect.

$$\dot{Q}''_w = k \cdot \frac{Re^{0.7}}{D} a(T - T_w) - \frac{a'}{\omega} \cdot \frac{dT}{dt} + c\sigma(T^4 - T_w^4) \tag{3.9}$$

$$\dot{Q}''_w = a \cdot \frac{p^{0.8}}{D^{0.2} T^{0.53}} \left(c_1 \bar{S}_p + c_2 \cdot \frac{V \cdot T_0}{p_0 \cdot V_0} (p - p_m) \right)^{0.8} \cdot (T - T_w) \tag{3.10}$$

$$c_1 = 2.28 + 0.308 \cdot \frac{\pi D w_p}{\bar{S}_p} \tag{3.11}$$

$$c_2 = 0.00324 \tag{3.12}$$

Lawton [**23**] modified equation (3.9) to better account for non-steady state heat transfer effects by using a one dimensional simulation approach. This modified equation is shown in (3.13) with the compressibility *L* shown in (3.14). The benefit of this model is that the convection coefficient is no longer a function of gas temperature. However, this model is not capable of prediction instantaneous heat transfer of an accumulator since some constants are based on engine data. Another factor is that the compressibility coefficient is a function of mean piston speed.

$$\dot{Q}_w'' = \frac{k}{D}\{a \cdot Re^b(T_g - T_w) - 2.75LT_w\} \tag{3.13}$$

$$L = (\gamma - 1)\ \cdot \frac{\dot{V}}{V}\sqrt{\frac{D^3}{\alpha_0 \bar{S}_p}} \tag{3.14}$$

Pfriem [**24**] modeled the cylinder space with a one dimensional energy equation in which convection was neglected, as shown in (3.15). In order to account for turbulent convection, the space was divided into two regions. The first region is the boundary layer with no convection, and the second region is the turbulent core. The result of Pfriem's investigation was the creation of the complex Nusselt number (3.16).

$$\frac{\partial T}{\partial t} = \alpha\left(\frac{\partial^2 T}{\partial x^2}\right) + \frac{1}{\rho C_p} \cdot \frac{\partial p}{\partial t} \tag{3.15}$$

$$Nu_c = D_h\psi \cdot \frac{1 - e^{-2\delta\psi} + s\psi\left(1 + e^{-2\delta\psi}\right)}{(1 - e^{-\delta\psi})^2 + s\psi(1 - e^{-2\delta\psi})} \tag{3.16}$$

Kornhauser and Smith [**25**] used Pfriem's results, but changed the turbulence model by using a turbulent thermal diffusivity Pe_ω. As a result equation (3.17) was created to predict the heat flux by using the real and imaginary values of the complex Nusselt number. The complex Nusselt number equations (3.18) and (3.19) were given by [**26**] as a function of the oscillating Peclet number. This approach seems promising in predicting the heat transfer of the accumulator because the equations do not use empirical coefficients and mean values.

$$\dot{Q}_w'' = \frac{k}{D_h}\left[Nu_r(T - T_w) + \frac{Nu_i}{\omega} \cdot \frac{dT}{dt}\right] \tag{3.17}$$

$$Nu_c = \sqrt{2Pe_\omega} \cdot \frac{(1+i)\,tanh(z)}{1 - tanh(z)/z} \tag{3.18}$$

$$z = (1+i)\sqrt{Pe_\omega/8} \tag{3.19}$$

A model was then created to predict the heat transfer of an accumulator designed to induce convection. The induction of convection was possible since the accumulator length and diameter were changed to create turbulence. Furthermore, the accumulator piston speed was used to calculate the equivalent angular velocity, as shown in equation (3.20) and Figure 28.

$$S_p = -\left(R_c \cdot sin(\theta) + \frac{R_c^2\, sin(\theta)\, cos(\theta)}{\sqrt{L_r^2 - (R_c \cdot sin(\theta))^2}}\right)\omega \tag{3.20}$$

Results from this simulation showed that none of the heat transfer models were able to predict the instantaneous heat transfer. We believe this case since the equations were designed to predict the instantaneous heat transfer at constant angular speed. This assumption is acceptable for engines and compressors since each compression and expansion cycle occurs several times faster than the dynamic response of the system (i.e. in the case of a vehicle). The behavior of the accumulator is the complete opposite as the piston speed will change drastically over a compression/expansion cycle.

Accumulator Redesign

The standard accumulator design will need to be changed to create the thermally boosted accumulator. This is the case since controlling the heat transfer of a normal accumulator will be difficult since the wall temperature will

have to be regulated as the gas expands and compresses. Heating the accumulator wall may prove to be impossible due to the high heat capacity of the metal body, and a safety issue might arise from thermal stresses.

The conceptualization of the thermally boosted accumulator is show in Figure 29. The left chamber contains a bladder that traps the gas, and it serves as a barrier between the hydraulic oil and the pressurized gas. On the other side, a cylinder houses the remaining gas. When energy is needed from the accumulator, the gas should flow from the right cylinder to the left chamber via the upper connection. This is possible by opening the upper control valves to allow the gas to pass through the heat exchanger. As this occurs the gas is heated, and as a result the pressure can be somewhat controlled. If the energy needs to be stored, the opposite operation is true. In this scenario the gas will flow from the right chamber towards the right cylinder thru the bottom connection by opening the appropriate flow valves.

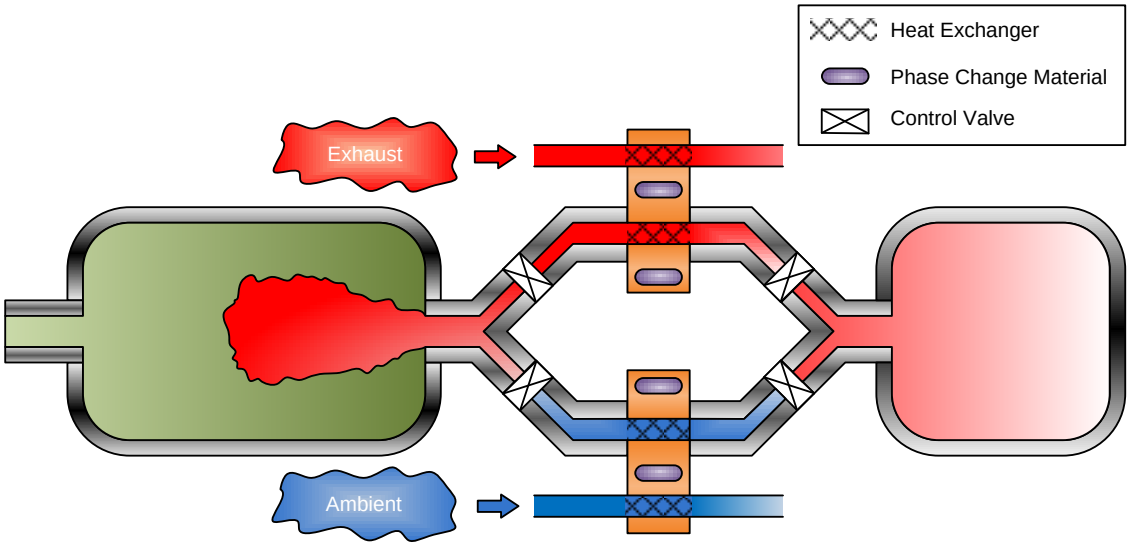

Figure 29: Thermally boosted accumulator conceptualization

To make the device as efficient as possible, it is necessary to continually heat and cool the respective heat exchangers to ensure that high and low temperatures are available when expanding or compressing the gas. For this to work a phase change material will be needed to maintain the heat exchanger at a desired temperature.

The intellectual contribution of this study will be to develop an understanding into how much improvement the thermally boosted accumulator will have. To achieve this goal, a one dimensional gas dynamics model will be used to calculate the speed of the fluid, which can then be used to estimate the heat transfer rate. In addition, the results will provide guidance for designing a practical device, and in particular the connecting passage.

CHAPTER IV

Fluid Dynamics Models

Introduction

In the previous chapter we discussed how energy storage may be improved by heating and cooling the gas. To validate this point, bulk models were used to quantify the maximum possible improvement with respect to the heat source temperature and heat transfer quantities. The next step is to develop of a more complex and detailed model. This additional level of complexity is obtained with the use of Computational Fluid Dynamics (CFD) schemes to better predict the heat transfer rates and the motion of the gas. These schemes will also be tailored to use real gas equations of state. The staggered and collocated control volume schemes are analyzed to determine the best approach of modeling the thermally boosted accumulator. Both schemes have positive and negative attributes, and they will be discussed in more detail in the sections below.

Nomenclature

A	Cross sectional area
a	Gas speed of sound
A_i	Cross sectional area at control volume *i*
a_0, a_1, a_2, a_3	Interpolation constants
a_i^n	Gas speed of sound at time step *n* and control volume *i*
$A_{ref,j}$	Reference cross sectional area at control volume *j*
$a_{rl,j}$	Rectilinear acceleration at control volume *j*
$\boldsymbol{C}$	Source vector
$\boldsymbol{C}_i^n$	Source vector at time step *n* and control volume *i*
c_{max}^n	Maximum wave speed at time step *n*
C_v	Specific heat capacity at constant volume
D	Pipe diameter
E	Gas energy
e	Gas specific energy
E_i	Gas energy at control volume *i*
$\boldsymbol{F}$	Flux vector
f	Frictional constant
$F_{AD,j}$	Artificial dissipation force at control volume *j*
$F_{f,j}$	Frictional force at control volume *j*
$\boldsymbol{F}_i^n$	Flux vector at time step *n* and control volume *i*
f_k	Gas state value (ρ, u, I) at node *k*
$F_{p,j}$	Net pressure forces at control volume *j*
$F_{r,j}$	Reaction force at control volume *j*
$\hat{f}_p(.)$	Gas pressure function
$\hat{f}_T(.)$	Gas temperature function
I	Gas specific internal energy
I_i	Specific internal energy at control volume *i*
m	Gas mass
m_i	Gas mass at control volume *i*
p	Gas pressure

$\Delta p_{f,j}$	Frictional pressure drop at control volume *j*
p_i	Gas pressure at control volume *i*
$\tilde{p}_j$	Estimated pressure at control volume *j*
$p_{mean,j}$	Mean gas pressure at control volume *j*
$\dot{Q}$	Rate of rate in
$\dot{Q}_i$	Rate of heat in control volume *i*
R	Ideal gas constant
T	Gas temperature
t	Time
T_i	Gas temperature at control volume *i*
Δt	Discrete time step
u	Gas velocity
u_i^n	Gas velocity at time step *n* and control volume *i*
V	Control volume
V_i	Control volume at control volume *i*
$\boldsymbol{W}$	State vector
w	Gas mass flow rate
$\dot{W}$	Rate of work out
w_i	Gas mass flow rate at control volume *i*
$\dot{W}_i$	Rate of work out of control volume *i*
$\boldsymbol{W}_i^n$	State vector at time step *n* and control volume *i*
Δx	Control volume length
Δx_j	Control volume *j* length
γ	Ratio of specific heats
ξ	CFL number
$\tilde{\mu}_1, \tilde{\mu}_2$	Dissipation coefficients
ρ	Gas density
ρ_i	Gas density at control volume *i*
Υ	Momentum equation forces
Φ	Gas momentum
Φ_j	Gas momentum at control volume *j*

Courant-Friedrichs-Lewy Stability Criterion

Before starting the discussion on how to create CFD models, we must first discuss the Courant-Friedrichs-Lewy stability criterion. This criteria was created by Courant et al. [**27**] and its purpose is to constrain the simulation time step as a function of the mesh size and the instantaneous wave speed. This can be seen in the equations below from [**14**]. The variable ξ is the Courant, or CFL, number and it serves as a safety factor since the wave speeds in non-homentropic flows (flows in which the entropy level varies) are not constant. Using a value of $\xi > 1$ can result in inaccurate simulations and/or instabilities.

$$\Delta t = \xi \frac{\Delta x}{c_{max}^{n}} \tag{4.1}$$

$$0 < \xi \leq 1 \tag{4.2}$$

$$c_{max}^{n} = \max_{i}\{|u_i^n| + a_i^n\} \tag{4.3}$$

Staggered Control Volume Schemes

In Figure 30 the staggered control volume mesh is shown, which is used to formulate the CFD algorithm similar to the one described by Andersen at el. [**13**]. The solid line control volumes represent the properties of the fluid with respect to mass and energy conservation equation, with the center of the control volume being represented by the "*i*" index. The dashed line control volume represents the momentum property of the fluid with the "*j*" index at the center of this control volume.

Staggered meshes are used to calculate the velocity of the fluid at the boundaries of the “i” control volume to obtain a stable prediction of the flux. The properties of the fluid can then be interpolated to find the values at the boundaries of the control volumes. Three variables (mass, momentum, energy) are used as the states of the fluid, and their relationship to one another is defined by the conservation equations.

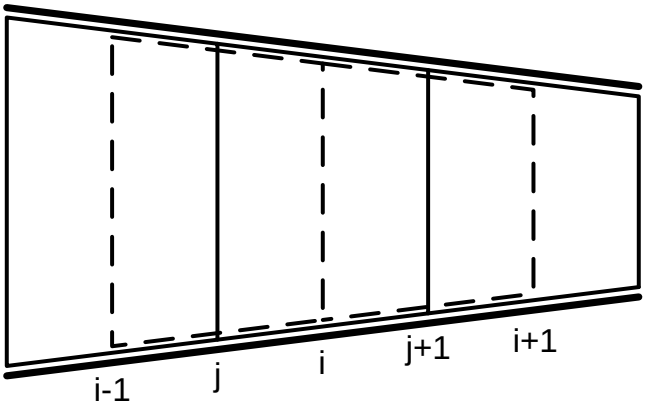

Figure 30: Staggered control volume meshes

The difference between the method of [**13**] and the one we present below is that the conservation equations are solved for mass, momentum and energy (conservative variables) instead of density, velocity, and temperature (non-conservative variables). In the non-conservative approach the velocity and temperature derivatives are a function of other derivatives, which increases the complexity of the solution. Furthermore, Andersen at el. sets the change in energy equal to the change in internal energy of the fluid in order to stabilize the temperature solution across area discontinuities. This assumption is not needed in the conservative approach since velocity derivatives do not manifest in the conservation of energy equation.

The density, velocity and specific internal energy of the fluid still need to be calculated using equations (4.4), (4.6) and (4.7). Once the density and specific internal energy variables are known the temperature and pressure of the gas can be calculated based on the real gas equations of state (see next chapter). The values for density, velocity and specific internal energy at the boundary of control volumes can be calculated using interpolation methods (discussed in the Interpolation Procedure section below). The temperature and pressure variables should not be interpolated as they are calculated based on the density and specific internal energy variables.

$$\rho_i = m_i / V_i \tag{4.4}$$

$$m_j = \rho_j \cdot V_j \tag{4.5}$$

$$u_j = \Phi_j / m_j \tag{4.6}$$

$$I_i = \frac{E_i}{m_i} - \frac{u_i^2}{2} \tag{4.7}$$

$$T_i = \hat{f}_T(\rho_i, I_i) \tag{4.8}$$

$$p_i = \hat{f}_p(\rho_i, T_i) \tag{4.9}$$

Conservation of Mass

The conservation of mass equation is solved by calculating the change in mass inside control volume "*i*" over time by estimating the mass flow in or out of the volume. In equation (4.10) the density of the fluid is calculated at the boundaries using interpolation. The mass flow rate at the boundary is calculated by using the density, velocity and cross sectional area at that surface.

$$\frac{dm_i}{dt} = -\rho_{j+1}A_{j+1}u_{j+1} + \rho_j A_j u_j \tag{4.10}$$

Conservation of Energy

The change in energy has to be calculated for the "*i*" control volume, and to accomplish this we must establish the conservation of energy principle. Equation (4.11) shows that the change in energy is a function of heat transfer into the control volume, work done by the control volume, and the flux of energy in and out of the control volume. The energy flux terms now contain a new variable, *w*, which represents the mass flow rate in and out of the control volume shown in equation (4.12).

$$\frac{dE_i}{dt} = \dot{Q}_i - \dot{W}_i - w_{j+1}\left(I_{j+1} + \frac{u_{j+1}^2}{2} + \frac{p_{j-1}}{\rho_{j-1}}\right) + w_j\left(I_j + \frac{u_j^2}{2} + \frac{p_j}{\rho_j}\right) \tag{4.11}$$

$$w = \rho \cdot A \cdot u \tag{4.12}$$

Conservation of Momentum

The conservation of momentum equation is solved over the "*j*" control volume. This is required since accurate velocities are critical in predicting the correct flux in and out of the "*i*" control volume. By defining a momentum variable as Φ, equation (4.13) shows that the change in momentum is a function of the frictional force F_f, the net pressure force F_p (due to a change in pressure across the control volume), the reaction force at the wall F_r, the rectilinear acceleration of the control volume a_{rl}, and the flux terms containing the speed and mass flow rate variables.

$$\frac{d\Phi_j}{dt} = F_{f,j} + F_{p,j} + F_{r,j} - m_j \cdot a_{rl,j} - u_i \cdot w_i + u_{i-1} \cdot w_{i-1} \tag{4.13}$$

The friction force can be thought of as a pressure drop across a duct or pipe in the direction of the flow (equation (4.15)), and the pressure drop can be expressed by equation (4.14) [**28**]. The friction factor can be found by using the Moody diagram first suggested in [**29**].

$$\Delta p_{f,j} = f \cdot \rho_j \cdot \frac{\Delta x}{D} \cdot \frac{u_j^2}{2} \tag{4.14}$$

$$F_{f,j} = -\frac{u_j}{|u_j|} \cdot \Delta p_{f,j} \cdot A_{ref,j} \tag{4.15}$$

$$F_{p,j} = p_{i-1} A_{i-1} - p_i A_i \tag{4.16}$$

$$F_{r,j} = \tilde{p}_j \cdot (A_i - A_{i-1}) \tag{4.17}$$

$$\left(p_{i-1} + \rho_j \frac{u_{i-1}^2}{2}\right) - \left(p_i + \rho_j \frac{u_i^2}{2}\right) = \frac{u_j}{|u_j|} \Delta p_{f,j} \tag{4.18}$$

$$\tilde{p}_j = p_i + \rho_j \frac{u_i^2}{2}\left(1 - \frac{A_i}{A_{i-1}}\right) + \frac{\frac{A_{ref,j}}{A_i} - 1}{\frac{A_i}{A_{i-1}} - 1} \cdot \frac{u_j}{|u_j|} \Delta p_{f,j} \tag{4.19}$$

$$\tilde{p}_j = p_{i-1} + \rho_j \frac{u_{i-1}^2}{2}\left(1 - \frac{A_{i-1}}{A_i}\right) + \frac{1 - \frac{A_{ref,j}}{A_i}}{1 - \frac{A_{i-1}}{A_i}} \cdot \frac{u_j}{|u_j|} \Delta p_{f,j} \tag{4.20}$$

The reaction force on the wall is estimated using equation (4.17). The authors of [**13**] suggest that $\tilde{p}_j$ should not be treated as the pressure value at "j" since this will not reflect the pressure drop due to friction. To find the correct value Andersen et al. [**13**] suggest using the conservation of energy equation in the steady state form for incompressible fluids, which reduces to the Bernoulli

equation shown in (4.18). Care must be taken when using the $\tilde{p}_j$ equations because the squared velocity terms can cause instabilities over flow area discontinuities. To avoid this undesirable condition [**13**] suggest that equation (4.19) be used when $A_i \geq A_{i-1}$ and equation (4.20) when the opposite is true.

Artificial Dissipation

The use of artificial dissipation in the conservation of momentum equation has been suggested as a method of reducing oscillations due to numerical errors in the scheme [**14**]. Andersen et al. [**13**] further suggest that artificial dissipation can be used to reduce the impact of acoustic waves, which can lead to a reduction of the computational time step. To accomplish this equation (4.21) can be modified by incorporating the dissipation force in equation (4.13). The $\tilde{\mu}$ coefficients below are the dissipation constants, which should be tuned depending on the application.

$$F_{AD,j} = \left\{ -\tilde{\mu}_1 \Delta x_j \left(A_{i-1} \left(\frac{\partial u}{\partial x} \right)_{i-1} - A_i \left(\frac{\partial u}{\partial x} \right)_i \right) + \tilde{\mu}_2 \Delta x_j \left(A_{i-1} \left(\frac{\partial^3 u}{\partial x^3} \right)_{i-1} - A_i \left(\frac{\partial^3 u}{\partial x^3} \right)_i \right) \right\} \cdot p_{mean,j} \tag{4.21}$$

Interpolation Procedure

In the sections above it was discussed how some dependent variables must be interpolated to calculate the desired state variables. To do this a new index "*k*" is introduced to relate the state variables at "*i*" and "*j*", shown in Figure 31. With this new indexing method, two interpolation schemes, linear and cubic,

are implemented. Equation (4.22) shows how linear interpolation is used to calculate the in-between values. Equation (4.23) shows the simplified formula if the distance between “k” indices is the same.

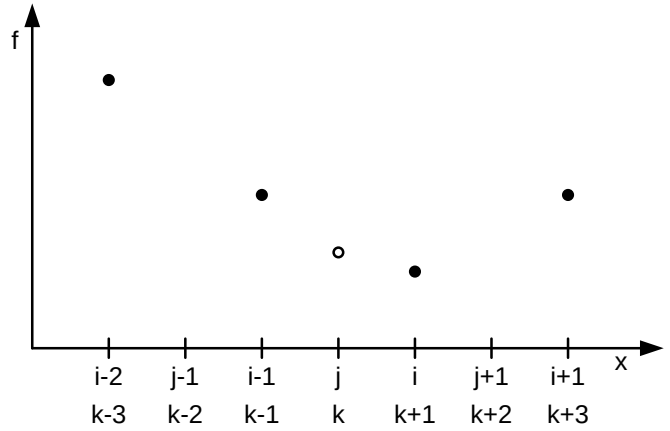

Figure 31: Illustration of state values f as function of x

$$f_k = f_{k-1} + \frac{f_{k+1} - f_{k-1}}{x_{k+1} - x_{k-1}} \cdot (x_k - x_{k-1}) \tag{4.22}$$

$$f_k = \frac{f_{k-1} + f_{k+1}}{2} \tag{4.23}$$

A cubic interpolation method can be used to improve the spatial accuracy of the scheme. To accomplish this we can define the dependent variable f_k to be a function of x_k, as shown in equation (4.24). By using the known values of f_k the coefficients can be calculated using (4.25). If the control volumes have the same width, the coefficients a_0, a_1, a_2, a_3 become constants and equation (4.26) can be used to solve for the intermediate value. However, at boundaries and flow area discontinuities linear interpolation is used, since cubic interpolation would require values past the boundaries.

$$f_k = a_3 x_k^3 + a_2 x_k^2 + a_1 x_k + a_0 \tag{4.24}$$

$$\begin{bmatrix} f_{k-3} \\ f_{k-1} \\ f_{k+1} \\ f_{k+3} \end{bmatrix} = \begin{bmatrix} x_{k-3}^3 & x_{k-3}^2 & x_{k-3} & 1 \\ x_{k-1}^3 & x_{k-1}^2 & x_{k-1} & 1 \\ x_{k+1}^3 & x_{k+1}^2 & x_{k+1} & 1 \\ x_{k+3}^3 & x_{k+3}^2 & x_{k+3} & 1 \end{bmatrix} \begin{bmatrix} a_3 \\ a_2 \\ a_1 \\ a_0 \end{bmatrix} \tag{4.25}$$

$$f_k = \frac{1}{16}(-f_{k-3} + 9f_{k-1} + 9f_{k+1} - f_{k+3}) \tag{4.26}$$

To avoid problems with numerical diffusion and non-physical oscillations an asymmetric interpolation scheme should be used to calculate the specific internal energy values. This interpolation method has an upwind component which causes the coefficients to change depending on the direction of the fluid. To achieve this feature we can set the derivative of equation (4.24) at *k-1* to be equal to the numerical derivate between points *i-1* and *i-2*, and vice versa for flow in the opposite direction. The equations below summarize the results with equations (4.28) and (4.29) assuming that the control volume widths are the same. More information about these methods can be found in [**30**,**31**].

$$\frac{df_{k-1}}{dx} = 3a_3x_{k-1}^2 + 2a_2x_{k-1} + a_1 = \frac{f_{k-1} - f_{k-3}}{2dx} \tag{4.27}$$

$$f_k = \frac{1}{32}(-6f_{k-3} + 27f_{k-1} + 12f_{k+1} - f_{k+3}) \; for \; u_k \geq 0 \tag{4.28}$$

$$f_k = \frac{1}{32}(-f_{k-3} + 12f_{k-1} + 27f_{k+1} - 6f_{k+3}) \; for \; u_k < 0 \tag{4.29}$$

Integration Procedure

A fourth order Runge-Kutta solver [**32**] is used to integrate the mass, momentum and energy derivatives of the conservation equations. The integration process is shown in equation (4.30) in general terms.

$$\hat{f}(x_k, t+\Delta t) = \hat{f}(x_k, t) + (g_1 + 2g_2 + 2g_3 + g_4) \cdot \frac{\Delta t}{6}$$

$$g_1 = \frac{d\hat{f}}{dt}\left(t, \hat{f}\right)$$

$$g_2 = \frac{d\hat{f}}{dt}\left(t + \frac{1}{2}\Delta t, \hat{f} + \frac{1}{2}\Delta t \cdot g_1\right) \tag{4.30}$$

$$g_3 = \frac{d\hat{f}}{dt}\left(t + \frac{1}{2}\Delta t, \hat{f} + \frac{1}{2}\Delta t \cdot g_2\right)$$

$$g_4 = \frac{d\hat{f}}{dt}\left(t + \Delta t, \hat{f} + \Delta t \cdot g_3\right)$$

Collocated Control Volume Schemes

Collocated control volume schemes are different then staggered schemes because the conservation of momentum is not solved in a separate control volume. Since collocated volume schemes solve for fluid properties at only one node, all of the conservation equations can be solved at the same time. Equations (4.31), (4.32), and (4.33) show the conservation of mass, momentum, and energy in differential form using non-conservative variables. Equation (4.34) shows the relationship between the specific energy of the control volume as a function of specific internal energy and specific kinetic energy. The *Y* variable in equation (4.32) is calculated based on the forces defined for the momentum equation of the staggered control volume scheme.

$$\frac{\partial(\rho \cdot A \cdot dx)}{\partial t} + \frac{\partial(\rho \cdot u \cdot A)}{\partial x} dx = 0 \tag{4.31}$$

$$\frac{\partial(\rho \cdot u \cdot A \cdot dx)}{\partial t} + \frac{\partial(\rho \cdot A \cdot u^2 + p \cdot A)}{\partial x} dx - p\frac{dA}{dx} dx + Y = 0 \tag{4.32}$$

$$\frac{\partial(\rho \cdot e \cdot A \cdot dx)}{\partial t} + \frac{\partial\left(\left(e + \frac{p}{\rho}\right) \cdot \rho \cdot u \cdot A\right)}{\partial x} dx - \dot{Q} + \dot{W} = 0 \tag{4.33}$$

$$e = I + \frac{u^2}{2} \tag{4.34}$$

The conservation equations above are often simplified by assuming that the control volume cannot expand or contract. This assumption allows the *dx* term to be removed from the partial derivative with respect to time to cancel out with other *dx* terms. In this case the rate of work would have to equal zero. However, these equations cannot be used to solve the accumulator problem since some control volumes will expand and contract.

In order to incorporate the change in volume, the conservation equations above need to be modified. A new volume variable is introduced and is defined by equation (4.35). The new conservation equations are formed by placing the volume variable in the conservation equations above and carrying out the partial derivatives. The result is shown in equations (4.36), (4.37) and (4.38).

$$V = A \cdot dx \tag{4.35}$$

$$V\frac{\partial(\rho)}{\partial t} + \frac{\partial(\rho \cdot u \cdot A)}{\partial x} dx + \rho \frac{\partial(V)}{\partial t} = 0 \tag{4.36}$$

$$V\frac{\partial(\rho \cdot u)}{\partial t} + \frac{\partial\left((\rho \cdot u^2 + p) \cdot A\right)}{\partial x} dx + \rho \cdot u \frac{\partial(V)}{\partial t} - p\frac{dA}{dx} dx + \Upsilon = 0 \tag{4.37}$$

$$V\frac{\partial(\rho \cdot e)}{\partial t} + \frac{\partial\left(\rho \cdot A \cdot u\left(e + \frac{p}{\rho}\right)\right)}{\partial x} dx + \rho \cdot e\frac{\partial(V)}{\partial t} - \dot{Q} + \dot{W} = 0 \tag{4.38}$$

The conservation of equations can be written in vector form by defining a state vector ***W***, flux vector ***F***, and a source vector ***C***. The conservation equation in vector form is shown in (4.42).

$$\boldsymbol{W} = \begin{bmatrix} \rho \\ \rho \cdot u \\ \rho \cdot e \end{bmatrix} \tag{4.39}$$

$$\boldsymbol{F} = \begin{bmatrix} \rho \cdot u \cdot A \\ (\rho \cdot u^2 + p) \cdot A \\ \rho \cdot A \cdot u \cdot \left(e + \frac{p}{\rho}\right) \end{bmatrix} \tag{4.40}$$

$$\boldsymbol{C} = \begin{bmatrix} \rho \frac{\partial(V)}{\partial t} \\ \rho \cdot u \frac{\partial(V)}{\partial t} - p \cdot \frac{dA}{dx} dx + \Upsilon \\ \rho \cdot e \frac{\partial(V)}{\partial t} + \dot{W} - \dot{Q} \end{bmatrix} \tag{4.41}$$

$$V \frac{\partial \mathbf{W}}{\partial t} + \frac{\partial \mathbf{F}}{\partial x} dx + \mathbf{C} = 0 \tag{4.42}$$

Using equation (4.42) we can now discretize it and use numerical integration to solve for the states in the next time step. Equation (4.43) shows the double integral over space and time. Using a first order differencing approach, equation (4.44) shows that the future state value *n+1* at "*i*" depends on the current state (*n, i*), the current flux variables at the boundaries (*n, i+1/2*) and (*n, i-1/2*) and the remaining source terms at (*n, i*). Equation (4.45) shows the source terms in discretized form when using a first order differentiation method.

$$\iint \left(V \frac{\partial \mathbf{W}}{\partial t} + \frac{\partial \mathbf{F}}{\partial x} dx + \mathbf{C} \right) dx dt = 0 \tag{4.43}$$

$$V \cdot (\mathbf{W}_i^{n+1} - \mathbf{W}_i^n) \Delta x + \left(\mathbf{F}_{i+1/2}^n - \mathbf{F}_{i-1/2}^n \right) \Delta x \Delta t + \mathbf{C}_i^n \Delta x \Delta t = 0 \tag{4.44}$$

$$\boldsymbol{C}_i^n = \begin{bmatrix} \rho_i \dfrac{\partial V_i}{\partial t} \\ \rho_i \cdot u_i \dfrac{\partial V_i}{\partial t} - p_i \cdot \left(A_{i+1/2} - A_{i-1/2}\right) + Y_i \\ \rho_i \cdot e_i \dfrac{\partial V_i}{\partial t} + \dot{W}_i - \dot{Q}_i \end{bmatrix}^n \tag{4.45}$$

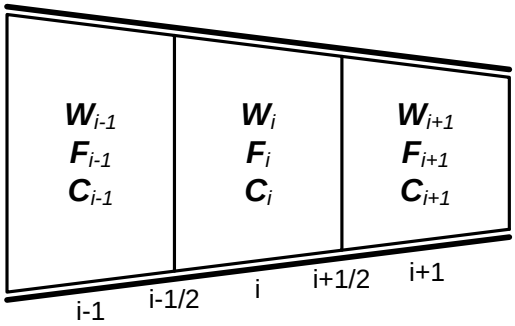

Figure 32: Discretized control volume representation in vector form

However, the numerical solution of equation (4.44) becomes unstable due to oscillatory behavior, which is caused by the current state $\boldsymbol{W}$ at (*i, n*). To circumvent this problem the Lax-Friedrichs and the two step Lax-Wendroff schemes can be used.

Lax-Friedrichs Scheme

Lax [**33**] suggested replacing the state variable $\boldsymbol{W}_i^n$ with the average of its surrounding points. This effect can be seen in Figure 33, and equation (4.46). To find the flux terms at the control volume boundaries, the averaged flux values are used, shown in equation (4.47). This scheme has first order accuracy in space and time.

$$\boldsymbol{W}_i^n = \frac{1}{2}(\boldsymbol{W}_{i+1}^n + \boldsymbol{W}_{i-1}^n) \tag{4.46}$$

$$\boldsymbol{F}_{i+1/2} = \frac{1}{2}[\boldsymbol{F}_{i+1} + \boldsymbol{F}_i] \quad and \quad \boldsymbol{F}_{i-1/2} = \frac{1}{2}[\boldsymbol{F}_i + \boldsymbol{F}_{i-1}] \tag{4.47}$$

$$\boldsymbol{W}_i^{n+1} = \frac{1}{2}[\boldsymbol{W}_{i+1}^n + \boldsymbol{W}_{i-1}^n] - (\boldsymbol{F}_{i+1}^n - \boldsymbol{F}_{i-1}^n) \cdot \frac{\Delta t}{2 \cdot V} - \boldsymbol{C}_i^n \frac{\Delta t}{V} \qquad (4.48)$$

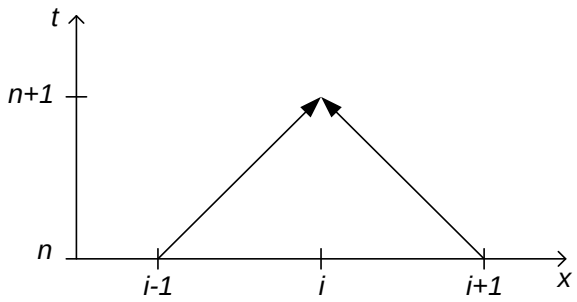

Figure 33: Computational stencil for the Lax-Friedrich's Scheme

The two-step Lax-Wendroff method

In the method above we only obtain first order accuracy with respect to time. Lax et al. [**34**] suggested using the Lax-Wendroff scheme, which uses the Taylor series expansion to compute higher order terms. This leads to a solution that is dependent on the evaluation of a Jacobian matrix. To avoid this feature, the two-step Lax-Wendroff method, given by Richtmyer [**35**], can be used to achieve second order accuracy in time.

The first step of this scheme is the Lax-Friedrichs method solved at the halfway point in time and space, as shown in Figure 34. Equations (4.49) and (4.50) illustrate how the state halfway points can be calculated. The second step involves using a Leapfrog calculation with respect to the state variables, and the use of the flux variables and remaining items at the halfway points. The halfway points can be calculated based on the resulting state variable of the first step. The solid lines in Figure 34 and equation (4.51) show the details of this step.

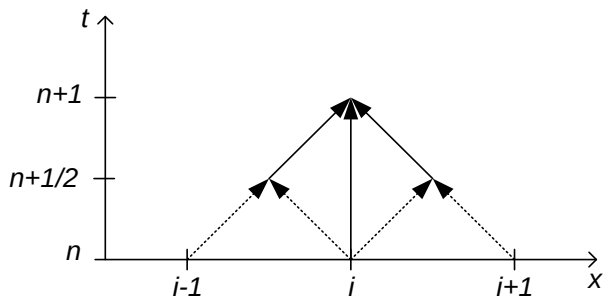

Figure 34: Computational stencil for the two-step Lax-Wendroff

$$\mathbf{W}_{i+\frac{1}{2}}^{n+\frac{1}{2}} = \frac{1}{2}[\mathbf{W}_{i+1}^{n} + \mathbf{W}_{i}^{n}] - (\mathbf{F}_{i+1}^{n} - \mathbf{F}_{i}^{n}) \cdot \frac{\Delta t}{2\Delta x} - (\mathbf{C}_{i+1}^{n} + \mathbf{C}_{i}^{n})\frac{\Delta t}{4} \tag{4.49}$$

$$\mathbf{W}_{i-1/2}^{n+1/2} = \frac{1}{2}[\mathbf{W}_{i}^{n} + \mathbf{W}_{i-1}^{n}] - (\mathbf{F}_{i}^{n} - \mathbf{F}_{i-1}^{n}) \cdot \frac{\Delta t}{2\Delta x} - (\mathbf{C}_{i}^{n} + \mathbf{C}_{i-1}^{n})\frac{\Delta t}{4} \tag{4.50}$$

$$\mathbf{W}_{i}^{n+1} = \mathbf{W}_{i}^{n} - \left(\mathbf{F}_{i+1/2}^{n+1/2} - \mathbf{F}_{i-1/2}^{n+1/2}\right) \cdot \frac{\Delta t}{\Delta x} - (\mathbf{C}_{i+1/2}^{n+\frac{1}{2}} + \mathbf{C}_{i-1/2}^{n+\frac{1}{2}})\frac{\Delta t}{2} \tag{4.51}$$

Boundary Conditions

To model the boundary conditions with collocated schemes, Winterbone and Pearson [**14**] suggest using the CIR (Courant, Isaacson, Rees) method or the method of characteristics. These two methods are based on the solution of the compatibility characteristic equations with the only difference being that the CIR method is expressed in terms of non-conservative variables (ρ, u, p) as opposed to the method of characteristics, which uses Riemann variables. For the purpose of our model we will only focus on the first method. It should be noted that this approach utilizes the ideal gas relationship to calculate the states at the boundaries.

The CIR method was first proposed by Courant et al. [**36**], and this scheme centers around the derivation of the compatibility equations. To obtain

these equations we must first carry out the differentiation of the conservation equations (4.31), (4.32) and (4.33). The result is shown in the equations below.

$$m = \rho \cdot A \cdot dx \tag{4.52}$$

$$\frac{\partial m}{\partial t} + u\frac{\partial m}{\partial x} + m\frac{\partial u}{\partial x} \tag{4.53}$$

$$m\frac{\partial u}{\partial t} + mu\frac{\partial u}{\partial x} + V\frac{\partial p}{\partial x} + \Upsilon = 0 \tag{4.54}$$

$$\frac{\partial \mathrm{I}}{\partial t} + u\frac{\partial \mathrm{I}}{\partial x} - \left(\frac{pV}{m^2}\right)\cdot\left(\frac{\partial m}{\partial t} + u\frac{\partial m}{\partial x}\right) + \frac{up}{m}\frac{\partial V}{\partial x} + \frac{\dot{W} - \dot{Q} - u\Upsilon}{m} = 0 \tag{4.55}$$

The next step is to convert the mass and the specific internal energy variables in equation (4.55) with the density and pressure variables instead. This is possible by using the relationship between the internal energy and temperature of the gas, seen in equation (4.56). This equation is than coupled with the ideal gas equation (4.57) to create equation (4.58).

$$C_v = \left(\frac{\partial \mathrm{I}}{\partial T}\right)_v \tag{4.56}$$

$$T = \frac{p}{\rho R} \tag{4.57}$$

$$\frac{\partial p}{dt} + u\frac{\partial p}{dx} - a^2\left(\frac{\partial \rho}{\partial t} + u\frac{\partial \rho}{\partial x}\right) - \frac{\rho R}{C_v}\cdot\frac{\dot{Q} + u\Upsilon}{m} = 0 \tag{4.58}$$

The next step is to derive equations (4.53) and (4.54) in terms of density. The outcome is shown in equations (4.59) and (4.60). By combining these equations as indicated in equation (4.61) it is possible to obtain the equations (4.62).

$$\frac{\partial \rho}{\partial t} + u\frac{\partial \rho}{\partial x} + \rho\frac{\partial u}{\partial x} + \frac{\rho}{V}\left(\frac{\partial V}{\partial t} + u\frac{\partial V}{\partial x}\right) = 0 \tag{4.59}$$

$$\frac{\partial u}{\partial t} + u\frac{\partial u}{\partial x} + \frac{1}{\rho}\frac{\partial p}{\partial x} + \frac{\Upsilon}{\rho V} = 0 \tag{4.60}$$

$$(4.58) + a^2(4.59) \pm (4.60) \tag{4.61}$$

$$\frac{\partial p}{dt} + (u \pm a)\frac{\partial p}{dx} \pm \rho a\left(\frac{\partial u}{\partial t} + (u \pm a)\frac{\partial u}{\partial x}\right) + \Delta_1 + \Delta_2 \pm \Delta_3 = 0 \tag{4.62}$$

$$\Delta_1 = -\frac{\rho R}{C_v} \cdot \frac{\dot{Q} + uY}{m} = -\frac{R}{C_v} \cdot \frac{\dot{Q} + u\Upsilon}{V} \tag{4.63}$$

$$\Delta_2 = \frac{a^2\rho}{V}\left(\frac{\partial V}{\partial t} + u\frac{\partial V}{\partial x}\right) \tag{4.64}$$

$$\Delta_3 = \frac{a\Upsilon}{V} \tag{4.65}$$

The final step is to define the pathline and wave characteristics. The pathline characteristic is defined in equation (4.66), and it can be applied to equation (4.58). This is done to obtain the “total” time derivate of pressure and density variables with respect to time as shown in equation (4.67). The same is true for the wave characteristic, which is defined in equation (4.68). When this is combined with equation (4.62), the remaining compatibility equations are shown in (4.69).

$$\frac{dx}{dt} = u \tag{4.66}$$

$$\frac{dp}{dt} - a^2\frac{d\rho}{dt} + \Delta_1 = 0 \tag{4.67}$$

$$\frac{dx}{dt} = u \pm a \tag{4.68}$$

$$\frac{dp}{dt} \pm \rho a \frac{du}{dt} + \Delta_1 + \Delta_2 \pm \Delta_3 = 0 \tag{4.69}$$

Using the compatibility equations, it is now possible to create a scheme which may be used to solve for the future values of density, pressure, and velocity. The first step to obtaining such a scheme is to discretize the compatibility equations in a first order manner. To figure out how the discretization should be made we can turn to Figure 35. From this figure we can see that it is possible to trace the information pathway between the node (*i, n+1*) to previous nodes at time t_n. The spatial location of the nodes in time t_n can be obtained using the pathline, equation (4.66), and wave, equation (4.68), characteristics. Equations (4.67) and (4.69) can be written in discretized form as demonstrated in equations (4.70), (4.71) and (4.72).

$$(p_i^{n+1} - p_S^n) - (a_S^n)^2(\rho_i^{n+1} - \rho_S^n) + (\Delta_1)_L^n \cdot \Delta t = 0 \tag{4.70}$$

$$(p_i^{n+1} - p_L^n) + \rho_L^n a_L^n (u_i^{n+1} - u_L^n) + (\Delta_1 + \Delta_2 + \Delta_3)_L^n \cdot \Delta t = 0 \tag{4.71}$$

$$(p_i^{n+1} - p_R^n) - \rho_R^n a_R^n (u_i^{n+1} - u_R^n) + (\Delta_1 + \Delta_2 - \Delta_3)_R^n \cdot \Delta t = 0 \tag{4.72}$$

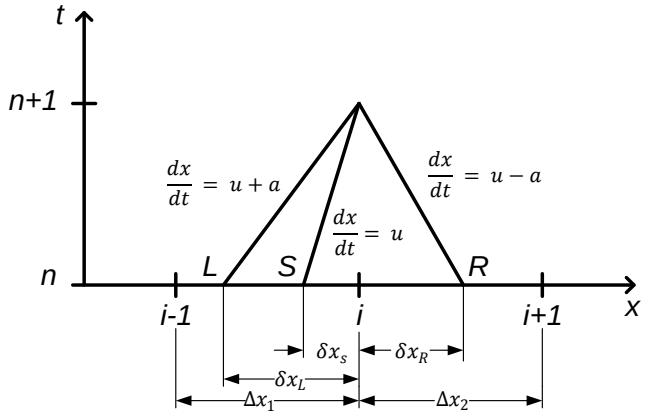

Figure 35: CIR method computational stencil

The last remaining step is to find the correct value of the state variables at the *L*, *R*, and *S* spatial locations. This can be done by linear interpolation, and using the pathline and wave characteristics properties shown in (4.74), (4.75), and (4.76). The variable "*a"* is the speed of sound shown in equation (4.80).

$$\chi = \begin{bmatrix} \rho \\ u \\ p \end{bmatrix} \tag{4.73}$$

$$\chi_L^n = \chi_i^n - \frac{\delta x_L}{\Delta x_1}(\chi_i^n - \chi_{i-1}^n) \tag{4.74}$$

$$\chi_R^n = \chi_i^n - \frac{\delta x_R}{\Delta x_2}(\chi_{i+1}^n - \chi_i^n) \tag{4.75}$$

$$\chi_S^n = \chi_i^n - \frac{\delta x_S}{\Delta x_1}(\chi_i^n - \chi_{i-1}^n) \tag{4.76}$$

$$\frac{\delta x_L}{\Delta x_1} = \frac{u_i^n - a_i^n}{\frac{\Delta x_1}{\Delta t} + (u_i^n - u_{i-1}^n) + (a_i^n - a_{i-1}^n)} \tag{4.77}$$

$$\frac{\delta x_R}{\Delta x_2} = \frac{u_i^n - a_i^n}{\frac{\Delta x_2}{\Delta t} - (u_{i+1}^n - u_i^n) + (a_{i+1}^n - a_i^n)} \tag{4.78}$$

$$\frac{\delta x_S}{\Delta x_1} = \frac{u_i^n}{\frac{\Delta x_1}{\Delta t} + (u_i^n - u_{i-1}^n)} \tag{4.79}$$

$$a^2 = \frac{\gamma p}{\rho} \tag{4.80}$$

Schemes Validation and Comparison

One of the biggest problems with writing a CFD code is the validation part. For this reason we decided to use a shock tube experiment to understand the

difference between the different schemes. The shock tube is a numerical example that simulates an infinitely long pipe with a diaphragm in the middle. The gas in the pipe is stagnant, but the state of the fluid is different across the diaphragm. The simulation then begins when the diaphragm is broken causing the fluid states to change as function of time and space.

Figure 36: Shock tube experiment visualization

Riemann Problem

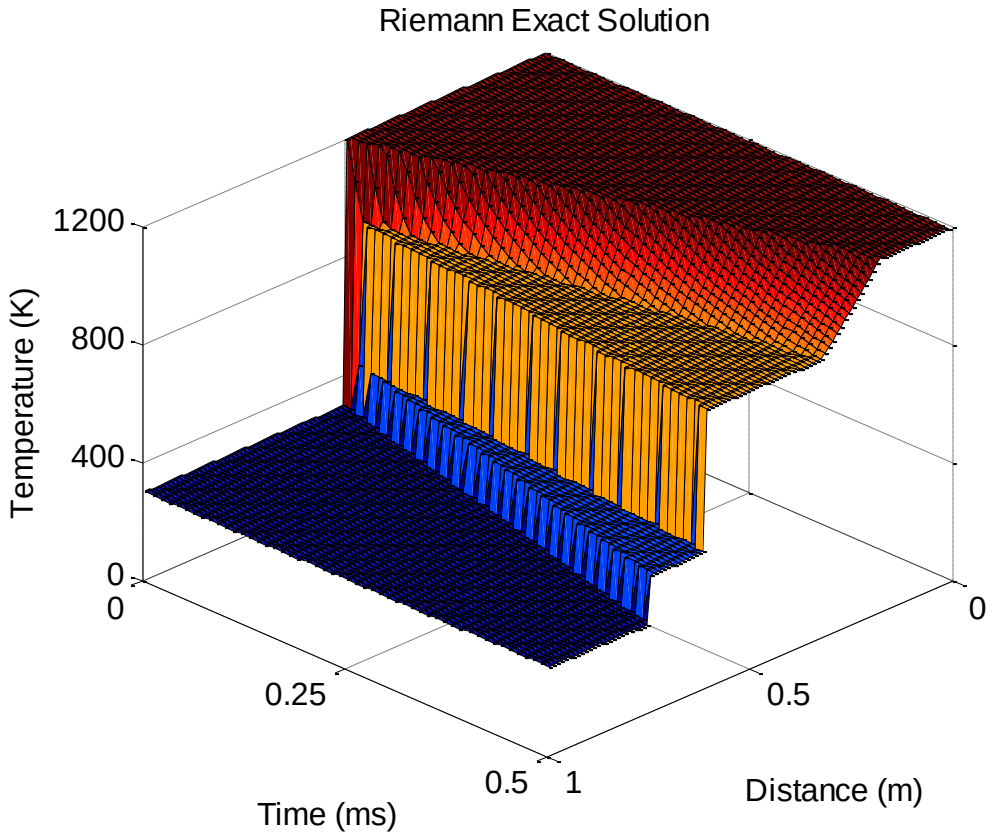

Figure 37: Temperature response "exact" (to a certain degree of accuracy) solution

Before we show the shock tube results for the different schemes, it is imperative that we calculate the exact solution (to a desired degree of accuracy) for comparison purposes. To this end we use the solution of the Riemann problem given by Toro [**37**]. The Riemann problem is solved using an extension of the work by Courant et al. [**36**], which is detailed in the Collocated Control Volume Schemes: Boundary Conditions section. Readers interested in the details of the algorithm used to calculate the exact solution are referred to [**37**]. Figure 37 shows how the temperature changes across space and time.

Staggered Scheme Results

Using the methods described in the Staggered Control Volume Schemes section, it was possible to create three possible implementation methods. All the methods use a fourth order Runge-Kutta integrator as show previously. The first implementation method uses linear interpolation to solve for the control volume boundary values. The results of this scheme are shown in Figure 38, and we can see that large oscillations are present in the temperature and density values.

The cubic scheme implementation causes the magnitude of the oscillations to decrease, but are still present as shown in Figure 39. Only when the cubic upwind scheme is used towards the specific internal energy variable, do the oscillations seem to disappear, as seen in Figure 40. However, regardless of interpolation method the staggered scheme seems to offer good accuracy when compared to the “exact” solution.

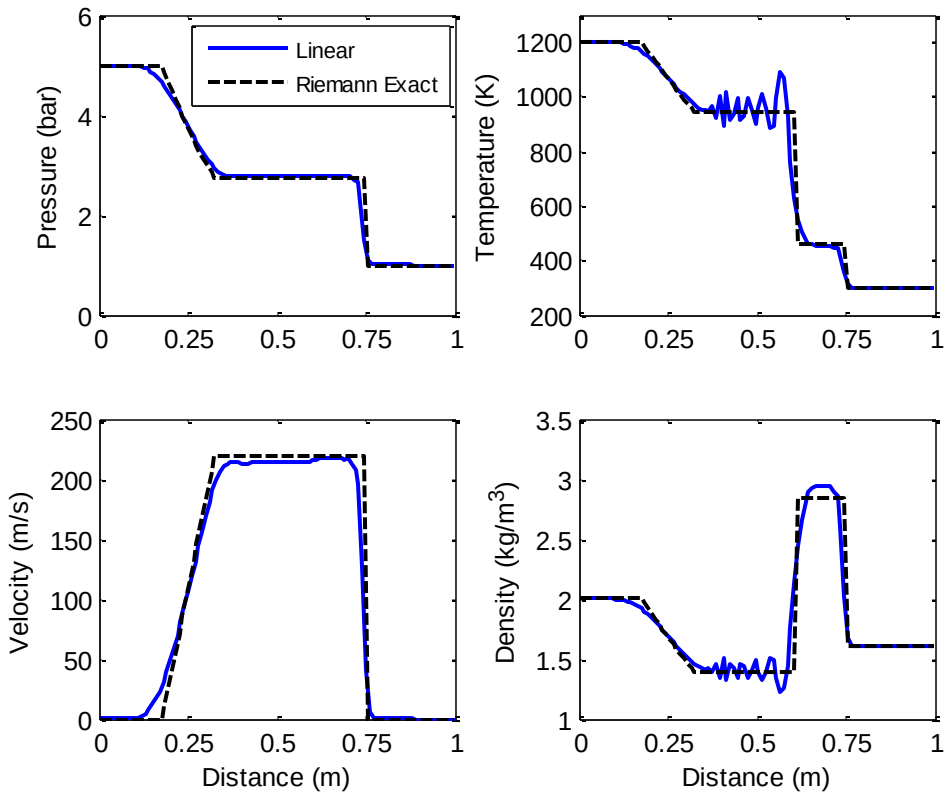

Figure 38: Linear interpolation staggered scheme with 4th order Runge-Kutta comparison

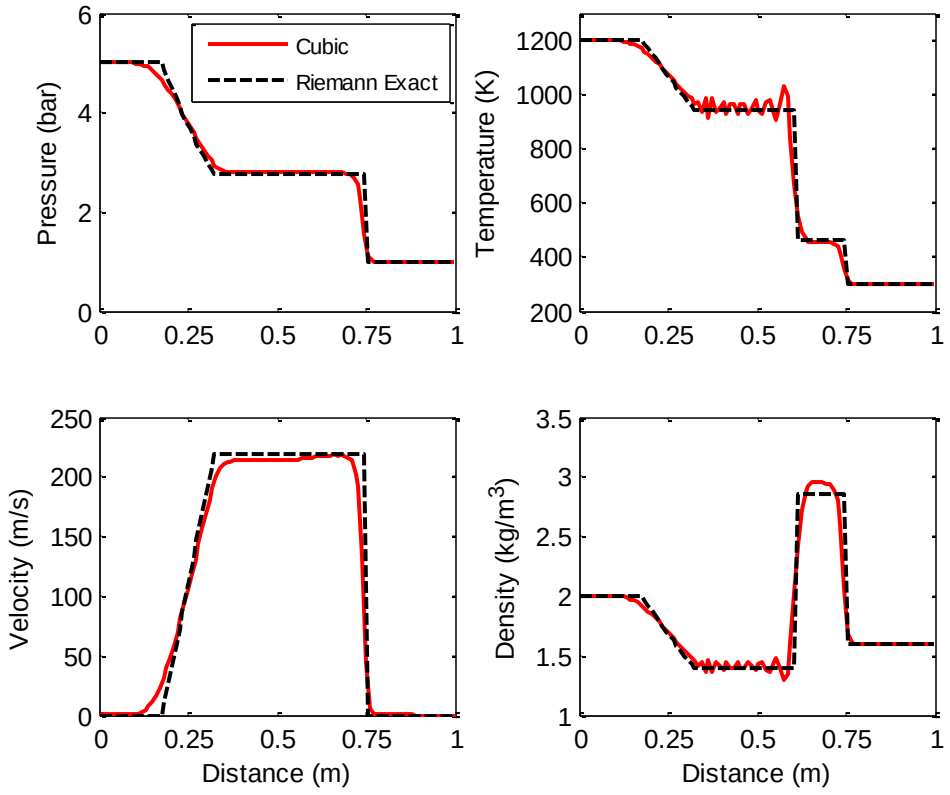

Figure 39: Cubic interpolation staggered scheme with 4th order Runge-Kutta comparison

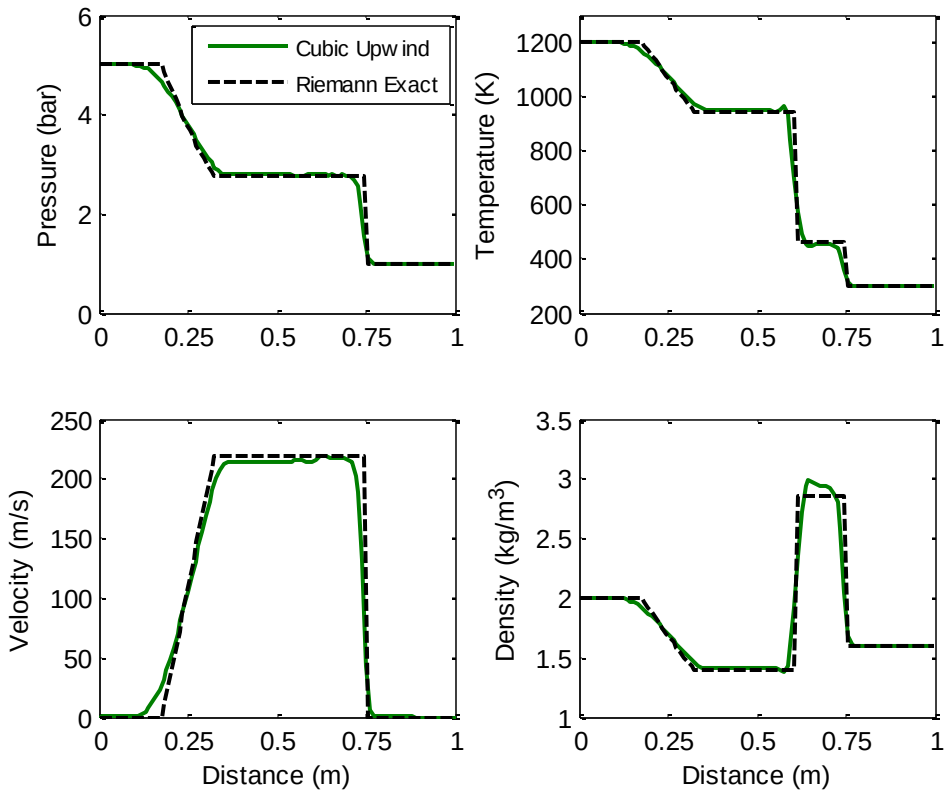

Figure 40: Cubic upwind interpolation staggered scheme with 4th order Runge-Kutta comparison

Collocated Schemes Results

The Lax-Friedrichs method, shown in Figure 41, has an averaging effect on the properties of the gas. This scheme has second order accuracy in space, and first order accuracy in time. Because of the smoothing effect, the accuracy of the solution is very poor. The two-step Lax-Wendroff method has second order accuracy in time and space. This scheme captures the shape of the solution very accurately. However, large numerical oscillations are present which can be seen in Figure 42.

To increase the accuracy of collocated schemes Winterbone and Pearson [**14**] explain that high frequency oscillations can be mitigated by using numerical dissipation and dispersion methods. Unfortunately, these methods require the

tuning of coefficients which can vary depending on the application. Winterbone and Peterson further suggest using upwind schemes and Riemann solvers, such as Godunov's method, Roe's approximate Riemann solver, the Harten-Lax-van Leer (HLL) Riemann solver, and the HLLC Riemann solver. Visual inspections of the shock tube results show that these schemes yield accurate results similar to those of the staggered cubic upwind method. High resolution schemes are also suggested as possible methods to improve with the total variation diminishing (TVD) concept, flux-corrected transport (FCT), and flux limiters.

The drawback of the methods suggested above is that the schemes are more complex to implement and the computational time increases by more than two times when compared to the two-step Lax-Wendroff method (see Winterbone and Pearson [**14**]). In order to achieve better accuracy we suggest the use of a blended Lax-Friedrichs (LF) scheme with the two-step method Lax-Wendroff (LW). Liska and Wendroff [**38**] denote that this method has only first order accuracy, but have smaller second order errors due to the recursive use of the two-step Lax-Wendroff.

The blending strategy works by solving one time step using the LF scheme, and a number of steps using the LW scheme. Figure 43 shows the shock tube results for such a scheme with one LF calculation after every five LW calculations.

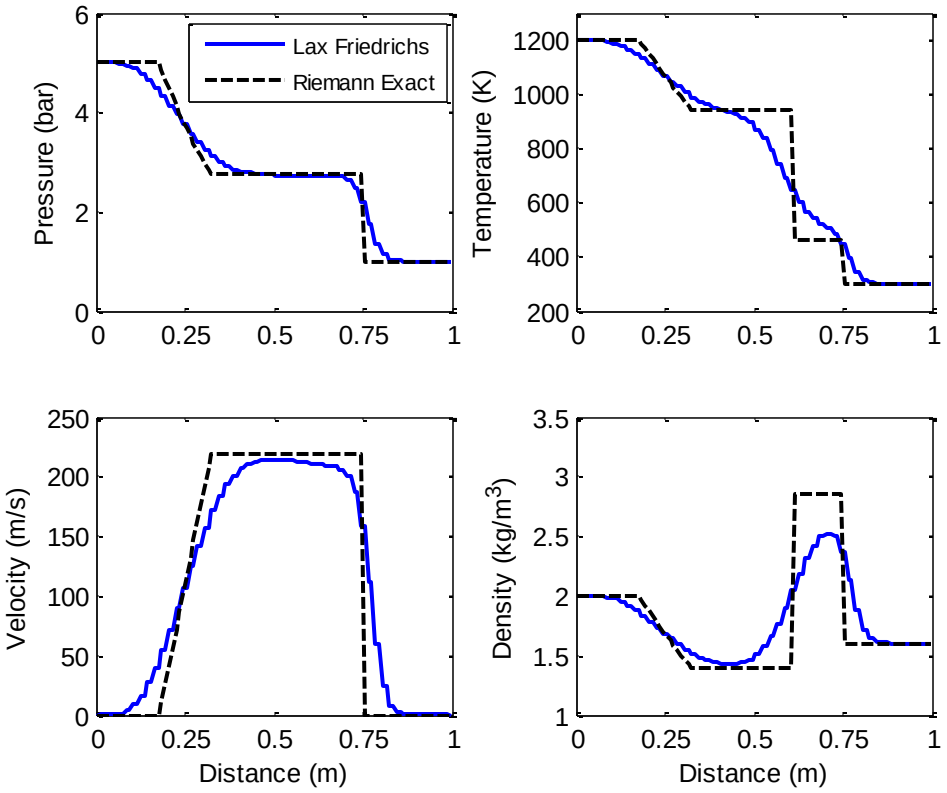

Figure 41: Lax-Friedrichs scheme comparison

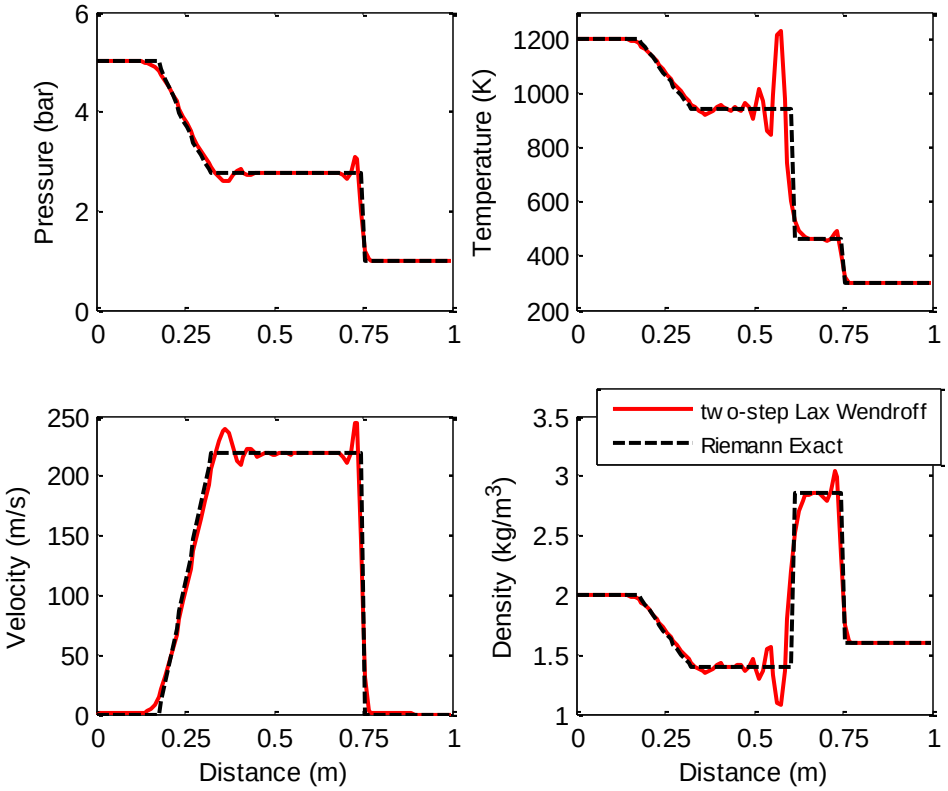

Figure 42: The two-step Lax-Wendroff scheme comparison

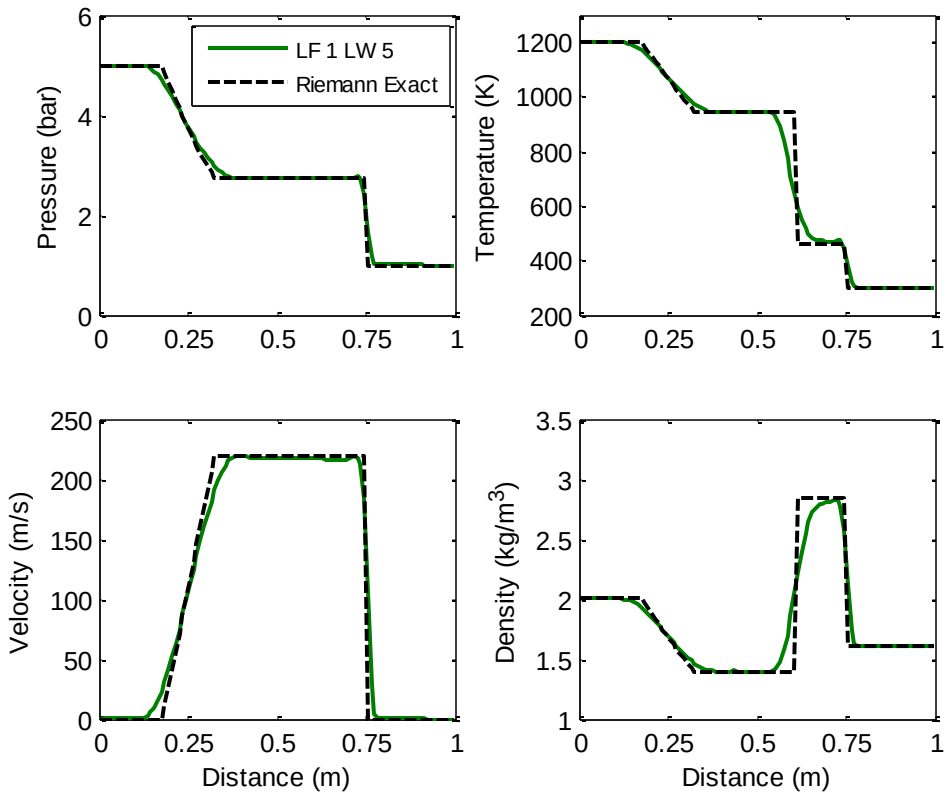

Figure 43: Blended Lax-Friedrichs and two-step Lax Wendroff comparison

Conclusion

The results above show that a cubic upwind staggered control volume scheme will yield the best results of the analyzed schemes. The blended Lax-Friedrichs/Lax-Wendroff also offers good accuracy with less computational cost then the cubic upwind scheme. However, the collocated schemes suffer from mass and energy conservation errors when the spatial discretization is not even, between control volumes of changing diameter, and when pressure waves interact with the boundary. For this reason the cubic upwind staggered scheme is used to create the thermally boosted accumulator model.

CHAPTER V

Thermodynamics and Heat Transfer Models

Nomenclature

a_{nm}, i_m, j_m, k_m	Equation of state constants
a	Speed of sound
a_e	Estimated speed of sound
$\tilde{a}$	Metal foam surface area density
A^r	Residual Helmholtz free energy
C_f	Specific heat capacity of fluid
C_v^0	Ideal gas specific heat at constant volume
C_v	Specific heat at constant volume
d	Shape factor for heat transfer
d_f	Metal foam fiber diameter
d_p	Pore diameter
Da	Darcy number
f	Friction factor
$\bar{h}$	Overall convective heat transfer coefficient
h_{sf}	Convective heat transfer coefficient between fluid and solid
I	Gas specific internal energy
$J_\alpha(.)$	Modified Bessel function
K	Permeability
k_e	Effective thermal conductivity
k_f	Fluid thermal conductivity
k_{fe}	Effective fluid thermal conductivity

k_s	Solid thermal conductivity
k_{se}	Effective solid thermal conductivity
Nu	Nusselt number
Nu_{sf}	Nusselt number between solid and fluid
p	Gas pressure
p^*	Saturation pressure
p_c	Critical gas pressure
p_e	Estimated gas pressure
Pr	Prandtl number
$\dot{Q}$	Rate of rate in
$\dot{Q}''_w$	Wall heat flux
R	Ideal gas constant
r	Radial distance
R_p	Pipe radius
Re_d	Metal foam localized Reynolds number
T	Gas temperature
t	Time
T_c	Critical gas temperature
T_e	Estimated gas temperature
T_f	Temperature of fluid
$T_{f,b}$	Bulk fluid temperature
T_s	Temperature of solid
T_w	Wall temperature
U	Dimensionless velocity parameter
u	Gas velocity
u_m	Mean fluid velocity
V	Gas volume
x	Longitudinal distance
Z_c	Critical compression factor
δ	Reduced density
ε	Metal foam porosity
θ_f	Dimensionless fluid temperature
$\theta_{f,b}$	Dimensionless bulk fluid temperature

θ_s	Dimensionless solid temperate
μ	Gas viscosity
ρ	Gas density
ρ_c	Critical gas density
ρ_f	Fluid density
τ	Reduced temperature
τ_e	Estimated reduced pressure
Υ	Reduced specific internal energy
ϕ^0	Dimensionless Helmholtz free energy for an ideal gas
ϕ^r	Dimensionless residual Helmholtz free energy
ψ	Dimensionless radial coordinate
ω	Accentric factor

Selection of a Working Fluid

For all the studies above, nitrogen gas is used as the working fluid; however this may not be the best choice for a thermally boosted accumulator. In the *Heat Transfer Simulation Case Study* section it's shown that the heat transfer, $\dot{Q}$, is linearly proportional to the power, $P \cdot dV/dt$, coming in or out of the accumulator for an ideal gas (see equation (3.6)). From this equation, the heat transfer can be minimized by selecting a fluid with the smallest C_v/R ratio. Another interpretation of this equation is that the fluid with the lowest molecular heat capacity will require the least amount of heat to maintain constant pressure. A quick search in the internet yields the results displayed in Table 6. This means that several noble gases can be used to reduce the heat transfer required by approximately 28%.

$$-p \cdot \frac{dV}{dt} \cdot \left(\frac{C_v}{R} + 1\right) = \dot{Q} \tag{3.6}$$

Name of Gas		C_v (kJ/kg-K)	R (kJ/kg-K)	C_v/R	Improv. (%)
Sulfur Dioxide	SO_2	0.510	0.130	3.92	-40.59
Carbon Dioxide	CO_2	0.655	0.189	3.47	-27.53
Nitrogen	N_2	0.743	0.297	2.50	0.0
Hydrogen	H_2	10.16	4.120	2.47	1.02
Helium	He	3.120	2.080	1.50	28.61
Argon	Ar	0.312	0.208	1.50	28.61
Neon	Ne	0.618	0.412	1.50	28.61

Table 6: Gas properties comparison to minimize heat transfer [39**]**

Real Gas Model

In the previous section we showed that a noble gas is an excellent choice as the working fluid of a thermally boosted accumulator. Helium gas offers several advantages such as low density and large availability. However, gases with low atomic numbers are known to be highly permeable, and can cause problems by diffusing through the bladder into the hydraulic oil. The next noble gas in the periodic table is Neon, but this gas is not desirable because it is an element that is rare to find in the atmosphere with 1 part in 65,000 of air [**40**]. The best suitable working gas is then Argon, which is the third most abundant gas in the atmosphere at 0.94%, which is a higher percentage than that of carbon dioxide [**41**].

With argon as the working gas, we must consider the behavior of the gas at high operating pressures since argon, like nitrogen gas, does not behave like

an ideal gas at these conditions. The pressure of the fluid can be predicted with an equation of state which is a function of two thermodynamic variables, such as fluid density and temperature. The equation of state is usually expressed in the form of the BWR equation (used in the previous chapters for the nitrogen gas analysis) or the Lee-Kesler equation. However, the coefficients for argon gas are not readily available for these equations. Furthermore, due to the form of the energy conservation equation (4.8), derived in the Fluid Dynamics Models chapter, the temperature must be estimated from the fluid density and specific internal energy values.

A generalized corresponding-states equation of state was developed by Xiang et al. [**15**] which the pressure and other thermodynamic properties can be calculated given the current density and temperature of the gas. The semi-universal equation of state developed in [**15**] can be used to calculate various gas properties (Argon, Nitrogen, Methane, Ammonia, Water, etc.) over a wide range of temperature, density and pressure. To create this equation the residual Helmholtz free energy can be calculated using equation (5.1). The resulting equation uses 42 coefficients (a_{nm}), 36 exponents (i_m, j_m, k_m), the gases acentric factor ω and the aspherical factor θ. These factors can be calculated using the critical constants of the fluid given by (5.3) and (5.4). Lastly, the reduced density δ and inversed reduced temperature τ are the remaining variables needed to solve for the dimensionless residual Helmholtz free energy.

Applying Maxwell relations to the dimensionless residual Helmholtz free energy yields the various thermodynamic states, such as, pressure, internal

energy, heat capacity, speed of sound, shown in equations (5.7), (5.8), and (5.9) respectively. For these states the ideal gas Helmholtz free energy and its derivatives need to be calculated, and then can found in Tegeler et al. [**42**] for the argon gas.

$$\phi^r = \frac{A^r}{RT} = \sum_{n=0}^{2} \left[\sum_{m=1}^{6} a_{nm} \delta^{i_m} \tau^{j_m} + \sum_{m=7}^{14} a_{nm} \delta^{i_m} \tau^{j_m} \, exp(-\delta^{k_m}) \right] b_n \tag{5.1}$$

$$b_0 = 1 \qquad b_1 = \omega \qquad b_2 = \theta \tag{5.2}$$

$$\omega = -1 - log\left(\frac{p^*}{p_c}\right) \tag{5.3}$$

$$\theta = (Z_c - 0.29)^2 \tag{5.4}$$

$$\delta = \rho/\rho_c \tag{5.5}$$

$$\tau = T_c/T \tag{5.6}$$

$$\frac{p}{\rho RT} = 1 + \delta \left(\frac{\partial \phi^r}{\partial \delta}\right)_\tau \tag{5.7}$$

$$\frac{I}{RT} = \tau \left(\left(\frac{\partial \phi^0}{\partial \tau}\right)_\delta + \left(\frac{\partial \phi^r}{\partial \tau}\right)_\delta \right) \tag{5.8}$$

$$\frac{Ma^2}{RT} = 1 + 2\delta \left(\frac{\partial \phi^r}{\partial \delta}\right)_\tau + \delta^2 \left(\frac{\partial^2 \phi^r}{\partial \delta^2}\right)_\tau - \frac{\left(1 + \delta \left(\frac{\partial \phi^r}{\partial \delta}\right)_\tau - \delta\tau \left(\frac{\partial^2 \phi^r}{\partial \delta \partial \tau}\right)\right)^2}{\tau^2 \left(\left(\frac{\partial^2 \phi^0}{\partial \tau^2}\right)_\delta + \left(\frac{\partial^2 \phi^r}{\partial \tau^2}\right)_\delta \right)} \tag{5.9}$$

Two problems arise when trying to implement the equations above with the conservation equations of the previous chapter. The first issue is that using the generalized state equations is a computationally expensive procedure requiring 36 exponentiation operations per time step, which will slow down the

code considerably. The second more critical issue is that the equations of state above are expressed as functions of density and temperature. However, the conservation of energy equation is solved for the energy variable (4.11), which dictates that the specific internal energy is known rather than temperature. For that reason equation (5.8) must be rearranged to compute the value of temperature as a function of density and specific internal energy.

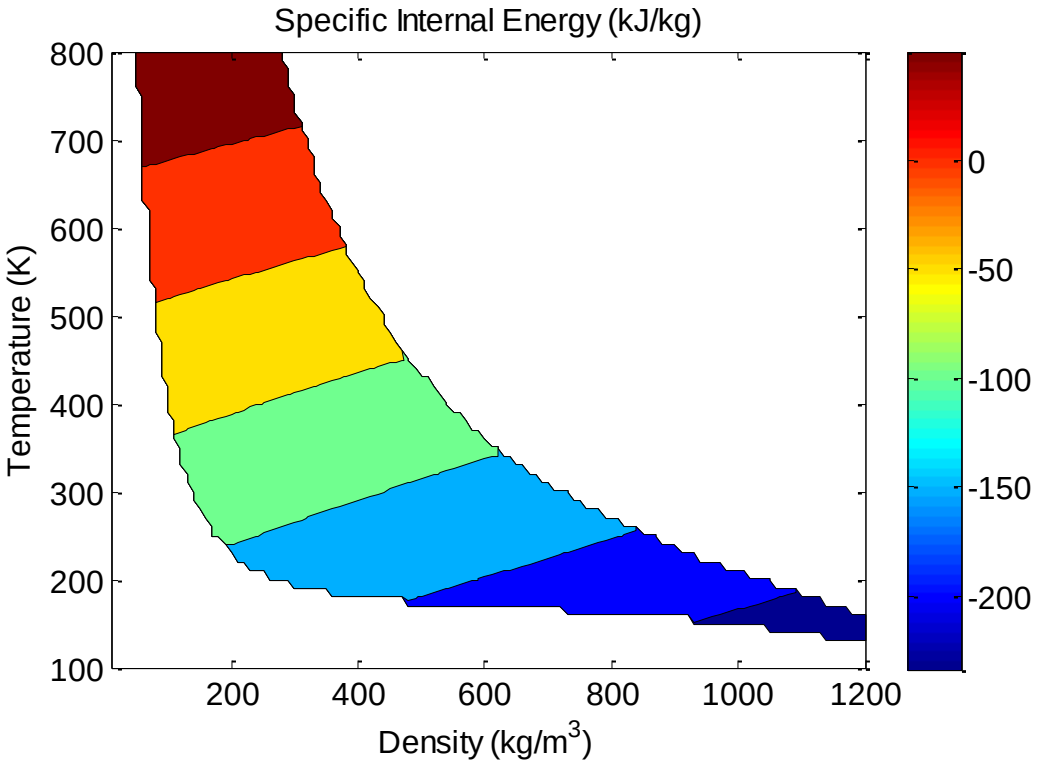

Figure 44: Argon gas internal energy calculated from equation (5.8)

To estimate the gas temperature based on the specific internal energy and density, equation (5.8) is used to generate data that can be fitted to a polynomial. To simplify the fitting process the input data is constrained by a maximum pressure of 550 (bar) and a minimum pressure of 80 (bar). This range is used since it is well within the operating range of the accumulator. Figure 44 shows the

specific internal energy values of argon for a range of temperatures and densities within the pressure range.

With this data it is possible to create a polynomial surface fit with third order terms of the reduced density and fifth order terms of the reduced internal energy (Υ). After performing the regression analysis, the terms of least significance were removed to obtain equation (5.10). Using this equation we obtain the estimated temperature values, which are compared to the actual values. The errors between actual and estimated values are shown in Figure 45. The maximum temperature error is 3.37%.

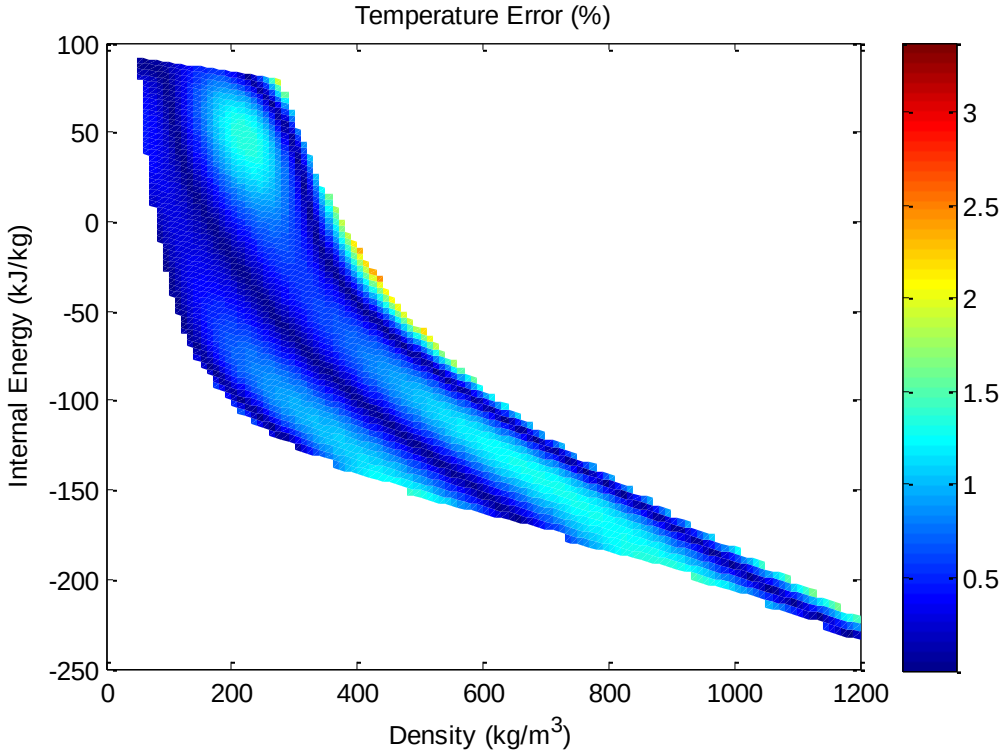

Figure 45: Temperature error as a function of internal energy and density

$$\tau_e = \frac{T_c}{T_e} = a_{00} + a_{01}\Upsilon + a_{20}\delta^2 + a_{02}\Upsilon^2 + a_{30}\delta^3 + a_{21}\delta^2\Upsilon + a_{12}\delta\Upsilon^2 + a_{03}\Upsilon^3 + a_{31}\delta^3\Upsilon + a_{13}\delta\Upsilon^3 + a_{04}\Upsilon^4 + a_{05}\Upsilon^5 \quad (5.10)$$

$$\Upsilon = \frac{U_m}{RT_c} \tag{5.11}$$

a_{00}	0.2978	a_{30}	0.2612	a_{31}	0.01224
a_{01}	-0.05599	a_{21}	0.03005	a_{13}	0.00221
a_{20}	-0.2452	a_{12}	-0.006018	a_{04}	0.0003733
a_{02}	0.01101	a_{03}	-0.002303	a_{05}	-4.215e-5

Table 7: Temperature estimation equation coefficients

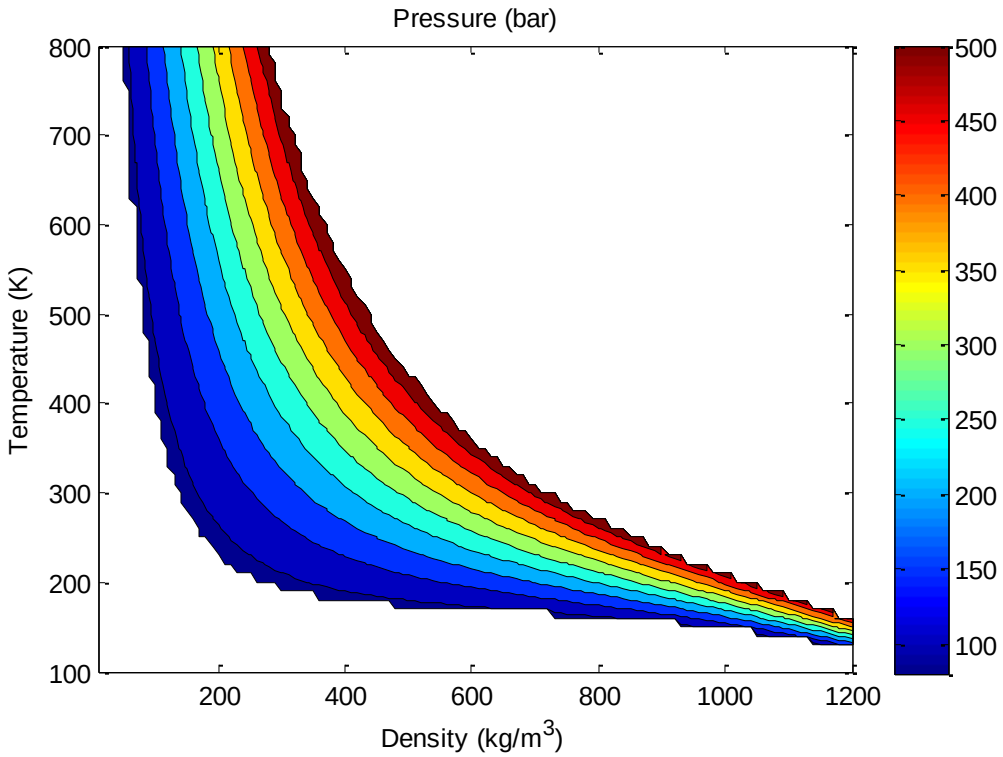

Figure 46: Pressure values as a function of temperature and density

The pressure can be calculated using equation (5.7), and results are shown in Figure 46. Since equation (5.7) has high computational overhead a new pressure equation (5.12) is created based on a modified version of the BWR equation. This equation uses the estimated temperature instead of the specific internal energy to calculate the estimated pressure since the form of the pressure equation is known with respect to density and temperature. Figure 47 shows that

the pressure error only becomes large at the maximum and minimum pressure values of this data set. This should not be a problem since the accumulator does not operate in those regions. It is important to note that the pressure error includes the error due to the temperature estimation.

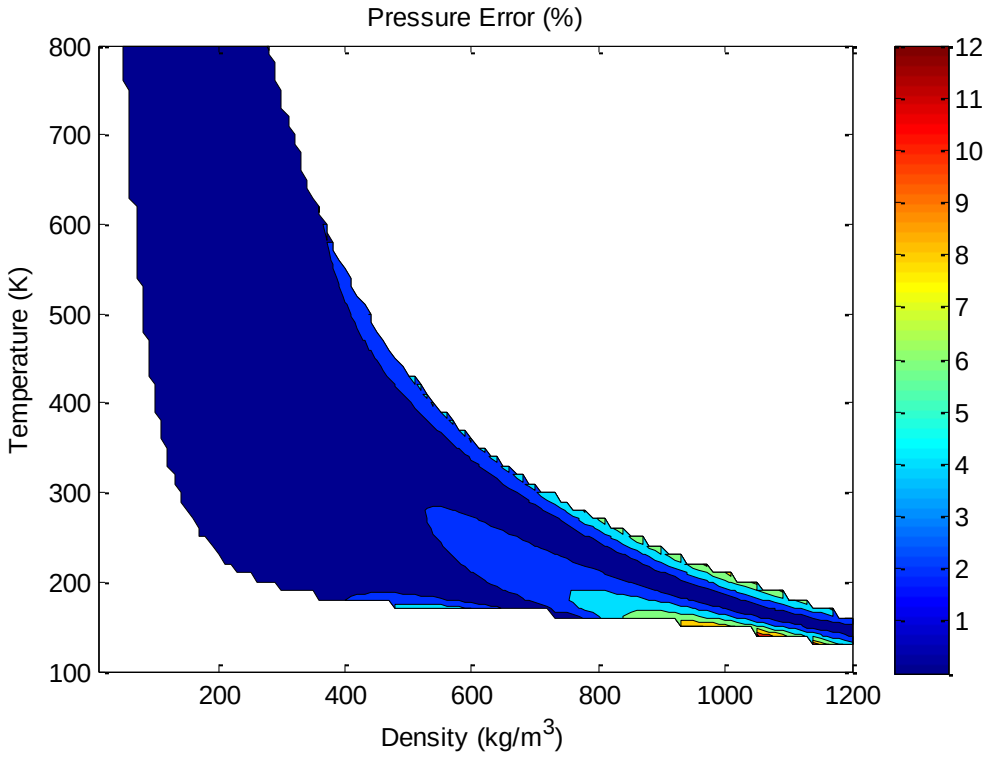

Figure 47: Pressure error as a function of temperature and density

$$\frac{p_e}{\rho R T_e} = 1 + b_1\delta - b_2\delta\tau_e - b_3\delta\tau_e^3 + b_4\delta^2 - b_5\delta^2\tau_e + b_6\delta^5\tau_e + b_7\delta^2\tau_e^3(1 + b_8\delta^2)\,exp(-b_8\delta^2) \tag{5.12}$$

b_1	0.4583	b_4	0.1984	b_7	0.1969
b_2	1.27	b_5	-0.02313	b_8	0.7712
b_3	0.3421	b_6	0.02698		

Table 8: Pressure estimation equation coefficients

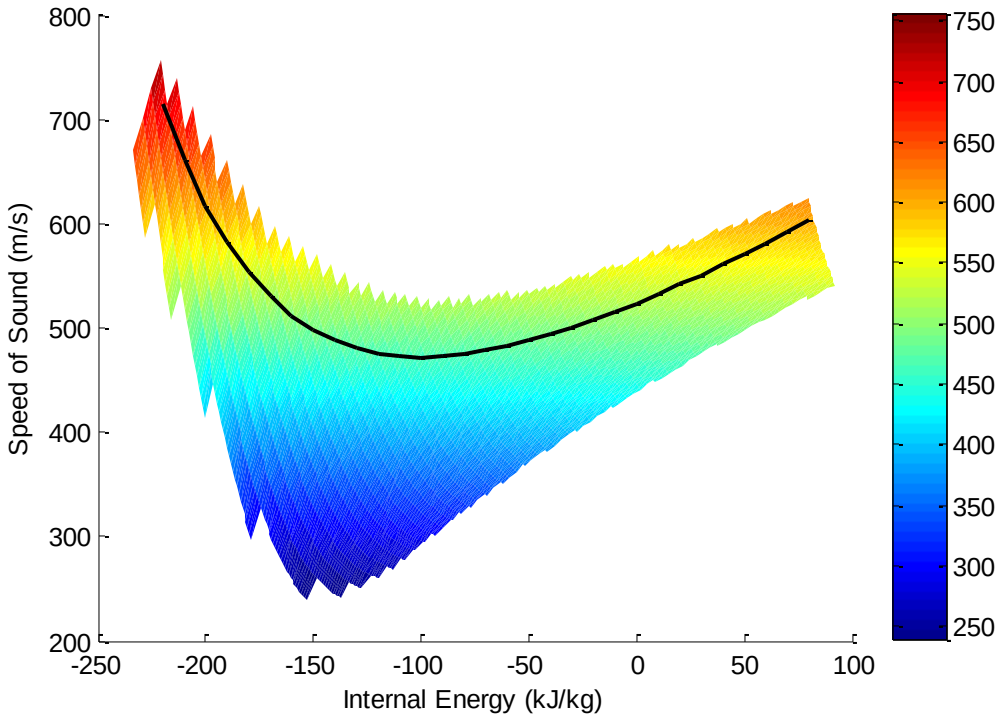

Figure 48: Speed of sound values and estimation as a function of internal energy

$$a_e = c_1\, exp(c_2 I) + c_3 exp(c_4 I) \tag{5.13}$$

c_1	8.515	c_2	-0.01725	c_3	514.9	c_4	0.001936

Table 9: Speed of sound estimation coefficients

The last value that needs to be estimated is the speed of sound. This thermodynamic property is not needed directly in order to solve the conservation equations, but it is required to calculate the Courant-Friedrichs-Lewy Stability Criterion. Since the thermally boosted accumulator model was implemented using a fixed step solver, the CFL criteria was only used to indicate whether the simulation time step was small enough to capture the acoustic waves. Therefore, it does not seem prudent to develop a complicated polynomial equation to estimate the exact speed of sound. To this end equation (5.13) is developed to estimate the speed sound as a function of internal energy at 400 bar, which is the

maximum operating pressure of the accumulator. This approach is in the end calculating the worst case scenario. The estimated speed of sound is shown in Figure 48 as the black line. It must be noted that the coefficients in Table 9 can only be used with internal energy values with units of kJ/kg.

The behaviors of three other thermodynamic properties are investigated as a function of pressure and temperature. These properties are the heat capacity, fluid viscosity, and thermal conductivity and their values were obtained from [**43**]. The heat capacity is the only property which can be estimated using the Maxwell thermodynamic relations. The other properties must be obtained from experimental look up tables. The properties are then combined to obtain the Prandtl number shown in the next section.

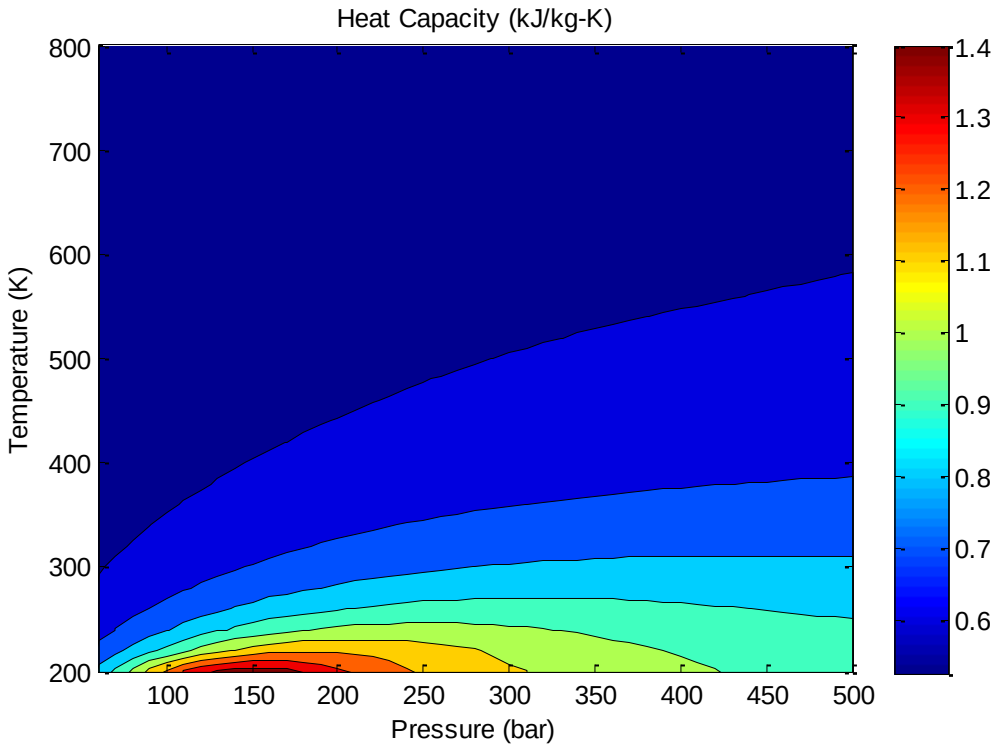

Figure 49: Heat capacity as a function of temperature and pressure

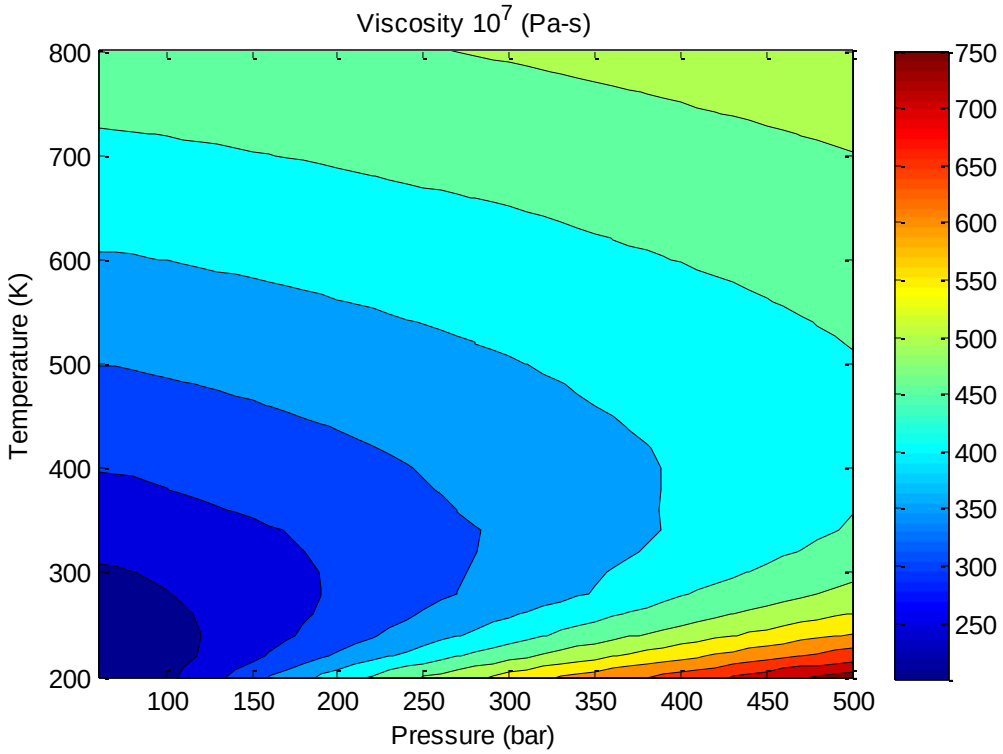

Figure 50: Fluid viscosity as a function of temperature and pressure

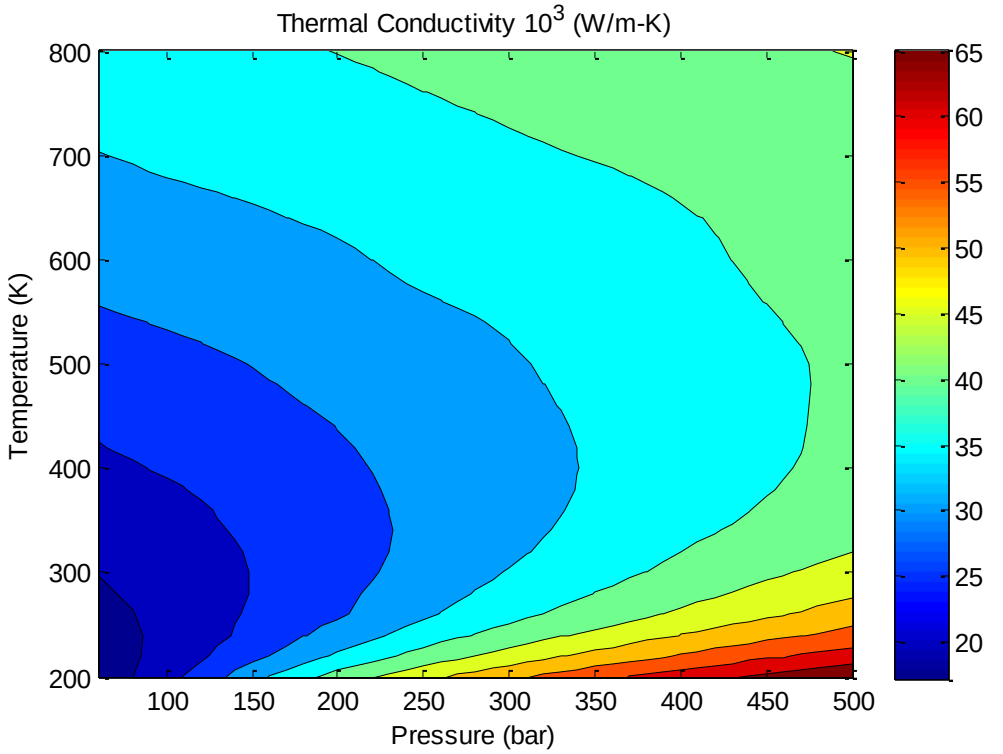

Figure 51: Fluid thermal conductivity as a function of temperature and pressure

Real versus Ideal Gas Comparison

In this chapter we showed how various thermodynamic equations can be used to find the temperature and pressure for a real gas. In this section we use the ideal gas equations to predict the specific internal energy and pressure, and then we compare these results to those of the real gas equations to understand its accuracy implications.

The ideal gas pressure and specific internal energy can be calculated using equations (5.14) and (5.16). To obtain the ideal gas specific internal energy, equation (5.15) must be simplified by calculating the derivative of equation (5.14) at constant density. Integrating the ideal specific internal energy equation yields equation (5.17) which shows that the internal energy for an ideal gas is only a function of temperature. Equation (5.18) gives the ideal specific heat capacity at constant volume for the argon gas.

$$p = \rho RT \tag{5.14}$$

$$dI = C_v dT - \left[T\left(\frac{\partial p}{\partial T}\right)_\rho - p \right] \frac{\partial \rho}{\rho^2} \tag{5.15}$$

$$dI = C_v^0 dT \tag{5.16}$$

$$I_2 - I_1 = C_v^0 (T_2 - T_1) \tag{5.17}$$

$$C_v^0 = \frac{3}{2} R \tag{5.18}$$

Using the equations above it is possible to compare the pressure and internal energy values between the real and the ideal gas model. The errors between the real and ideal models are shown in Figure 52 for the pressure

estimation and Figure 53 for the specific internal energy. These figures illustrate that the accuracy of ideal gas model is poor due to the large errors in pressure and specific internal energy.

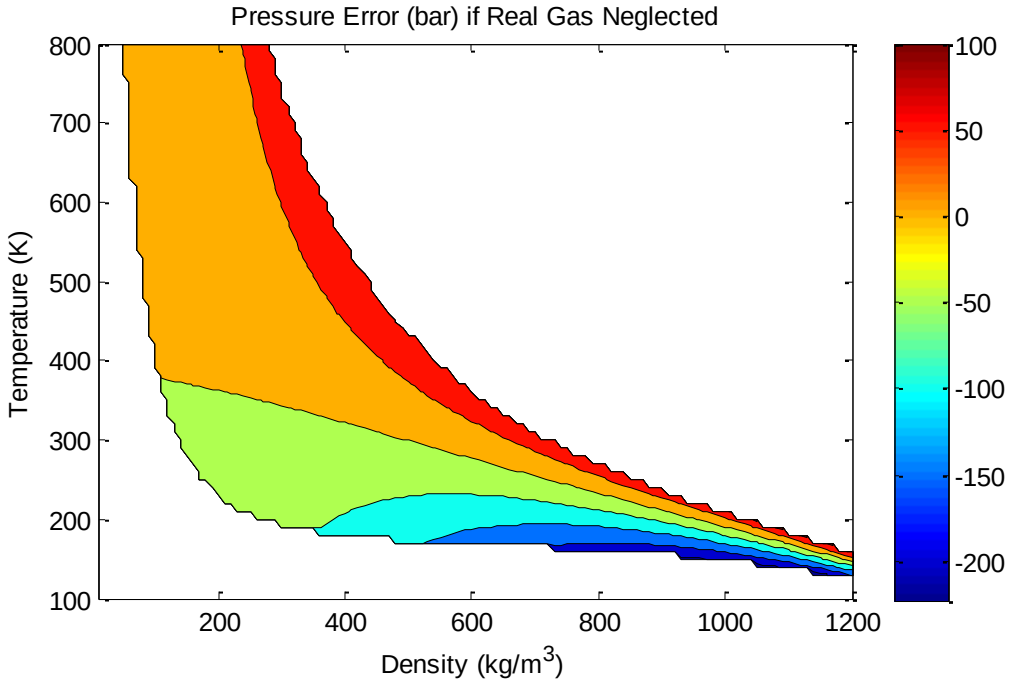

Figure 52: Pressure error between the ideal and real gas estimations

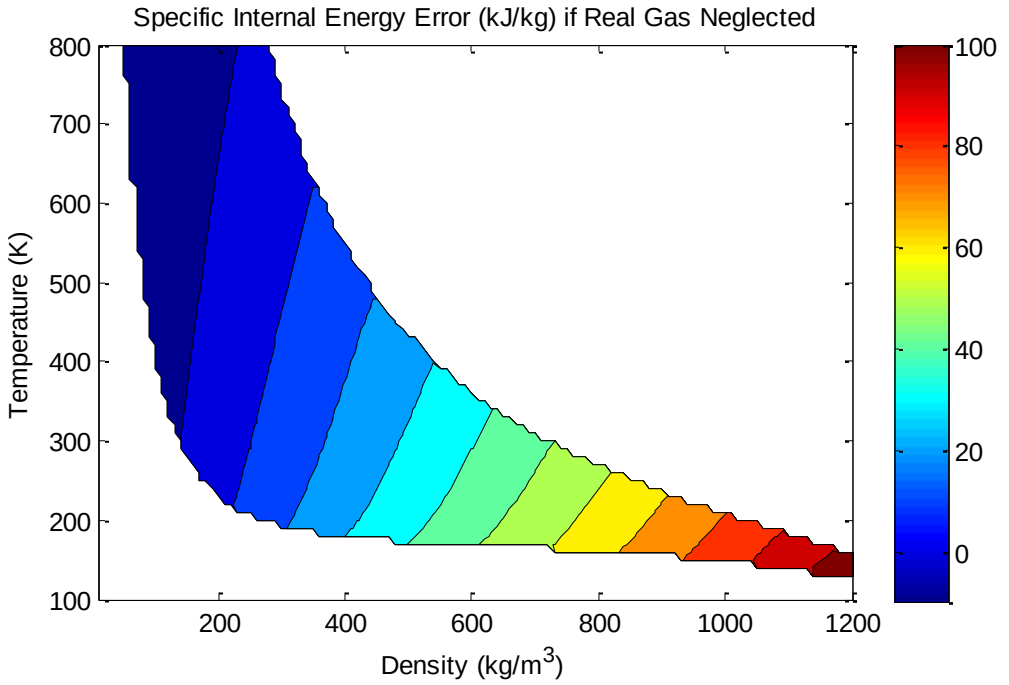

Figure 53: Specific internal energy error between the ideal and real gas estimations

Heat Exchanger Model

A literature search for highly efficient heat exchangers shows that several methods are available. Among them the most promising are the heat exchangers using a nano-porous layer, and the open-cell metal foams.

Nano-porous layer heat exchangers are made by etching the surface of a metal with acid forming the nano-porous layer. This layer improves the heat transfer because the effective surface area increases significantly. Kunugi et al. [**44**] compared the heat transfer between a standard channel, and a channel containing a nano-porous layer. The results showed that the porous layer device had around 200% more heat transferred. The benefit of this heat exchanger is that heat transfer is improved with very little extra pressure loss when compared to normal channel flow. However, this method of heat transfer may not be the most desirable for the thermally boosted accumulator since only the outer layer of the flow is interacting with the heat exchanger.

Open-cell metal foams can be used in a pipe or channel as a heat exchanger. This device is attractive because it has low density, large surface area in small volumes, high strength, and it increases the heat transfer coefficient. Boomsma et al. [**45**] estimates that the surface area to volume ratio may be in the order of 10,000 m^2/m^3. Lu et al. [**16**] conducted a thermal analysis of metal-foam filled heat exchangers in a pipe. Figure 54 shows open-cell metal foams which have been co-sintered with metal pipes.

Figure 54: Open-cell metal foam pipes with different porosities [16]

The open-cell metal foam heat exchangers will impact the flow of the fluid by increasing the frictional force and heat transfer. To investigate these properties Lu et al. [**16**] defined the conservation equations assuming steady state flow in the axial direction with no flow in the radial or angular direction. The momentum equation is based on the Brinkman extended Darcy model [**46**] while the energy equations for the fluid and solid are based on the heat transfer model by Calmidi et al. [**47**]. All thermophysical properties of the solid and fluid are used as constants.

$$0 = -\frac{dp}{dx} + \frac{\mu}{\varepsilon}\left(\frac{\partial^2 u}{\partial r} + \frac{1}{r}\frac{\partial u}{\partial r}\right) - \frac{\mu}{K}u \tag{5.19}$$

$$0 = k_{se}\left(\frac{\partial^2 T_s}{\partial r^2} + \frac{1}{r}\frac{\partial T_s}{\partial r}\right) - h_{sf}\tilde{a}(T_s - T_f) \tag{5.20}$$

$$\varepsilon\rho_f C_f u\frac{dT_f}{dx} = k_{fe}\left(\frac{\partial^2 T}{\partial r^2} + \frac{1}{r}\cdot\frac{\partial T_f}{\partial r}\right) + h_{sf}\tilde{a}\left(T_s - T_f\right) \tag{5.21}$$

To solve the equations above, it is necessary to define the boundary conditions at the center of the pipe and its outer edge, assuming the flow and temperature are symmetrical about the center of the pipe. Besides the initial conditions, several parameters must be calculated, such as the permeability *K*,

effective thermal conductivities k_{se} and k_{fe}, surface area density $\tilde{a}$, and the heat transfer coefficient h_{sf}.

$$r = R_p, \quad u = 0, \quad T_s = T_f = T_w \tag{5.22}$$

$$r = 0, \quad \frac{\partial u}{\partial r} = \frac{\partial T_f}{\partial r} = \frac{\partial T_s}{\partial r} = 0 \tag{5.23}$$

Equation (5.24) is a formulation by Calmidi [**48**] used to calculate the permeability of metal-foams. The pore diameter can be calculated using the *ppi* (pores per inch) value given by equation (5.25). Lastly the fiber diameter of metal foams can be estimated using equation (5.26) developed by Zhao [**49**].

$$K = 0.00073(1-\varepsilon)^{-0.224}\left(\frac{d_f}{d_p}\right)^{-1.11} \tag{5.24}$$

$$d_p = 0.0254/ppi \tag{5.25}$$

$$d_f = 1.18\, d_p \sqrt{\frac{1-\varepsilon}{3\pi}}\left(\frac{1}{1-e^{-\left(\frac{(1-\varepsilon)}{0.04}\right)}}\right) \tag{5.26}$$

To calculate the effective thermal conductivity of open-cell metal foams Boosma and Poulikakos [**50**] created a correlation based on three-dimensional cellular morphology of metal foams, shown in (5.27). To obtain the effective thermal conductivity of the solid, k_{se}, equation (5.27) can be solved by setting the thermal conductive of the fluid to zero. The same can be done to find the effective thermal conductivity of the fluid, k_{fe}, by setting the thermal conductivity of the solid to zero.

$$k_e = \frac{\sqrt{2}}{2(R_A + R_B + R_C + R_D)} \tag{5.27}$$

$$R_A = \frac{4\lambda}{\left(2\xi^2 + \pi\lambda(1-\xi)\right)k_s + \left(4 - 2\xi^2 - \pi\lambda(1-\xi)\right)k_f}$$

$$R_B = \frac{(\xi - 2\lambda)^2}{(\xi - 2\lambda)\xi^2 k_s + (2\xi - 4\lambda - (\xi - 2\lambda)\xi^2)k_f}$$

$$R_C = \frac{\left(\sqrt{2} - 2\xi\right)^2}{2\pi\lambda^2\left(1 - 2\xi\sqrt{2}\right)k_s + 2\left(\sqrt{2} - 2\xi - \pi\lambda^2\left(1 - 2\xi\sqrt{2}\right)\right)k_f}$$

$$R_D = \frac{2\xi}{\xi^2 k_s + (4 - \xi^2)k_f}$$

$$\lambda = \sqrt{\frac{\sqrt{2}\left(2 - \left(\frac{5}{8}\right)\xi^3\sqrt{2} - 2\xi\right)}{\pi\left(3 - 4\xi\sqrt{2} - \xi\right)}}$$

$$\xi = 0.339$$

Heat exchangers are usually made by using cylindrical tubes to increase the surface area between the solid and fluid. The best possible orientation using cylindrical tubes would be to have three cylinders perpendicular to each other and equally spaced between their intersections. With the geometry shown in Figure 55, the area density is approximately $3\pi d/a^2$. However, the topology of metal foams is not similar to that of cross cylinders. To circumvent this problem Calmidi [**48**] suggests using the correlation given in equation (5.29).

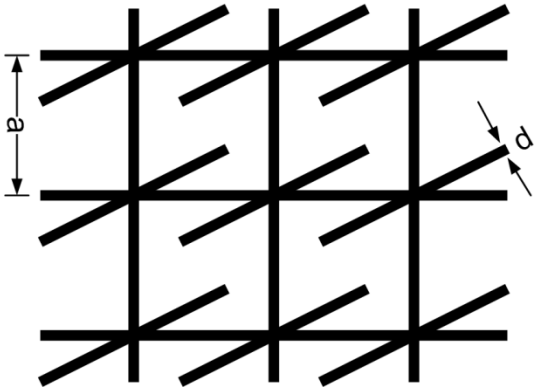

Figure 55: Heat exchanger tube distribution

$$a = 0.59 d_p$$

$$d = \left(1 - e^{-\left(\frac{1-\varepsilon}{0.04}\right)}\right) d_f \tag{5.28}$$

$$\tilde{a} = \frac{3\pi d_f \left(1 - e^{-\left(\frac{1-\varepsilon}{0.04}\right)}\right)}{\left(0.59 d_p\right)^2} \tag{5.29}$$

The interfacial heat transfer coefficient is the last parameter that needs to be estimated, however, no correlations currently exist to predict this value. Lu et al. [**16**] and Camildi et al. [**47**] suggest the use of a correlation developed by Zukauskas [**51**], which is valid for staggered cylinders, shown in equation (5.30). To estimate the heat transfer coefficient the localized Reynolds number is calculated using equation (5.31) and the shape factor defined in (5.28).

$$Nu_{sf} = \frac{h_{sf} d}{k_f} = \begin{matrix} 0.76 Re_d^{0.4} Pr^{0.37}, & (1 \le Re_d \le 40) \\ 0.52 Re_d^{0.5} Pr^{0.37}, & (40 \le Re_d \le 10^3) \\ 0.26 Re_d^{0.6} Pr^{0.37}, & (10^3 \le Re_d \le 2 \cdot 10^5) \end{matrix} \tag{5.30}$$

$$Re_d = \frac{u d \rho}{\mu} \tag{5.31}$$

After defining these parameters it is possible to express equations (5.19), (5.20), and (5.21) in dimensionless form. The dimensionless conservation of momentum is shown in (5.32) while the dimensionless conservation of energy equations are shown in (5.33) and (5.34). The dimensionless variables are defined from equation (5.35) to (5.39). The differential equations constants are show in (5.40).

$$U = -P + \frac{Da}{\varepsilon}\left(\frac{\partial^2 U}{\partial \psi} + \frac{1}{\psi}\frac{\partial U}{\partial \psi}\right) \tag{5.32}$$

$$0 = \frac{\partial^2 \theta_s}{\partial \psi^2} + \frac{1}{\psi}\frac{\partial \theta_s}{\partial \psi} - D\left(\theta_s - \theta_f\right) \tag{5.33}$$

$$2U = C\left(\frac{\partial^2 \theta_f}{\partial \psi^2} + \frac{1}{\psi}\frac{\partial \theta_f}{\partial \psi}\right) + D\left(\theta_s - \theta_f\right) \tag{5.34}$$

$$\psi = r/R_p \tag{5.35}$$

$$U = u/u_m \tag{5.36}$$

$$P = \frac{K}{\mu u_m}\frac{dp}{dx} \tag{5.37}$$

$$\theta_s = \frac{T_s - T_w}{\dot{Q}_w'' R/k_{se}} \tag{5.38}$$

$$\theta_f = \frac{T_f - T_w}{\dot{Q}_w'' R/k_{se}} \tag{5.39}$$

$$Da = K/R_p^2, \quad D = h_{sf}\tilde{a}R_p^2/k_{se}, \quad C = k_{fe}/k_{se} \tag{5.40}$$

The dimensionless differential equations above are known as Bessel differential equations. These equations have a known analytical solution which can be expressed with modified Bessel functions, $J_\alpha(z)$.For more information on the solution methods of these functions refer to the Appendix section of [**16**]. Using these methods, Lu et al. [**16**] obtained the analytical solution of the dimensionless conservation equations summarized below.

$$U = P\frac{J_0\left(\sqrt{\frac{\varepsilon}{Da}}\psi\right)}{J_0\left(\sqrt{\frac{\varepsilon}{Da}}\right)} - P \tag{5.41}$$

$$P = \frac{J_0\left(\sqrt{\frac{\varepsilon}{Da}}\right)}{2\sqrt{\frac{Da}{\varepsilon}}J_1\left(\sqrt{\frac{\varepsilon}{Da}}\right) - J_0\left(\sqrt{\frac{\varepsilon}{Da}}\right)} \tag{5.42}$$

$$\theta_f = \frac{2P}{C+1}\left(\frac{1-\psi^2}{4} + \frac{Da/\varepsilon}{J_0\left(\sqrt{\frac{\varepsilon}{Da}}\right)}J_0\left(\sqrt{\frac{\varepsilon}{Da}}\psi\right) + B - A - \frac{Da}{\varepsilon}\right.$$

$$\left. - \frac{B}{J_0\left(\sqrt{\frac{(C+1)D}{C}}\right)}J_0\left(\sqrt{\frac{(C+1)D}{C}}\psi\right)\right. \tag{5.43}$$

$$\left. + \frac{A}{J_0\left(\sqrt{\frac{\varepsilon}{Da}}\right)}J_0\left(\sqrt{\frac{\varepsilon}{Da}}\psi\right)\right)$$

$$\theta_s = 2P\left(\frac{1-\psi^2}{4} + \frac{Da/\varepsilon}{J_0\left(\sqrt{\frac{\varepsilon}{Da}}\right)}J_0\left(\sqrt{\frac{\varepsilon}{Da}}\psi\right) - \frac{Da}{\varepsilon}\right) - C\theta_f \tag{5.44}$$

$$A = \frac{1}{C\cdot\frac{\varepsilon}{Da} - (C+1)D}, \qquad B = \frac{C\cdot\frac{\varepsilon}{Da}}{(C+1)D\left(C\frac{\varepsilon}{Da} - (C+1)D\right)}$$

Using these solutions it is possible to define equations which predict the pressure drop, friction factor, and the overall heat transfer coefficient of metal foams. The overall heat transfer coefficient is the most critical of these calculations, as this value can be used to calculate the estimated heat transfer into the fluid by using the wall temperature of the solid and bulk fluid temperature.

In summary, the friction and heat transfer effects of the foam can be estimated without considering the temperature and speed profile as a function of radius.

$$\frac{dp}{dx} = \frac{\mu u_m}{K} P \tag{5.45}$$

$$f = \frac{8P}{Da \cdot Re} \tag{5.46}$$

$$Nu = \frac{\bar{h}}{k_f} 2R_p = -\frac{2}{\left(k_f/k_{fe}\right) C \theta_{f,b}} \tag{5.47}$$

$$\theta_{f,b} = \frac{T_{f,b} - T_w}{\dot{Q}_w'' R_p / k_{se}} = 2 \int_0^1 U \theta_f \psi d\psi \tag{5.48}$$

The ultimate goal of using these equations is to correctly predict the heat transfer and friction effects of a metal foam heat exchanger for the purpose of the one dimensional CFD analysis. There are seven factors that can affect heat transfer: pipe radius, foam porosity, foam pores per inch, heat conduction coefficient of the solid and fluid, the Reynolds number, and the Prandtl number. From these factors only the Reynolds number and Prandtl number change during the simulation due to the change in speed and thermodynamic properties of the fluid. All of the remaining factors are constants since they do not change during the operation of the heat exchanger. Even though the thermal conductivity of the fluid will change depending on the pressure and temperature, for the purpose of heat transfer the conduction coefficient of the fluid is set to 21.1e-3 W/m-K. This value is a conservative estimate for the heat conduction of argon gas at 100 bar pressure and 300 K temperature given by Vargaftik [**43**], and shown on Figure

51. The value also happens to be the lowest heat conduction value of the gas for any temperature between the operating pressures of 100 to 400 bar.

With the fluid conductivity now selected a method must be used to quantify the heat transfer effect based on the remaining factors. In the following analysis equation (5.47) is used to calculate the overall effective convection heat transfer coefficient. To solve this equation the dimensionless bulk temperature of (5.48) is numerically integrated using the values from (5.41) and (5.43). Figure 56 shows how the convective heat transfer coefficient, $\overline{h}$, changes as function of Reynolds number and Prandtl number. The effect of these variables is of particular importance since the Reynolds number and Prandtl number change depending on the fluid state.

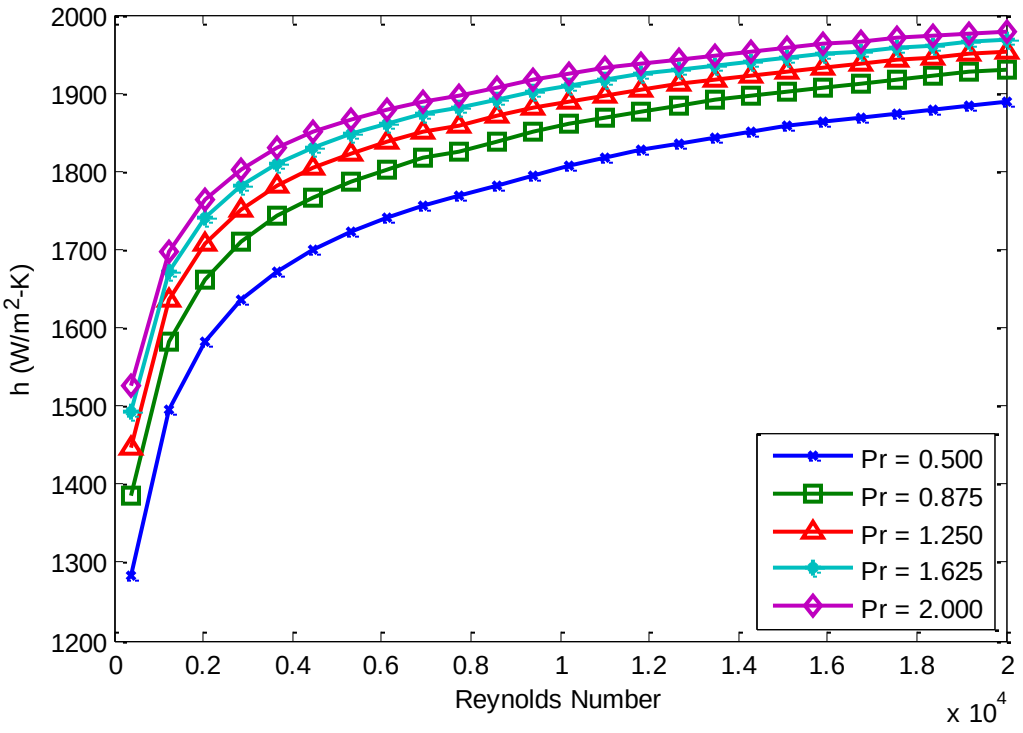

Figure 56: Overall convective heat transfer coefficient as a function of Re and Pr

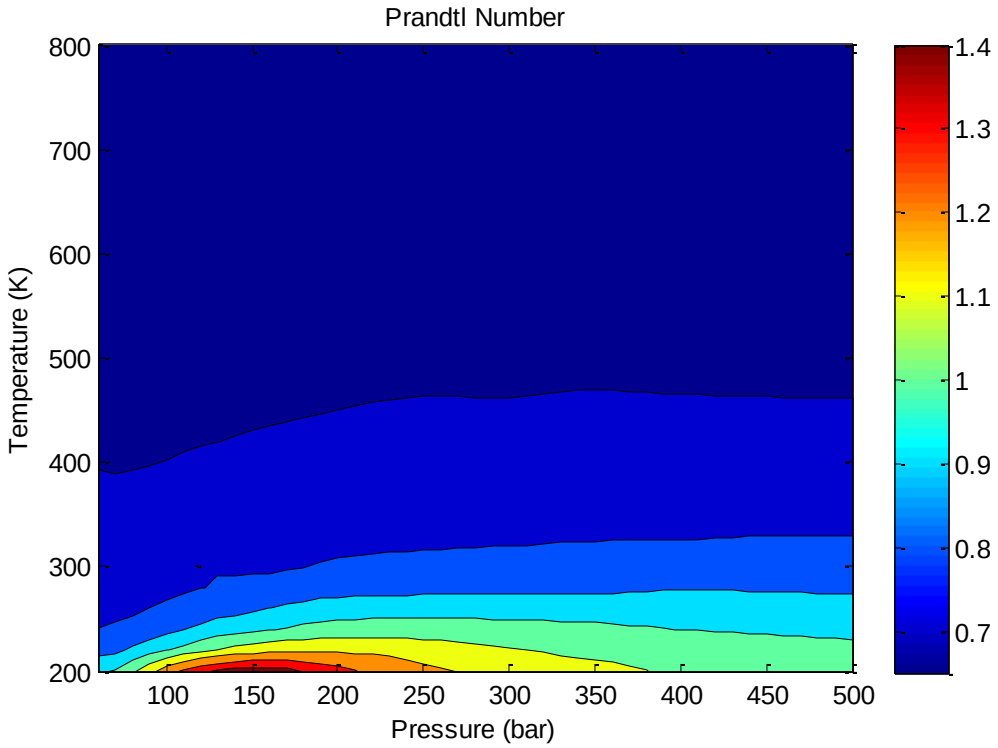

Figure 57: Prandtl number as a function of temperature and pressure

$$Pr = \frac{C_p \cdot \mu}{k_f} \tag{5.49}$$

Parameters	Values	Units
ε	0.90	
ppi	30	
k_f	21.3e-3	(W/m-K)
k_s	200	(W/m-K)
R	10	(mm)

Table 10: Constant parameters for convective heat transfer coefficient estimation

To create Figure 56 the Prandtl and Reynolds number was varied while keeping the parameters in Table 10 constant. The heat capacity, viscosity and heat conduction values of the previous section were used to estimate the Prandtl number as a function of fluid pressure and temperature. Figure 57 shows the range of Prandtl numbers for the accumulator operating conditions. It is seen

from this figure that the Prandtl number does not change drastically. Prandtl numbers between 0.65 to 1.4 do not seem to significantly impact the heat transfer coefficient; therefore a constant Prandtl number value of 0.849 will be used in subsequent analysis.

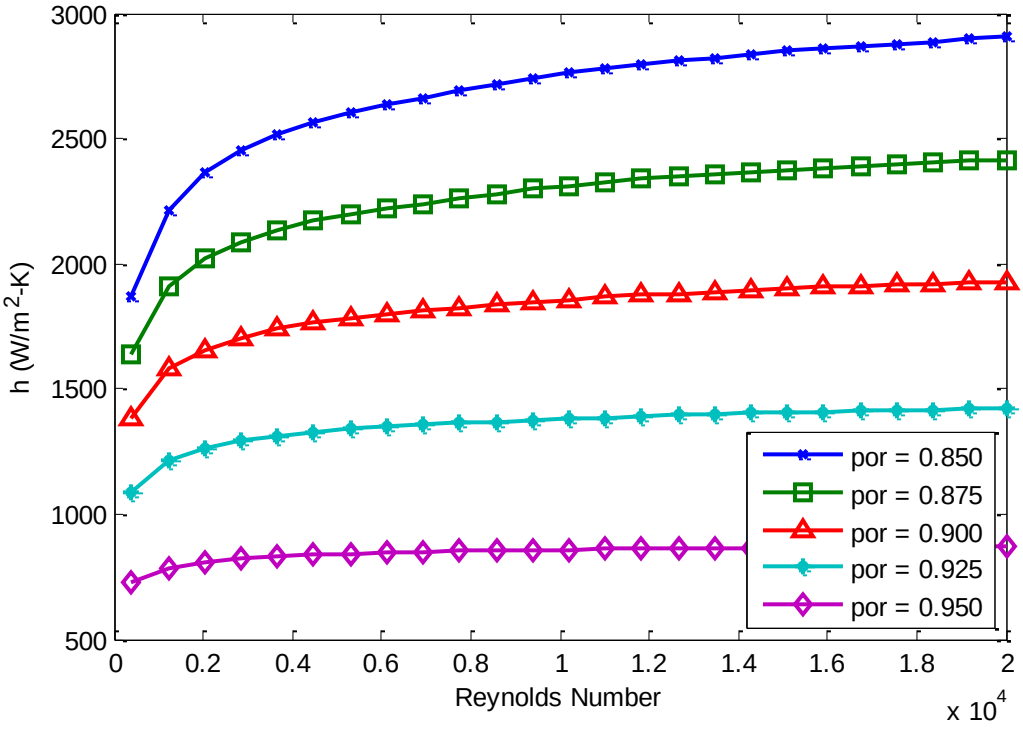

Figure 58: Effect of porosity on the overall heat transfer coefficient

In order to understand how the heat transfer coefficient changes as a function of other parameters, the previous study is repeated by alternating some parameters while maintain the rest constant, as shown on Table 10. Figure 58 shows that the heat transfer coefficient increases as porosity decreases. This is understandable since the metal density increases as the porosity decreases creating more surface interactions between the fluid and the metal. A similar effect can be seen in Figure 59 since the heat transfer coefficient increases as

the pore density increases. It stands from reason that as the pores decrease in effective diameter more fluid will interact with the surface of the solid.

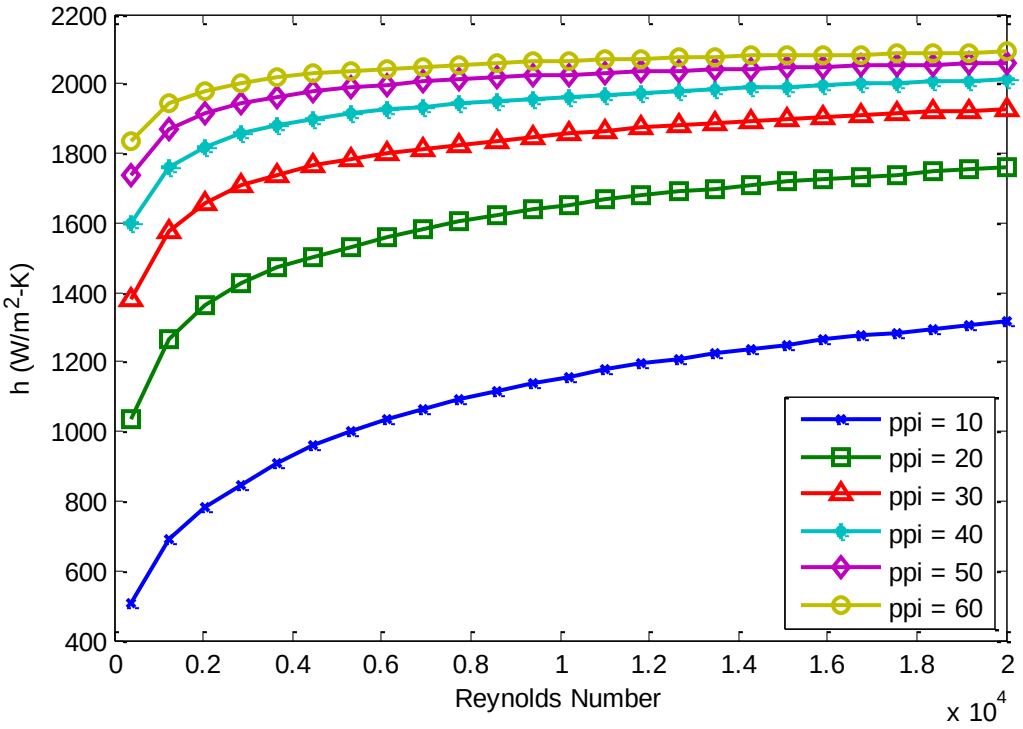

Figure 59: Effect of pore density on the overall heat transfer coefficient

The final parameters to be considered are the thermal conductivity of the metal, and the radius of the heat exchanger. As shown in Figure 60, the thermal conductivity of the metal has a large impact on the heat transfer coefficient. To obtain thermal conductivities higher then 300 W/m-K copper, gold, or silver alloys must be used. If a thermal conductivity of 200 W/m-K is desired, aluminum, and beryllium alloys can be used. However, given that gold, silver and beryllium are extremely expensive the only realistic choices are copper and aluminum alloys.

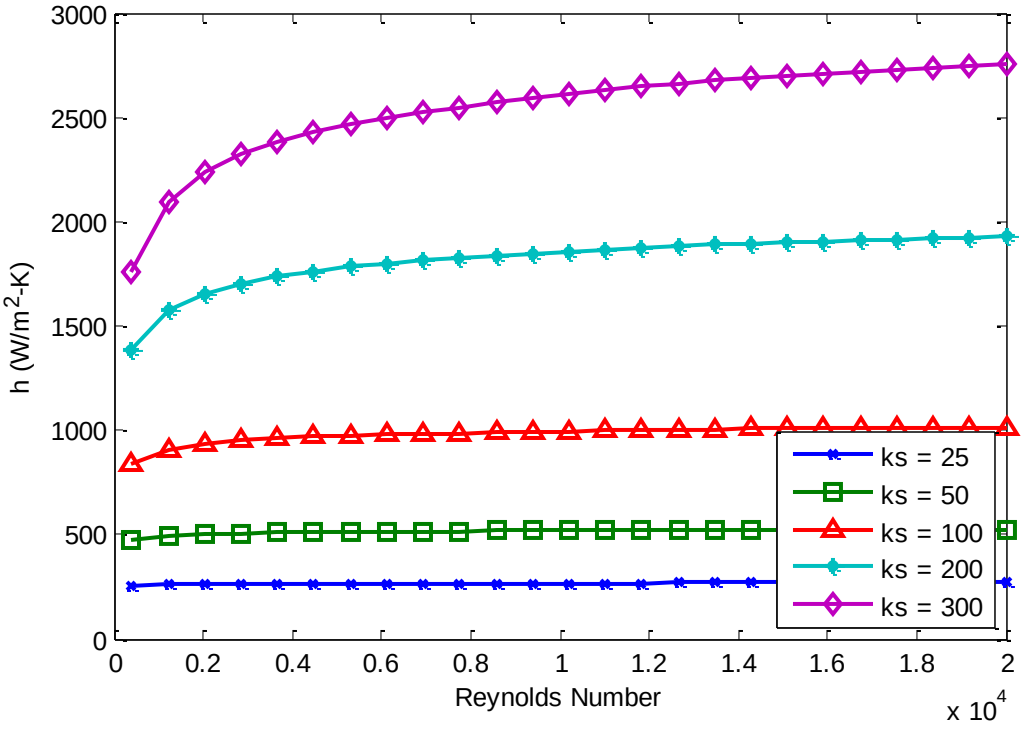

Figure 60: Effect of metal conductivity on the overall convective heat transfer coefficient

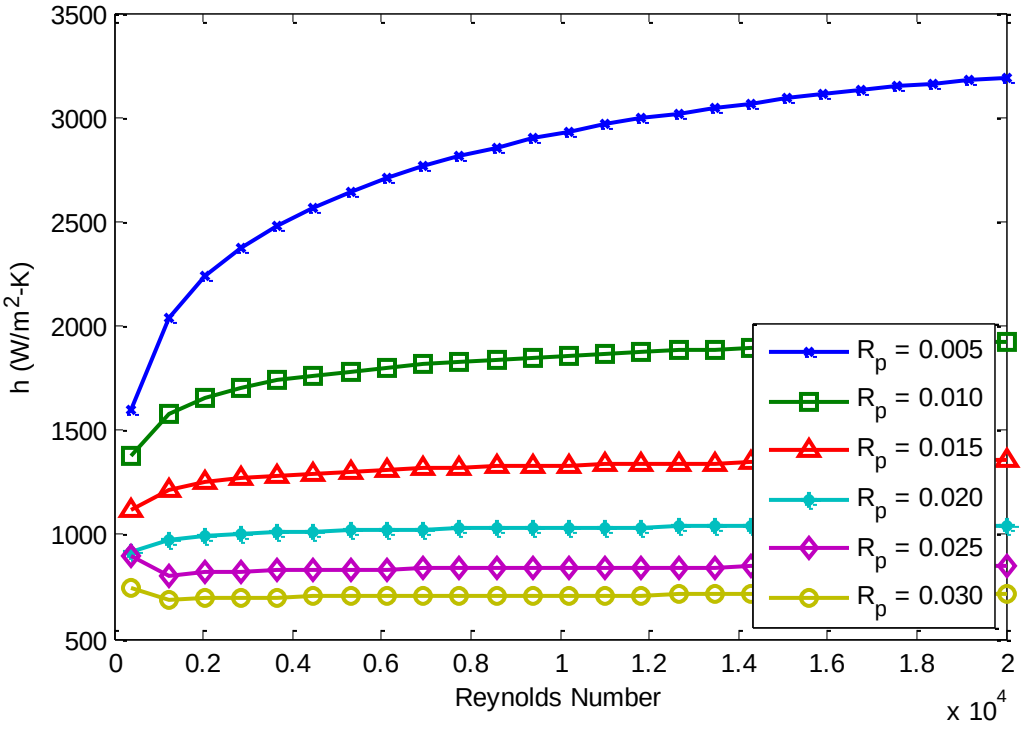

Figure 61: Effect of pipe radius on the overall convective heat transfer coefficient

Increasing the pipe radius seems to decrease the convective heat transfer coefficient. To investigate this behavior further, equation (5.43) and (5.44) are used to calculate the temperature distribution across the pipe radius, shown in Figure 62. It seems that as the radius increases the solid and fluid temperatures are further away from the wall temperature values (at r/R_p = 1). Furthermore, the difference between the solid and fluid temperature is considerably smaller for large pipe radius. This mechanism may have the largest impact on the heat transfer coefficient as this temperature difference will dictate the heat transfer to the fluid. It must be noted that even though the overall convective heat transfer coefficient decreases, the total heat transfer may not since the heat transfer surface area increases with the pipe diameter.

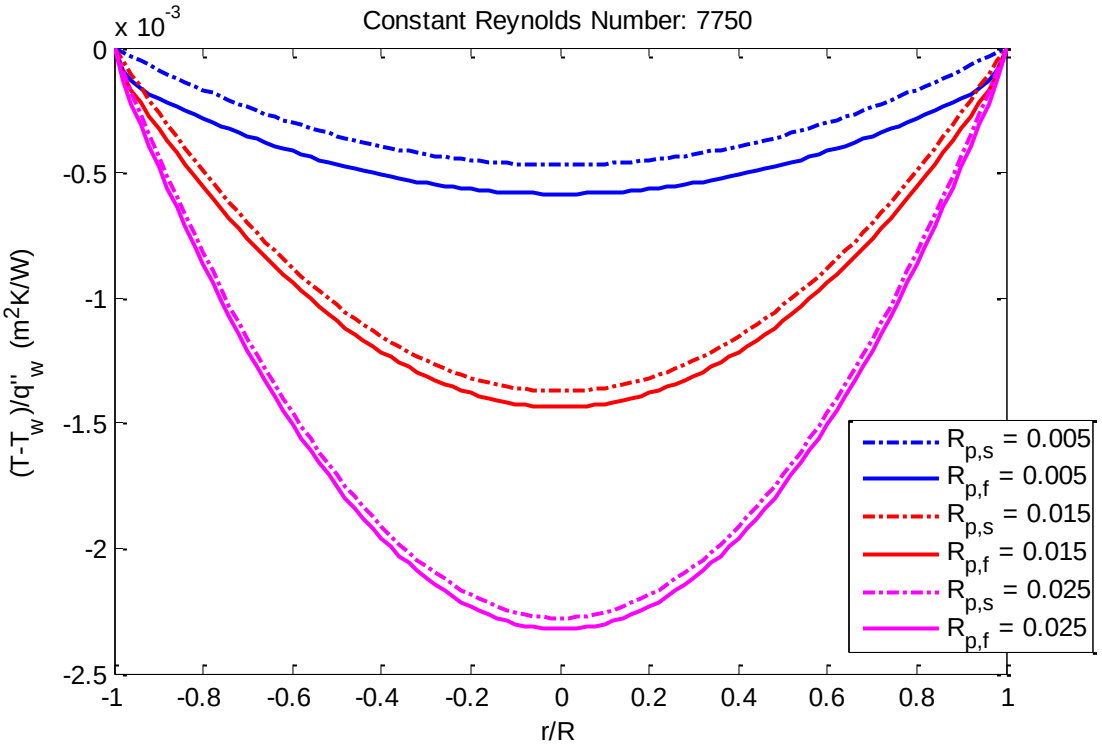

Figure 62: Temperature distribution of fluid and solid for various pipe radiuses

To verify the validity of the metal foam heat transfer models, Lu et al. [**16**] compared the heat transfer coefficient difference between experimental and measured results, shown in Figure 63, of six different samples, Table 11. These results show that there is good agreement between the estimated and measured values, with the analytical models reporting more conservative estimates. With the information presented in this chapter is possible to calculate the convective heat transfer coefficient as a function of Reynolds number. The other variables will be treated as constant parameters input to the model.

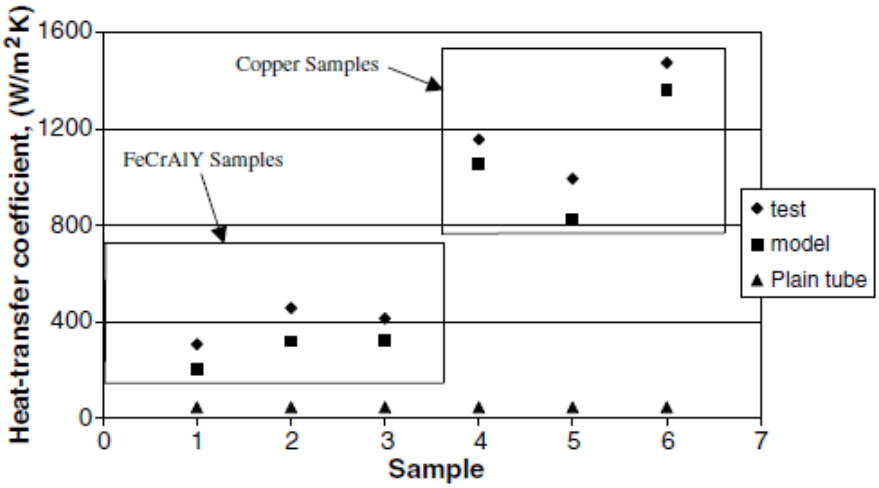

Figure 63: Heat transfer coefficients for different samples: estimated versus measured [16**]**

Sample	1	2	3	4	5	6
Foam	FeCrAlY	FeCrAlY	FeCrAlY	Copper	Copper	Copper
Pore size (ppi)	10	10	30	10	30	60
Porosity	0.943	0.857	0.898	0.933	0.956	0.943
k_s (W/m-K)	26	20	20	310	300	320

Table 11: Summary of microstructures and thermal conductivities of compared samples [16**]**

CHAPTER VI

Thermally Boosted Accumulator Analysis and Results

Nomenclature

D	Pipe diameter
g	Gravitational acceleration
H	Effective height
$\bar{h}$	Overall convective heat transfer coefficient
k	Fluid thermal conductivity
L	Distance between nodes
$\overline{Nu}_D$	Nusselt number with respect to pipe diameter
$\overline{Nu}_L$	Nusselt number with respect to distance
p	Gas pressure
Pr	Prandtl number
r_0	Accumulator outer shell radius
r_i	Accumulator inner shell radius
Ra_D	Rayleigh number with respect to pipe diameter
Ra_L	Rayleigh number with respect to distance
Re	Reynolds number
T_s	Accumulator shell temperature
T_∞	Ambient temperature
v	Kinematic viscosity
α	Thermal diffusivity
β	Expansion coefficient
σ_a	Axial stress

Model Implementation

To analyze the thermally boosted accumulator potential, it is necessary to combine all of the tools created in the previous chapters of the dissertation into a single model. The initial focus of this model is to understand the impact of gas dynamics and heat transfer on the performance of the accumulator. For this reason, the thermally boosted accumulator is split into three sections, as shown in Figure 64. The first section is the *constant volume chamber* designed to house the majority of the gas prior to expansion. Next, the *hot heat exchanger runner* is used to accelerate fluid and increase its temperature via the heat exchanger. The last part of the model is the *bladder chamber*, where the gas is compressed and expanded during the cycles.

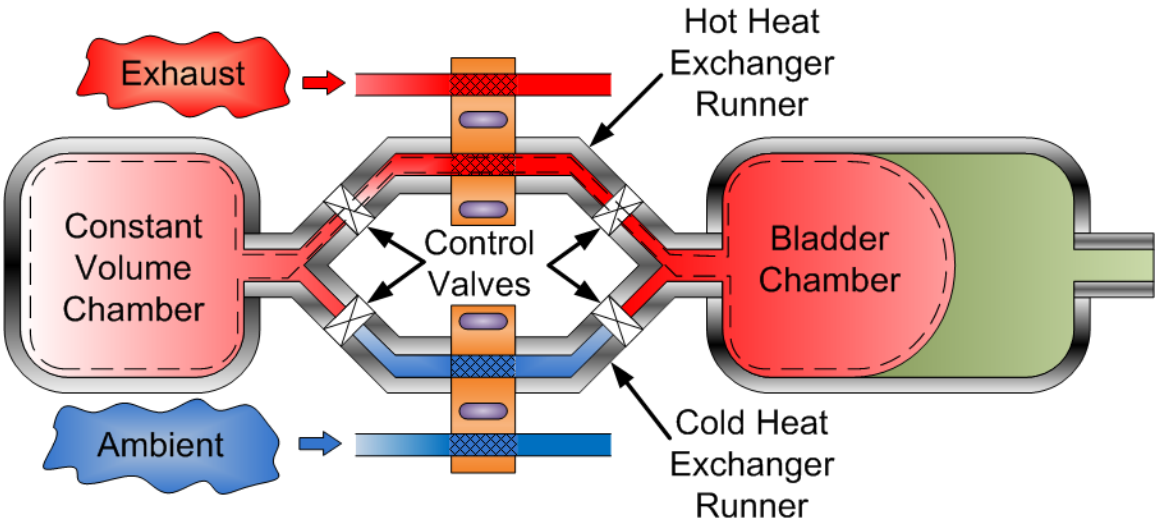

Figure 64: Thermally boosted accumulator conceptual design

It is important to note that in this initial analysis the effects of the exhaust, ambient and phase change materials are not considered. This is done so to facilitate the investigation and maintain focus on critical design features. Therefore, a constant temperature heat source of 500 K is used throughout our

analysis. The dashed lines in Figure 64 highlight the components included in our study.

Geometrical Properties	Values	Units
Constant Volume Chamber Diameter	230	(mm)
Hot Heat Exchanger Runner Diameter	52.7	(mm)
Effective Runner Diameter	50.0	(mm)
Bladder Chamber Diameter	230	(mm)
Constant Volume Discretization Width	42.5	(mm)
Hot Runner Discretization Width	10.0	(mm)
Initial Bladder Chamber Discretization Width	5.0	(mm)
Final Bladder Chamber Discretization Width	106.0	(mm)
Constant Volume Chamber Volume	11.0	(L)
Hot Runner Volume (gas volume)	0.47	(L)
Initial Bladder Chamber Volume	1.74	(L)
Final Bladder Chamber Volume	18.52	(L)

Table 12: Thermally Boosted Accumulator geometrical properties

Table 12 quantifies the dimensions of the components we use to create the simulation version of the thermally boosted accumulator. Since we use one dimensional CFD code to analyze this problem, the thermally boosted accumulator model needs to be discretized into a number of control volumes. We use three sets of control volume widths in our model. In the constant volume chamber and the bladder chamber the control volume widths are much larger than the widths used in the heat exchanger runner. This is done to increase the simulation speed as the fluid velocities of this section are smaller due to the large diameter. Figure 65 gives a graphical representation of how the control volumes are aligned with their control volume centers shown in the zero radius axes.

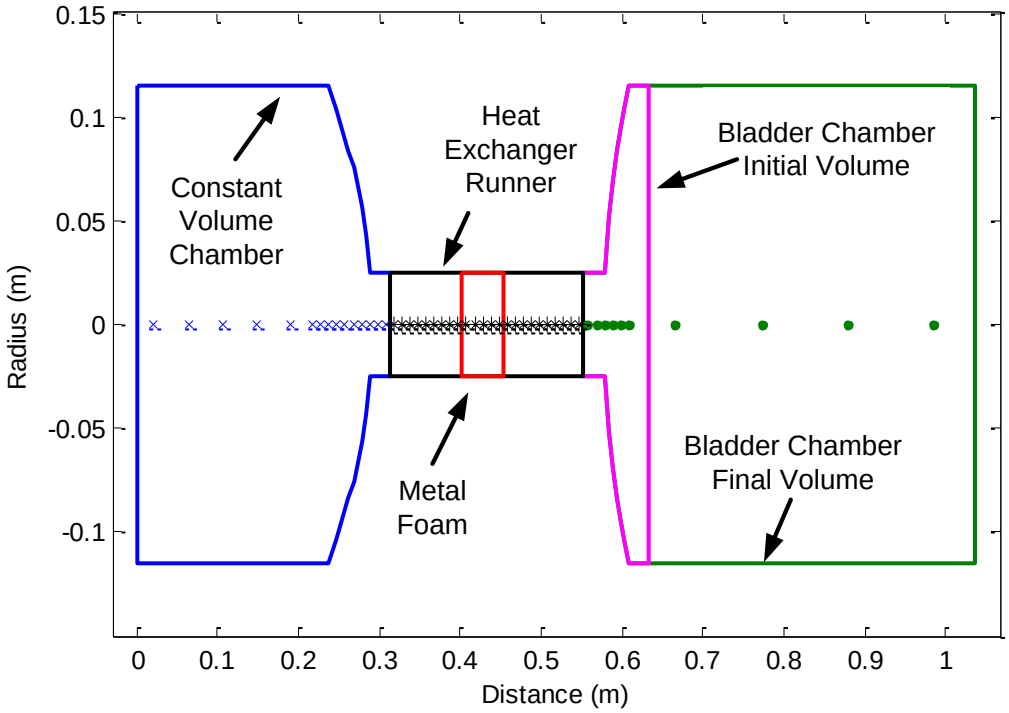

Figure 65: Simulation representation of the Thermally Boosted Accumulator design (Figure 64)

Foam Properties	Values	Units
Number of Foam Control Volume Nodes	5	(-)
Porosity	0.90	(-)
Pores Per Inch	30	(ppi)
Metal Conduction Coefficient	200	(W/m-K)
Heat Transfer Area Density	3887	(m^2/m^3)
Heat Transfer Area	0.424	(m^2)

Table 13: Hot heat exchanger runner foam properties

Equations (5.46) and (5.47) are used to implement the heat transfer and friction aspects of the metal foam. The foam parameters selected in this study are meant to reflect an average open cell metal foam and are set to medium porosity and pores per inch values, as shown in Table 13. Another important factor is the thermal conductivity of the metal, and the value shown in Table 13 reflects the impact of aluminum foam.

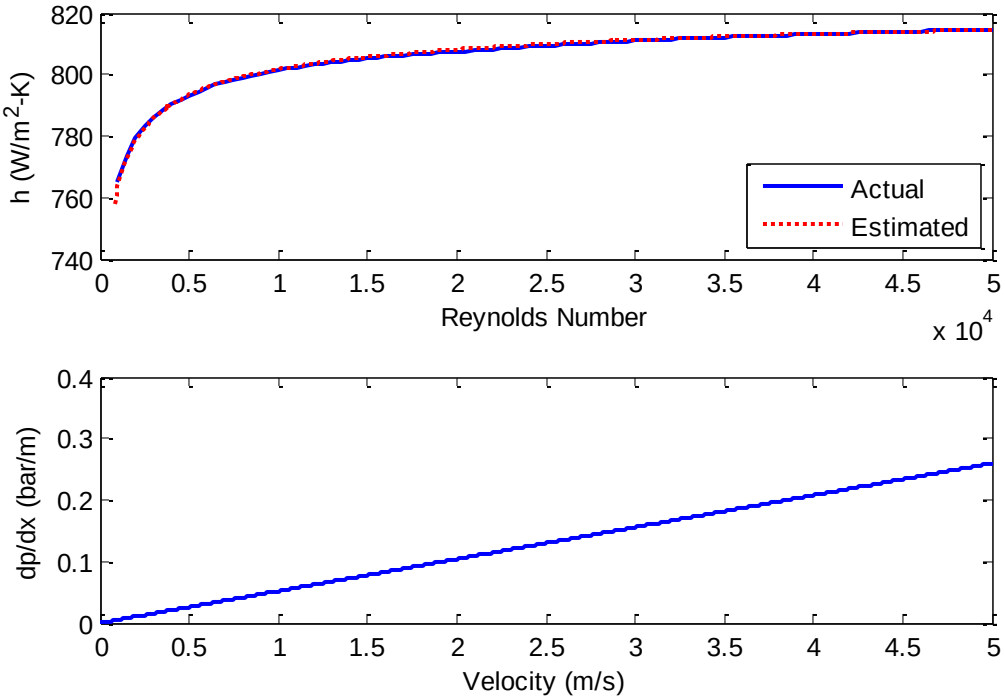

Figure 66: Heat transfer and friction implications of the selected open cell metal foam

In order to calculate the heat transfer coefficient of the metal foam heat exchanger, one can use the equations presented in the Heat Exchanger Model section of the dissertation. However, this method is severely inefficient as it requires analytical solution of the steady state conservation equations using Bessel functions. An alternative method is to use the constant parameters to create an overall convection coefficient versus Reynolds number curve, shown in Figure 66. The estimated values shown in this figure are calculated using equation (6.1), while equation (5.45) is used to calculate the pressure drop per length of the metal foam.

$$\bar{h} = 830.4 - 852.1 \cdot Re^{-0.3638} \tag{6.1}$$

Transient Operation

Simulation Results at 10 kW Expansion

Based on the models presented in the previous three chapters, we simulate the thermally boosted accumulator to evaluate its benefits and drawbacks. The results presented below show the initial change in the thermodynamic states and velocity of the thermally boosted accumulator over a transient heating period of 100 milliseconds. During this time, a constant temperature heat source of 500 K is present along the heat exchanger, and the energy is obtained from the accumulator at a constant rate of 10 kW.

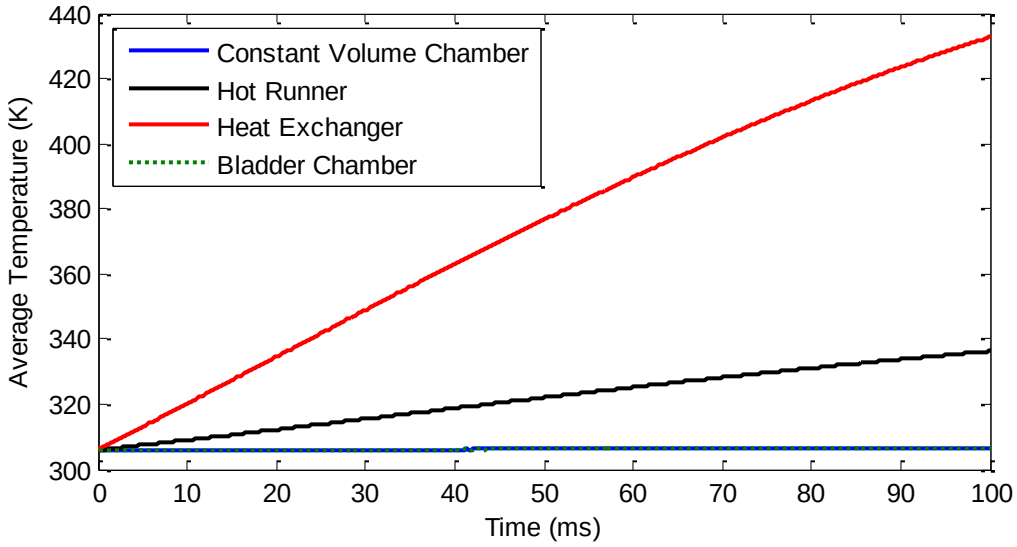

Figure 67: Average fluid temperature of various accumulator sections

Figure 67 illustrates the impact of the heat exchanger on the average fluid temperature. In the initial transient period, the temperature of the fluid increases rapidly nearing the heat sink source temperature. This figure also shows that the temperature of other sections is not affected during this time period. This is

consistent with our expectations, since majority of the fluid mass is located in the larger chambers.

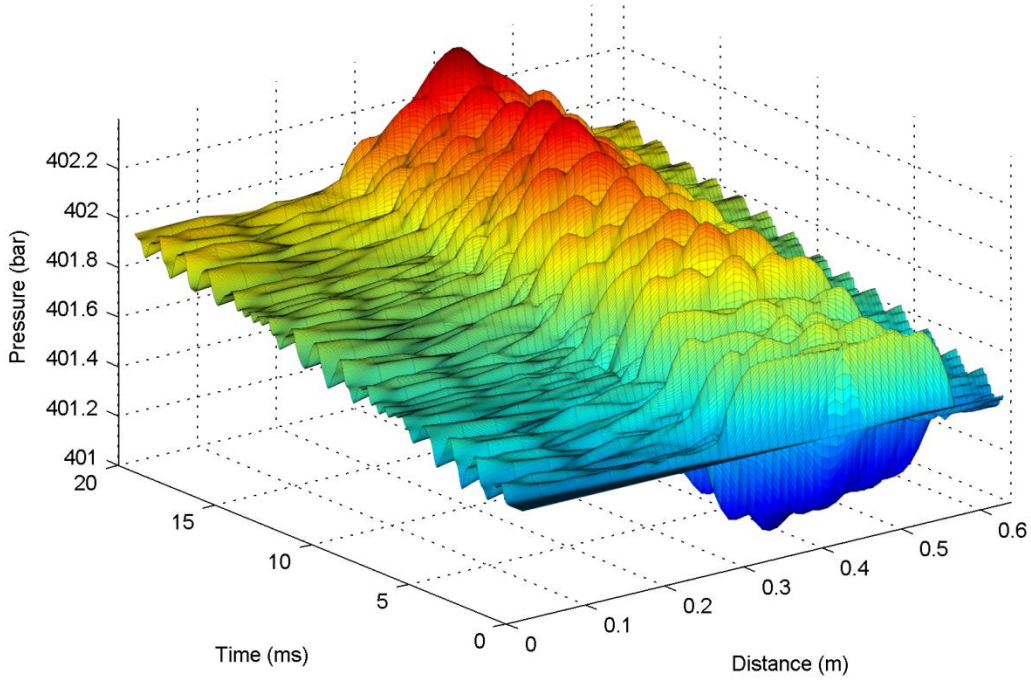

Figure 68: Pressure distribution in space and time

The temperature change of the fluid is a fairly slow process and requires the entire mass of the fluid to interact with the heat exchanger. On the other hand, the pressure changes very quickly due to the acoustic nature of the fluid. As the fluid in the heat exchanger is heated, we observe pressure pulsations, causing mass to leave the heat exchanger and travel to the adjacent chambers. These pressure pulsations are demonstrated in Figure 68. The pressure fluctuations are desirable in our model as they facilitate the interaction of the fluid with the heat exchanger, and as a result, the system pressure increases. The average effect of these pulsations can be seen in Figure 69.

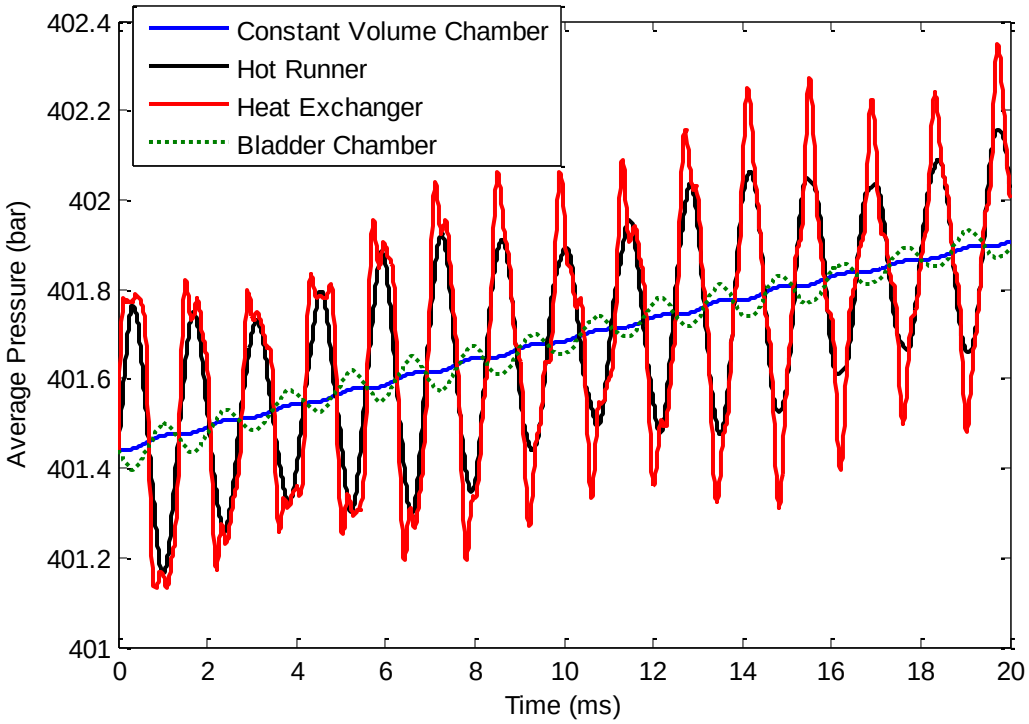

Figure 69: Average fluid pressure of the various accumulator sections

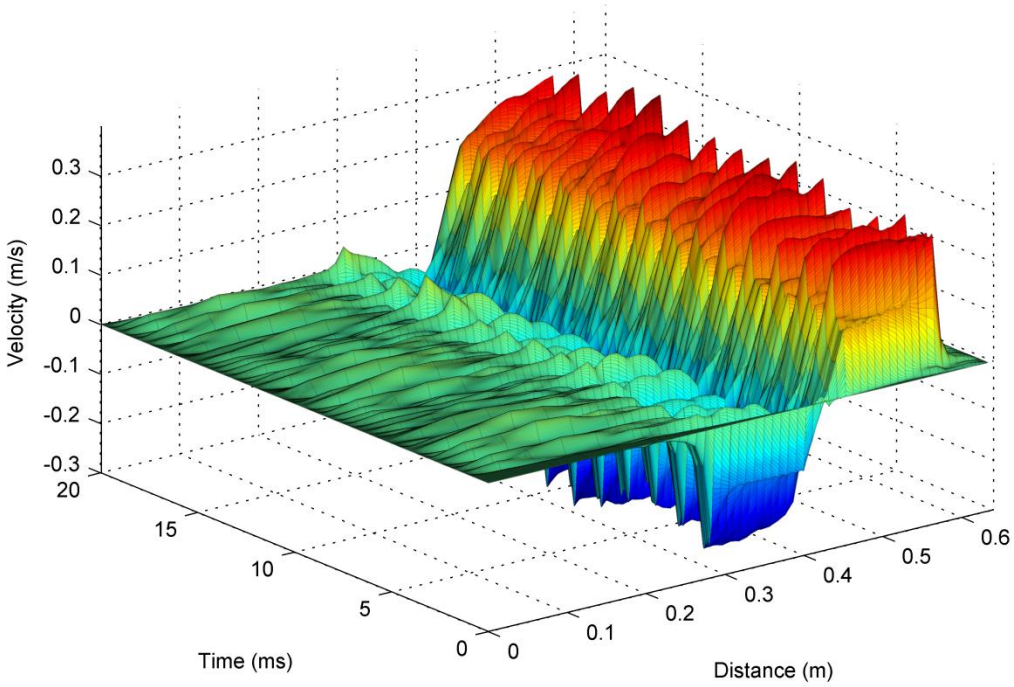

Figure 70: Fluid velocity profile across space and time

The pressure pulsations have direct impact on the velocity profile throughout the thermally boosted accumulator chambers. Figure 70 shows how well these profiles are developed inside the hot runner. The velocities appear to indicate that fluid is leaving the heat exchanger center and moving towards the larger volume sections. This behavior is especially interesting since the accumulator gas volume is expanding during that time, by proving a constant power of 10 kW. This mechanism is mostly driven by fluid density drop in the heat exchanger to maintain the constant pressure level.

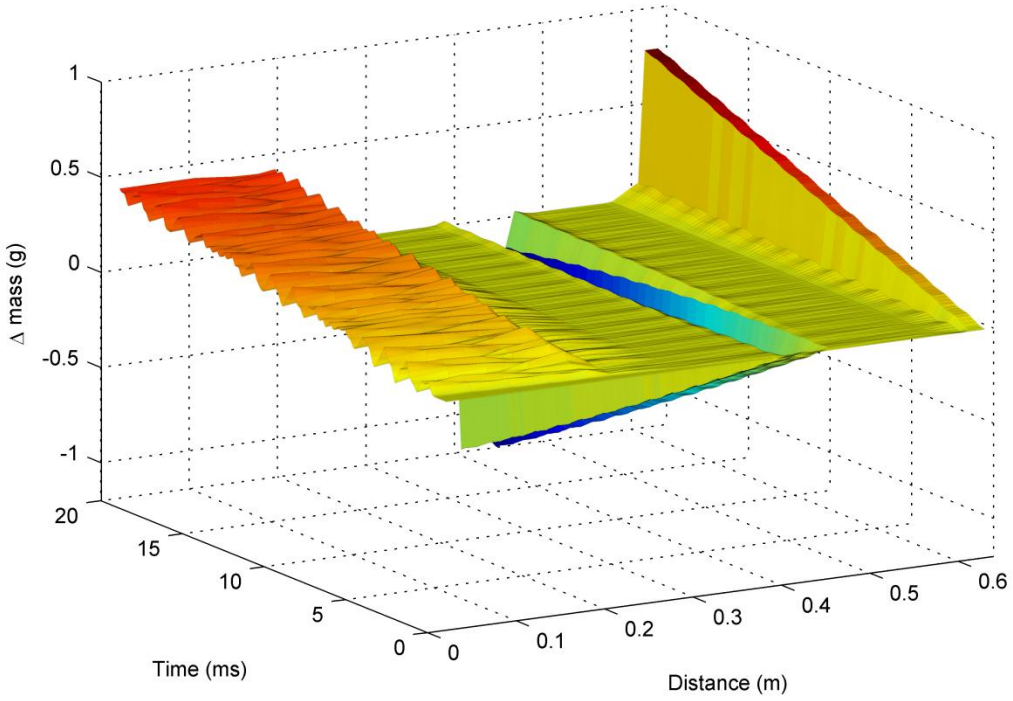

Figure 71: Change in mass distribution across space and time

To fully understand the flow velocity implications, detailed analysis of the mass distribution is required. Due to the extremely small transient period, it is essential to evaluate the change in mass across the accumulator sections. Figure 71 illustrates that a significant amount of mass has moved from the heat

exchanger area towards the larger volume sections of the constant volume chamber and the bladder chamber. It is interesting to note that the hot runner control volumes, outside of the heat exchanger, do not appear to lose much mass. This is the case since more mass is needed in the larger volumes to maintain the pressure levels semi-constant.

The change in mass of the three accumulator sections is illustrated in Figure 72. This figure demonstrates that the heat exchanger is able to maintain and even slightly increase the pressure of the system by supplying the larger chambers with hot fluid. However, since the fluid temperature at the heat exchanger slowly reaches the source temperature, this mass distribution mechanism cannot be sustained for a long period of time.

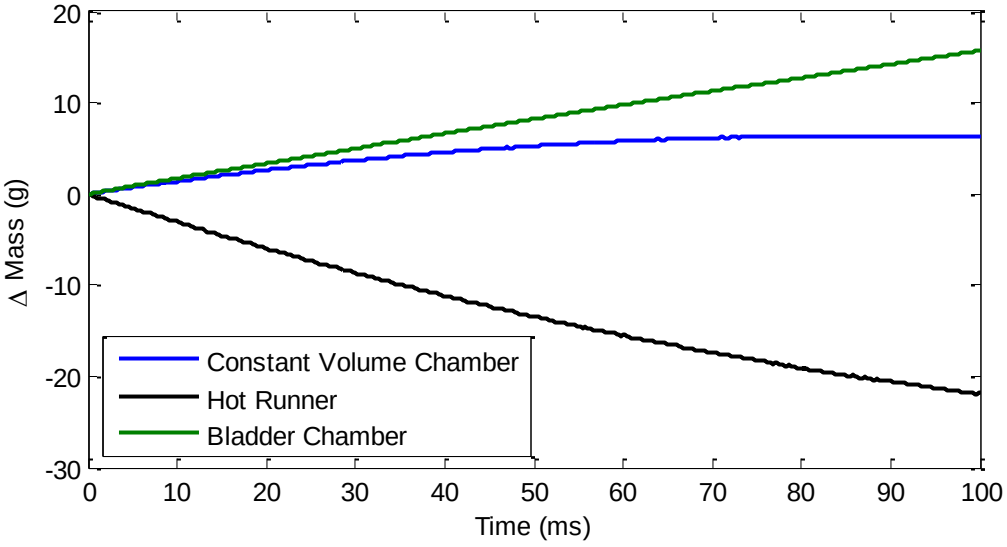

Figure 72: Change in mass of various accumulator sections

This examination of the transient dynamics is essential to the analysis of the proposed system, due to the resulting increase in system pressure. Since our goal is to maintain constant pressure across all sections of the accumulator, the transient results are critical to understanding how this process is achieved.

Steady State Operation

As various combinations of fluid mass and initial volume of a standard accumulator can lead to different energy storage capacities, we develop a standardized process for comparison of the existing accumulator designs to a thermally boosted accumulator. We select a density value that achieves a pressure of 400 bar at room temperature (300 K). The initial volume is selected by ensuring that the final gas volume is equal to 30 L and that the final pressure is slightly higher than 100 bar (the minimum accumulator pressure) while the accumulator energy is discharged at a constant rate of 10 kW.

In the previous section, we show transient results for a simulation time of 0.1 seconds. However, in order to capture all of the acoustic phenomena (i.e., pressure waves) a simulation time step of 10 μs is required. This is also true when simulating to a final time step of 34 seconds, since the acoustic information must be still taken into account. For storage purposes, the data is sampled every millisecond to obtain 34 thousand data points per variable, instead of 3.4 million date points. Using this approach decreases the required storage space for the results, however these results cannot be used to observe the acoustic waves accurately.

Simulation Results at 10 kW Expansion

The thermally boosted accumulator acts in similar fashion to a normal accumulator with respect to its steady state pressure behavior. This can be observed in Figure 73 (a) where the accumulator end pressure drops over time.

The end pressure is defined as the pressure in the last control volume of the bladder chamber, which is the pressure that interacts with the hydraulic fluid. More importantly, the mean and standard deviation of the difference in pressure versus the end pressure demonstrate how the pressure waves are damped out after four seconds (Figure 73 (b)).

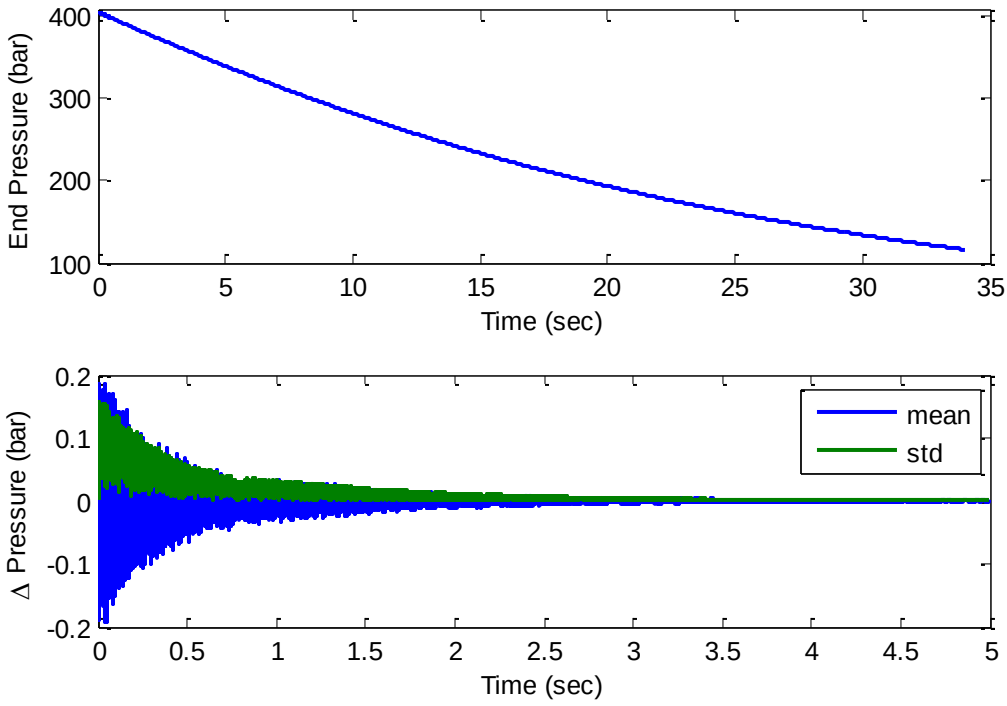

Figure 73: (a) Accumulator end pressure which interacts with the hydraulic fluid (b) mean and standard deviation of change in pressure from the end pressure

The purpose of heating internal gas is to maintain constant pressure and to slow down the pressure drop in order to obtain more energy. However, from observing the pressure information above, it appears that the thermally boosted accumulator acts similarly to a normal accumulator. To investigate this observation, the temperature distribution is plotted in Figure 74. From this figure, the heat exchanger appears to be effectively heating the right side of the accumulator, while the temperature is dropping in left side of the heat exchanger.

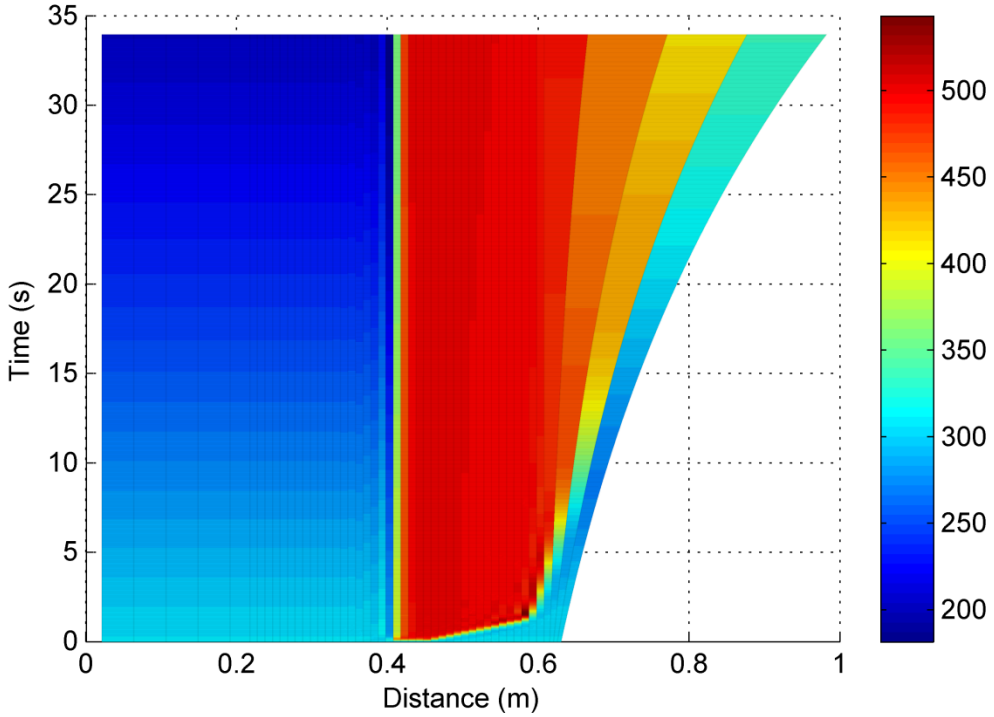

Figure 74: Temperature distribution versus space and time

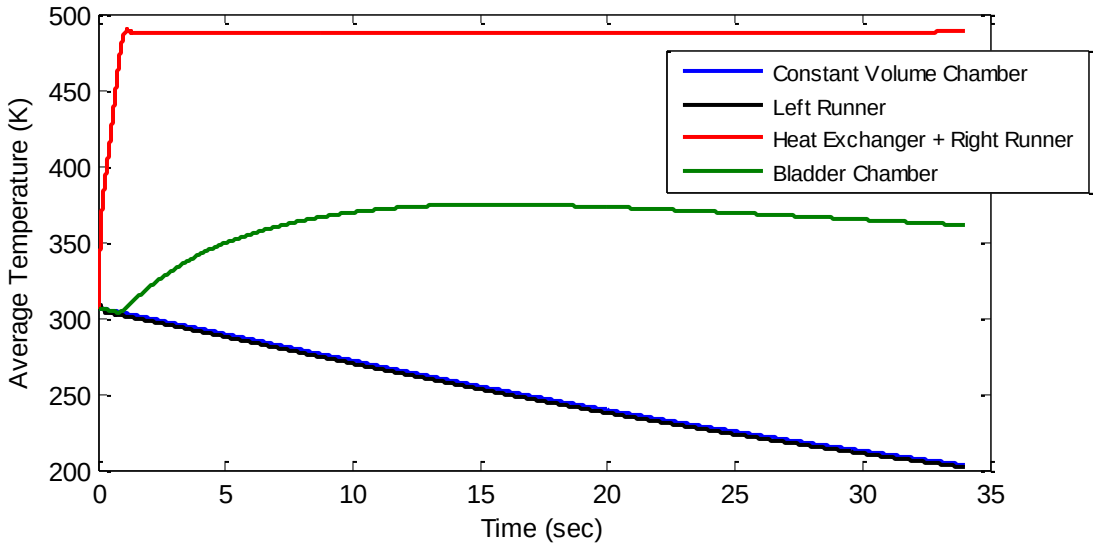

Figure 75: Average temperature over time over various accumulator sections

Figure 75 illustrates how the average temperature of the heat exchanger and right runner increases to almost to 500 K. The average temperature of the bladder chamber also increases due to the constant hot fluid incoming from the

hot runner. However, the average temperature of the constant volume chamber and left runner are significantly lower than the temperature for the rest of the system, which leads to an undesirable behavior explained below.

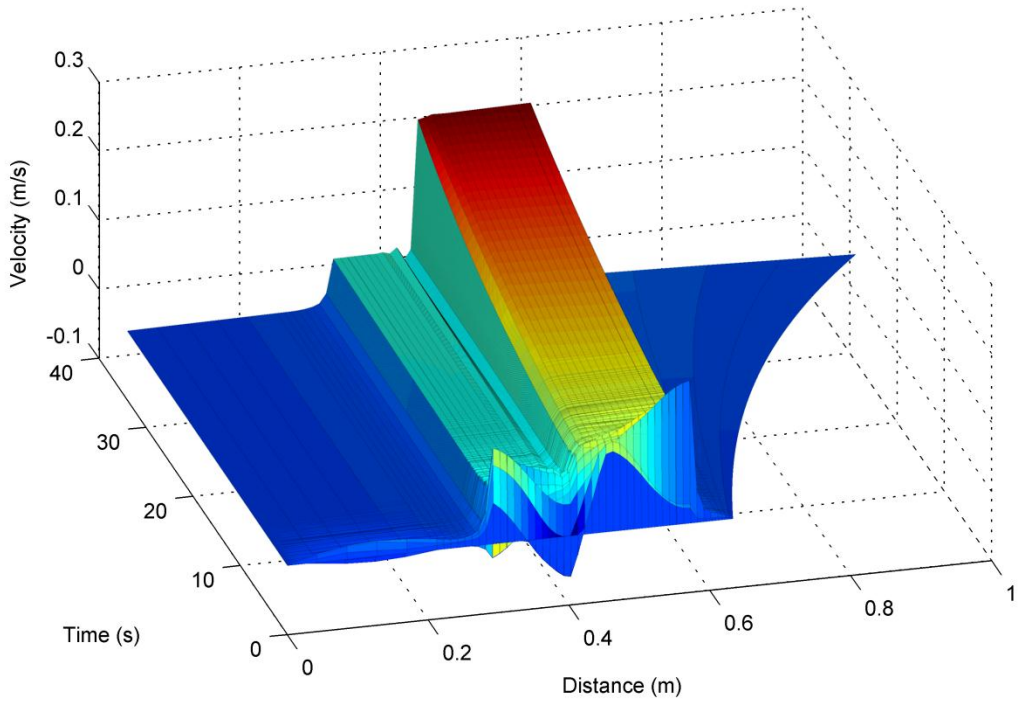

Figure 76: Velocity distribution across space and time

The temperature drop in the constant volume section is due to the one directional fluid flow from left to right. Figure 76 illustrates how fluid speed increases when it enters the runner and then increases again when it enters the heat exchanger. This speed increase in the heat exchanger is caused by the constant mass flow rate throughout the runner. Since the density is not constant across the runner, see Figure 77, the fluid must accelerate as it passes the heat exchanger. This mechanism is desirable since the fluid is heated to the maximum possible temperature before leaving the heat exchanger.

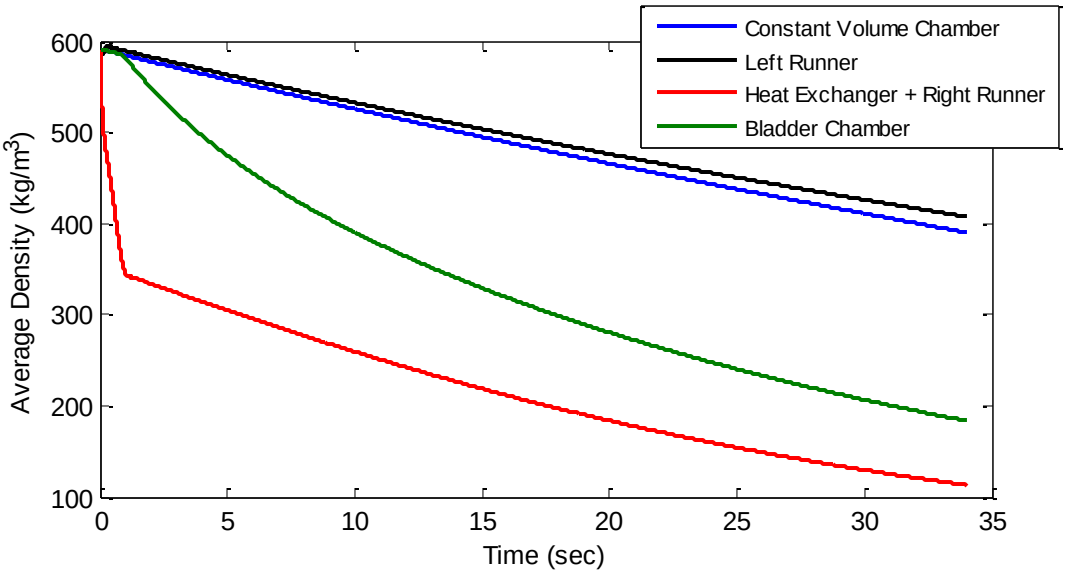

Figure 77: Average fluid density for various accumulator sections

The results we presented so far demonstrate that the heat exchanger is capable of heating the fluid to a desirable temperature. However, this mechanism does not appear to yield the expected improvement of maintaining higher pressures. An analysis of the overall accumulator behavior is required to understand this phenomenon.

In a standard accumulator, energy is obtained by expanding the fluid volume while fluid mass is maintained constant. This behavior leads to a decrease in density, which in turn, leads to a decrease in temperature (see Chapter I for more details). The combination of these effects causes the fluid pressure to drop based on the heat capacity of the gas. The thermally boosted accumulator is no different from a density point of view, since the fluid mass is constant and the volume expands in the same manner to obtain energy. The difference is that the pressure can be improved by injecting heat into the fluid in order to raise its temperature.

The high pressure nature of accumulators makes the task of heating the fluid a complex endeavor. Design of the thermally boosted accumulator presented in this section appears to effectively heat the right side of the system, but not its left side. This can be explained by the fact that no heat transfer mechanisms can transfer heat in the opposite direction of the fluid flow. In other words, convection only occurs from left to right, making conduction and radiation the only modes of heat transfer capable of transmitting heat from right to left. The conduction coefficients of fluids in the gaseous form are extremely low, making this mode of heat transfer insignificant. By comparison, the conductivity of metals is 10,000 times larger than the conductivity of gases (see Figure 51 for the argon gas values). Likewise, radiation heat transfer is only significant in the presence of considerable temperature difference. Furthermore, a straight line path with no obstruction between the hot and cold objects is usually required for radiation heat transfer to successfully occur. The thermally boosted accumulator is not designed to take advantage of this mechanism, and as a result, radiation heat transfer is considered to be a non-factor.

Under the assumption that heat is not transferred to the constant volume chamber, it is possible to analyze this part of the accumulator independently from the rest of the system. From the simulation results presented above, one can observe that the constant volume chamber behaves similarly to an isentropic accumulator. In the constant volume chamber, the density changes due to mass flow out of the chamber while maintaining the volume constant. The isentropic accumulator changes density due to the change in volume while maintaining

constant fluid mass. Even though the mechanisms are different in nature, the density effects are the same. Temperature is not a factor here, since these processes are assumed to be adiabatic (i.e. no heat transfer with the ambient).

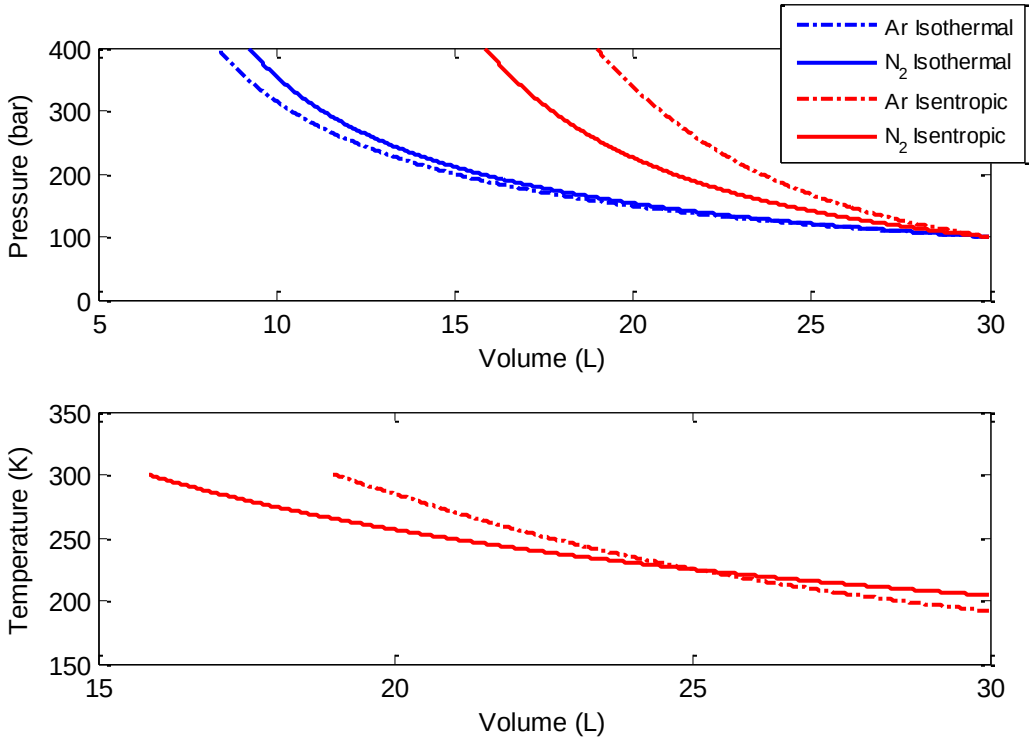

Figure 78: Ideal accumulator operation using nitrogen and argon gas as working fluids

Working Fluid	Isothermal (kJ)	Isentropic (kJ)
Argon	388.76	222.36
Nitrogen	375.91	271.91

Table 14: Energy storage capacity of nitrogen and argon during ideal operations

To understand the impact of isentropic operation, the equation of state is used to evaluate the pressure versus density relationship during this ideal operation. Figure 78 illustrates the behavior of an isentropic accumulator using argon as the working fluid. By integrating the area under the pressure versus volume curve, the accumulator energy storage is calculated for this ideal

operation. Table 14 shows that the energy storage of an argon isentropic accumulator is much lower than for another ideal operation, such as isothermal. Furthermore, the use of a different fluid, nitrogen gas, during isentropic operation can yield better energy storage results than the same condition for argon.

In the Selection of a Working Fluid section we demonstrate that argon is a better working fluid for a thermally boosted accumulator than nitrogen. This follows from the lower heat capacity of the argon gas resulting in less heat transfer required to maintain constant pressure. However, the lower heat capacity of the fluid has the opposite effect when heat transfer is not present. This behavior is further magnified by the nonlinear relationship between pressure and temperature. Based on this information, we conclude that the isentropic nature of the constant volume chamber severely impacts the operating conditions of the thermally boosted accumulator.

		Constant Volume Chamber	Hot Runner	Expanding Volume Chamber
Initial Mass	(kg)	6.493	0.278	1.027
Final Mass	(kg)	4.293	0.105	3.399
Initial Volume	(L)	11.004	0.471	1.027
Final Volume	(L)	11.004	0.471	18.524

Table 15: Mass and volume distribution of the thermally boosted accumulator

Table 15 further quantifies the impact of the isentropic operation for the constant volume chamber. From this table, one can observe that most of the gas resides initially in the constant volume chamber. Mass distribution within the system following the expansion demonstrates how well the thermally boosted accumulator has operated. This information shows that the isentropic operation

has a significant impact on the effectiveness of the system since the bladder chamber is 68% larger than the constant volume chamber while containing 21% less mass. The data below also shows that only 30.4% of the fluid mass interacts with the heat exchanger.

Accumulator Comparison

The last step remaining in our analysis is a performance comparison between a standard accumulator and a thermally boosted accumulator. Figure 79 illustrates the pressure versus volume curves for several accumulator operating conditions. The thermally boosted accumulator pressure results are based on the end pressure, while the temperature results are based on the “bulk” gas temperature. The results presented in Table 16 indicate the energy storage capacity for various operating conditions discussed in Chapter I. Most importantly, these results show that a 28.6% energy storage improvement is obtained by using a thermally boosted accumulator over a traditional accumulator.

In the previous sections, we discuss how the accumulator energy storage depends on heat transfer parameters and the discharging and charging power. This relationship with the output power is particularly important to the thermally boosted accumulator. This is the case since the heat transfer rate and power output have to be linearly proportional, defined in equation (6.2), to maintain constant pressure. The amount of heat required to maintain the accumulator at a constant pressure during a period of 34 seconds (discharging period of the

thermally boosted accumulator) is 851 kJ. Table 16 illustrates that only 45.8% of that heating value can be achieved.

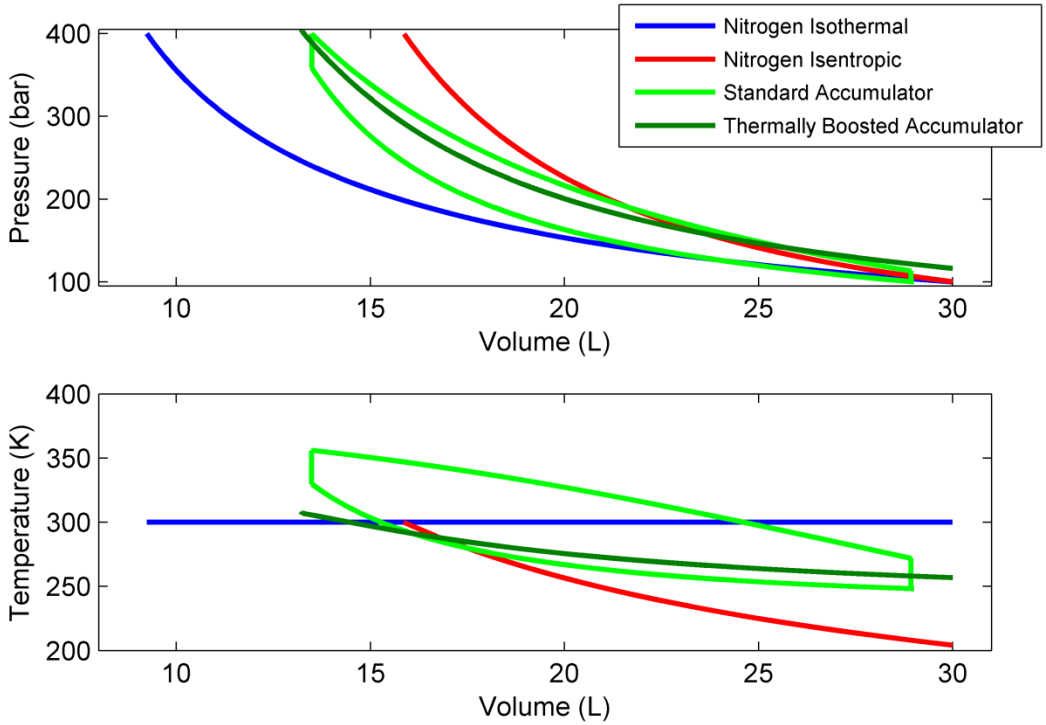

Figure 79: Thermally boosted accumulator comparison for output power of 10 kW

Ideal Nitrogen Accumulator		
Isothermal Energy Storage	375.9	(kJ)
Isentropic Energy Storage	271.9	(kJ)
Standard Nitrogen Accumulator		
Work In	331.9	(kJ)
Work Out	264.7	(kJ)
Efficiency	80	(%)
Thermally Boosted Accumulator		
Work Out	340.4	(kJ)
Heat In	389.5	(kJ)
Energy Storage Improvement	28.6	(%)

Table 16: Accumulator energy storage comparison for 10 kW output

Simulation Results at 60 kW Expansion

Next, we perform a simulation of the thermally boosted accumulator for a different power output of 60 kW. This operating condition increases the mass flow rate from the constant volume chamber to the bladder chamber, causing the velocity to increase in the hot runner (see Figure 80). However, the heat transfer coefficient of the metal foam heat exchanger does not change drastically with the increase in Reynolds number (which is affected by the increase in speed). This behavior is illustrated in Figure 66, which is a function of the metal foam parameters (i.e. porosity, pores per inch, radius, and metal type). For this reason, the heat exchanger length is doubled to ensure that the fluid output temperature is close to that of the heat source.

The mechanisms of the thermally boosted accumulator do not change with an increase in power output. Results in Table 17 show that the thermally boosted accumulator energy storage remains practically the same. This behavior is achieved due to the effectiveness of the heat exchanger and the lack of heat transfer with the outside ambient. In contrast, the standard accumulator is penalized by its interaction with the environment, which is a function of power output. This behavior of the standard accumulator leads to poor performance, as illustrated in Table 17 and Figure 81. As a result, the energy storage improvement of the thermally boosted accumulator is 40.3% over the traditional accumulator.

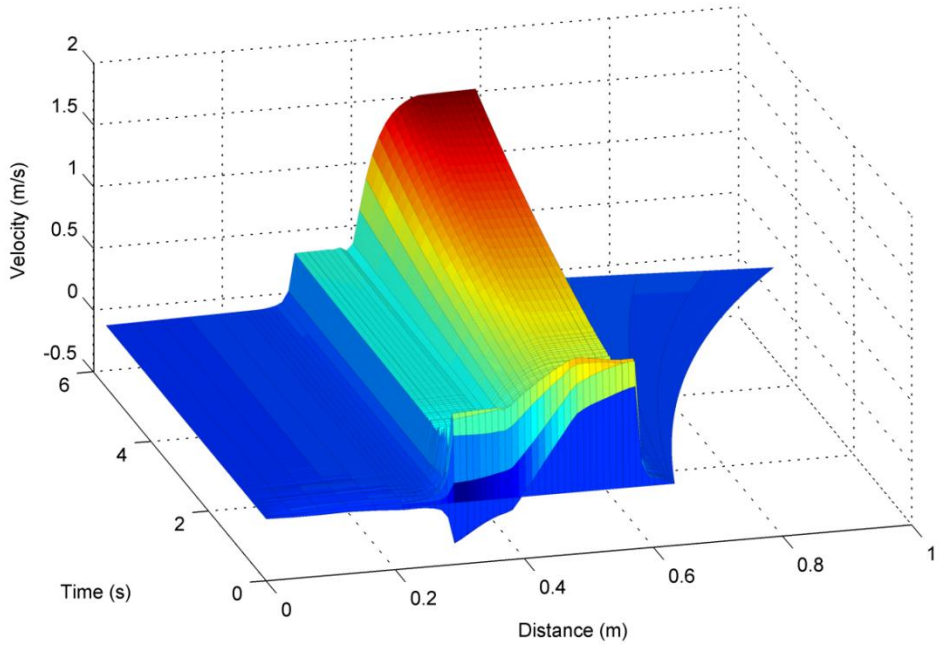

Figure 80: Accumulator velocity profile with an output power of 60 kW

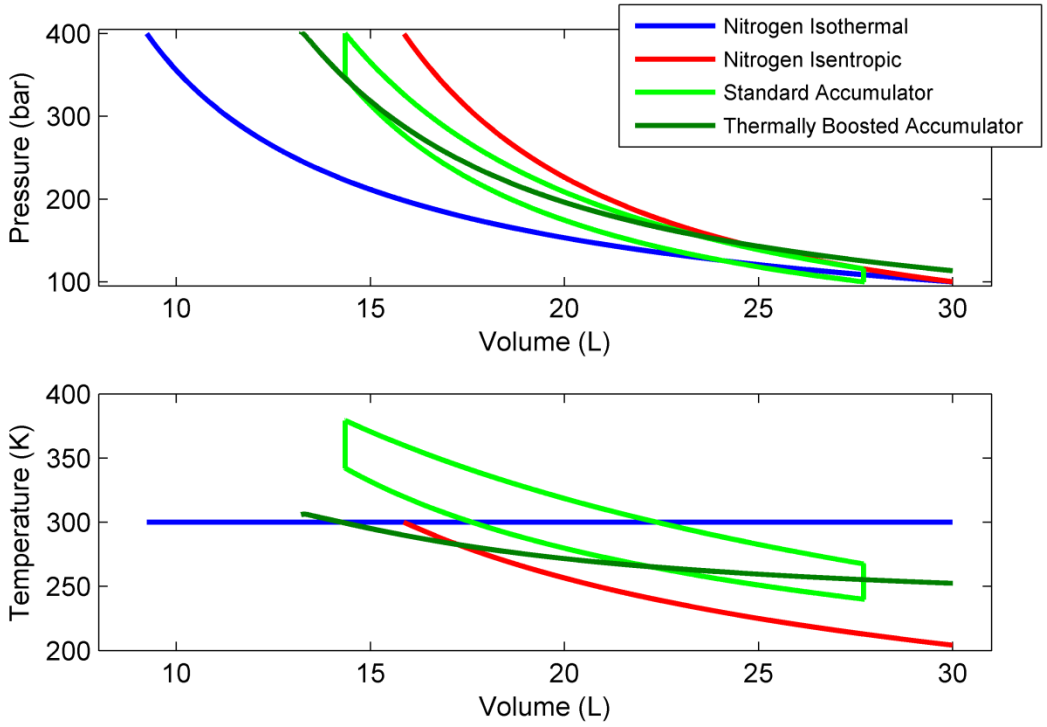

Figure 81: Thermally boosted accumulator comparison for output power of 60 kW

Ideal Nitrogen Accumulator		
Isothermal Energy Storage	375.9	(kJ)
Isentropic Energy Storage	271.9	(kJ)
Standard Nitrogen Accumulator		
Work In	281.7	(kJ)
Work Out	238.3	(kJ)
Efficiency	85	(%)
Thermally Boosted Accumulator		
Work Out	334.4	(kJ)
Heat In	373.3	(kJ)
Energy Storage Improvement	40.3	(%)

Table 17: Accumulator energy storage comparison for 60 kW output

Throttling Operation

The thermally boosted accumulator results above indicate that energy storage capacity can be improved by increasing the amount of mass that interacts with the heat exchanger. Indeed, Table 15 illustrates that only 30% of the total fluid mass passes through the heat exchanger. To improve this effect, the control valves shown in Figure 64 can be used to “throttle” the fluid entering the hot heat exchanger runner to create a disturbance in the fluid flow. Restricting the flow creates pressure waves that propagate back towards the constant volume chamber resulting in high mass flow rates in and out of the heat exchanger. To validate this theory, we use the thermally boosted accumulator model to simulate the right control valve of the hot runner being opened and closed every 50 milliseconds (10 Hz operating frequency).

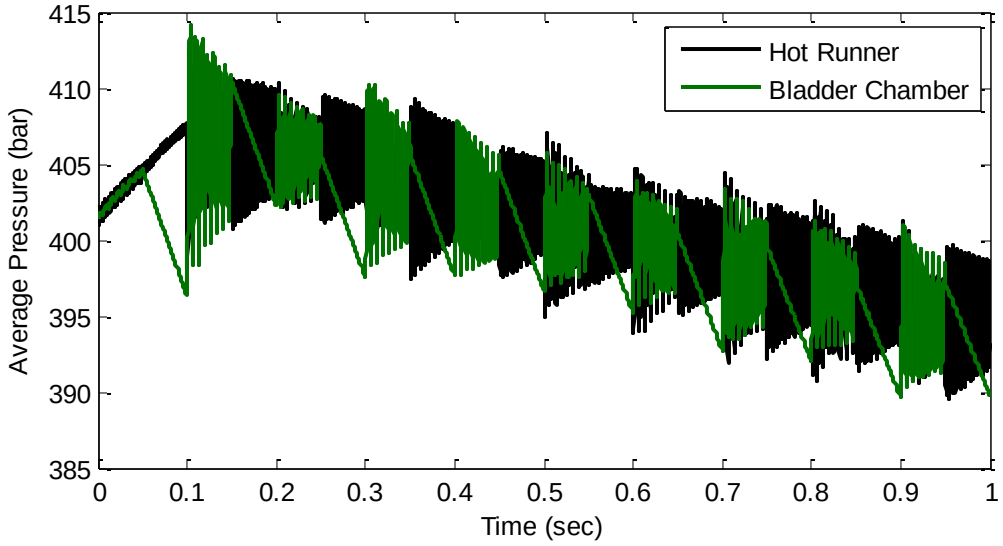

Figure 82: Average pressure for thermally boosted accumulator sections

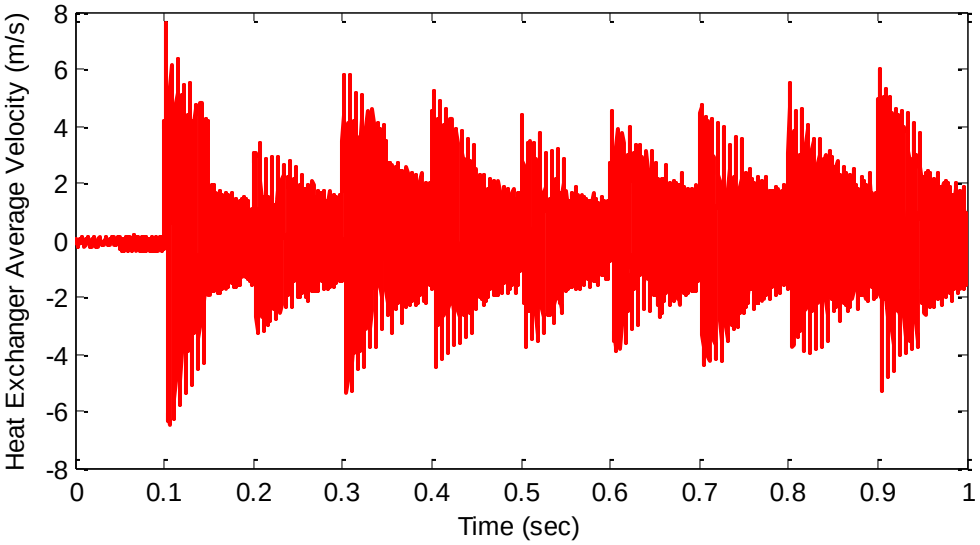

Figure 83: Heat exchanger fluid average velocity

From performing the throttling simulation of a thermally boosted accumulator, we obtain the pressure history for various sections of the accumulator. Figure 82 illustrates that when the throttle is open the hot runner and bladder chamber have nearly the same pressure. When the throttle is closed, the expanding volume chamber pressure drops as no additional mass can enter the chamber to compensate for the volume expansion. Similarly,

pressure fluctuations occur in the hot runner due to the momentum of the fluid moving towards the closed throttle. These pressure fluctuations induce high velocity flows shown in Figure 83. By comparing these velocity values to that of Figure 76, it can be observed that throttling the accumulator increases the speed magnitude by at least ten times.

At a first glance, throttling the thermally boosted accumulator appears to provide the desired fluid mass movement between both sides of the heat exchanger. However, Figure 84 illustrates that even though oscillations are present, the end pressure still drops similarly to the previous thermally boosted accumulator results. Indeed, Table 18 gives nearly the same energy storage capacity and heat intake quantity as the unthrottled thermally boosted accumulator.

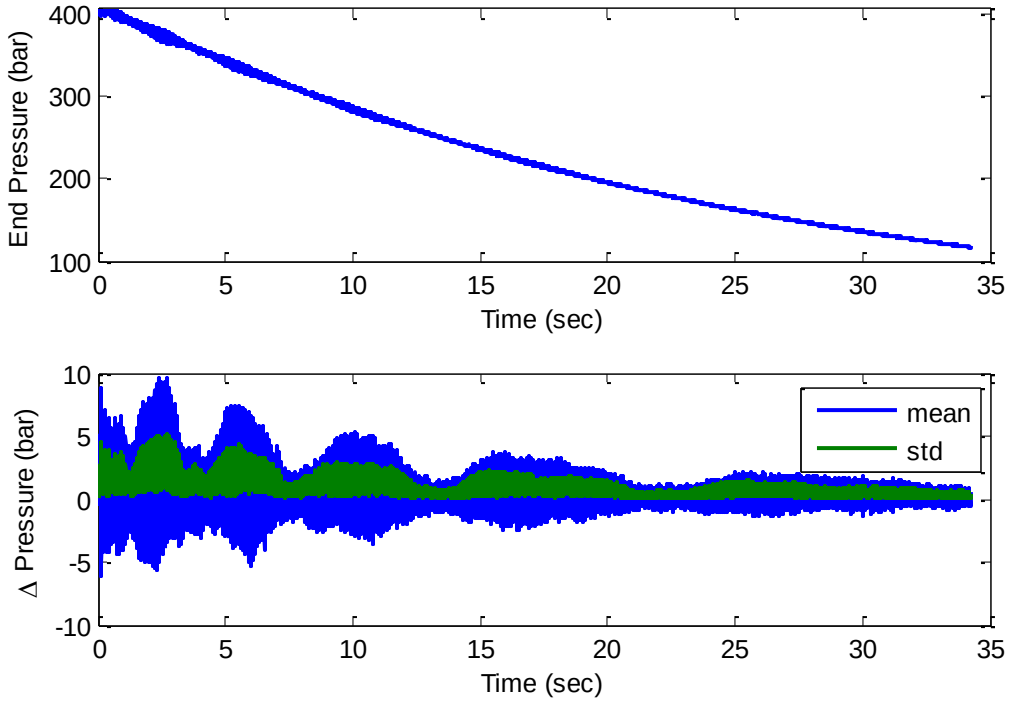

Figure 84: (a) Accumulator end pressure for throttling accumulator (b) mean and standard deviation of change in pressure from end pressure

Thermally Boosted Accumulator		
Work Out	342.4	(kJ)
Heat In	394.0	(kJ)

Table 18: Throttling thermally boosted accumulator energy storage capacity at 10 Kw

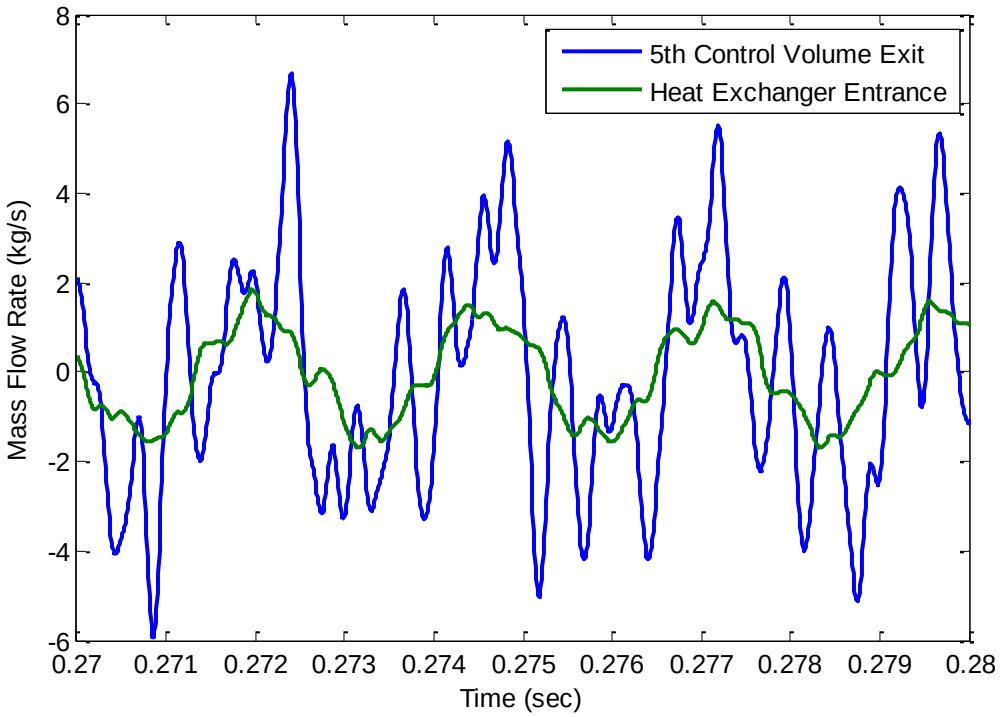

Figure 85: Mass flow rate of selected control volumes entrance and exit

The thermally boosted accumulator mass flow rate information is used to understand how pressure waves impact the exchange of mass between the control volumes. Figure 85 illustrates the mass flow rate at the boundaries of the two control volumes. The first set of data is obtained at the right edge of the fifth control volume in the constant volume chamber (see Figure 65). This location was chosen to understand the mass flow rate mechanism in a large volume section. The second curve demonstrates the mass flow rate at the inlet of the heat exchanger over time. This data has a sinusoidal form that oscillates at approximately 370 Hz frequency. It can be concluded that the acoustic behavior

causes the mass flow rate to switch directions rapidly, and as a result, a small amount of mass appears to be constantly leaving from and returning to the control volumes.

In conclusion, throttling the thermally boosted accumulator to induce wave action and more flow rates through the system does not provide significant benefits to the system, due to the high frequency nature of the acoustic waves. However, it should be noted that if another less efficient heat exchanger was used in the thermally boosted accumulator, the heat transfer could be improved with the throttling behavior. In addition, further improvement could be achieved by accelerating the dissipation of the acoustic waves near the end of the constant volume chamber. This behavior would essentially convert the kinetic energy of the fluid into thermal energy.

Thermally Boosted Accumulator with High Heat Capacity Insert

In the previous section, we suggest a method for improving the heat transfer between the heat exchanger and the constant volume chamber with the use of a throttle. In this section, other methods to improve upon the isentropic nature of the constant volume chamber are presented. One such method is the use of other materials in the constant volume chamber to increase the heat capacity of the system. In the Literature Review chapter, we discuss how elastomeric foam can be used to accomplish this exact goal. However, Figure 87 demonstrates that better volumetric heat capacity can be obtained by using metals and alloys instead of elastomers. To accomplish this goal, we propose to

use an aluminum alloy, T7451, as the metal foam material. Figure 86 shows the metal foam insert in the constant volume chamber of the thermally boosted accumulator.

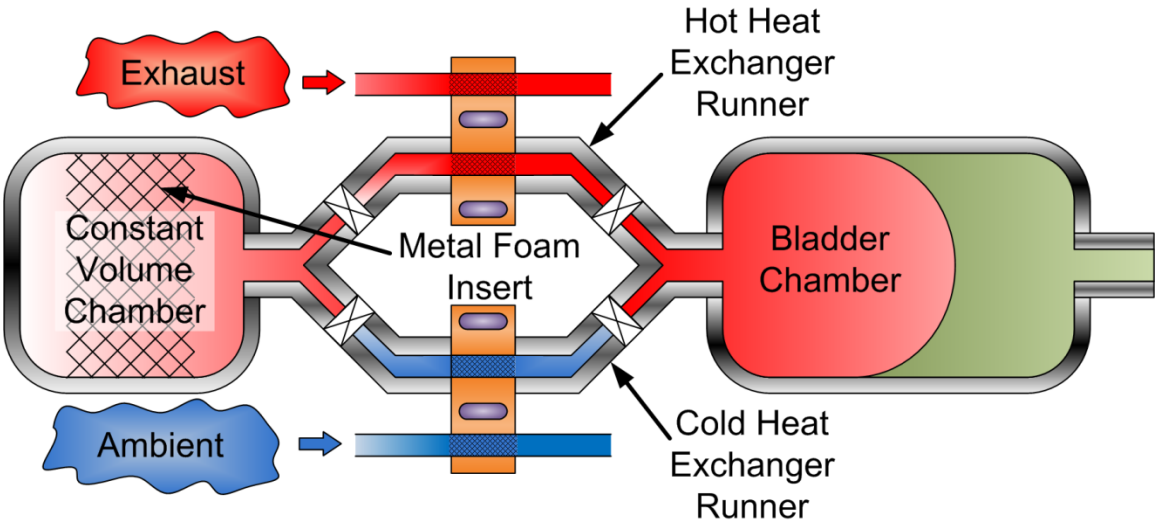

Figure 86: Thermally boosted accumulator concept with metal foam insert

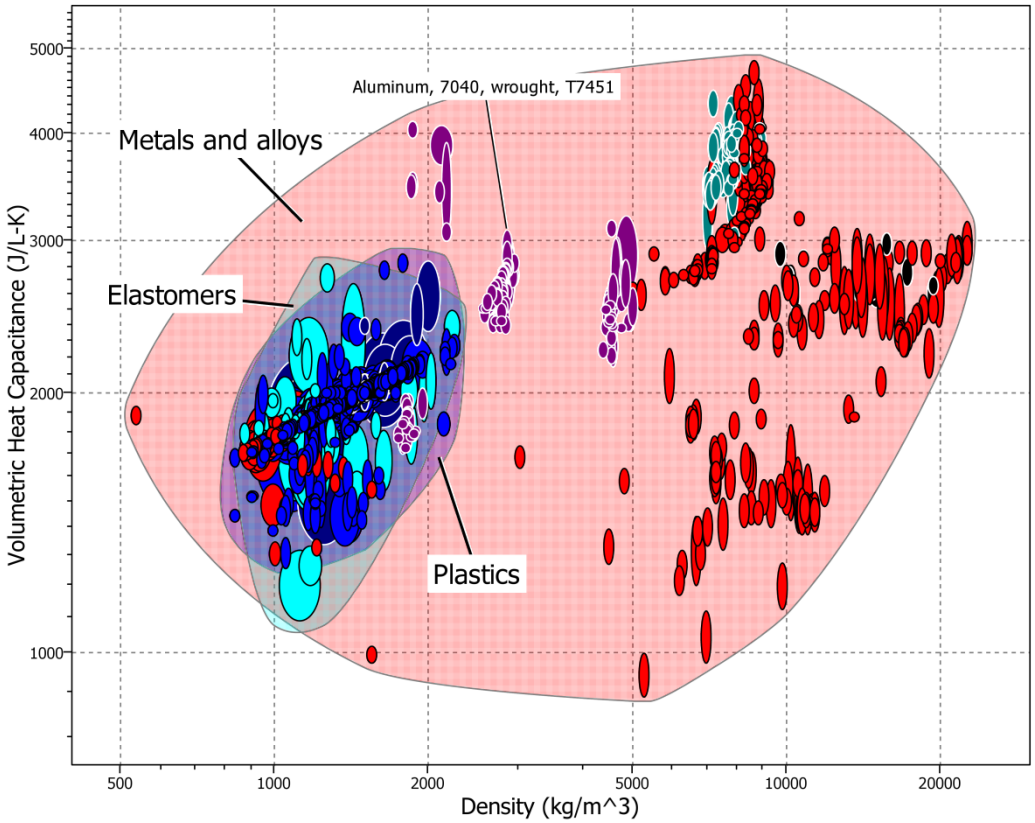

Figure 87: Materials volumetric heat capacitance versus density [52]

The heat exchanger model section outlines the convective heat transfer coefficient behavior as a function of pipe radius and Reynolds number for a given set of metal foam parameters. Figure 61 shows that that the convection coefficient decreases as the pipe radius increases, while the Reynolds number has diminishing impact. This comes from the fact that the radial heat transfer mechanism becomes more dominant than the convection of the fluid in the axial direction.

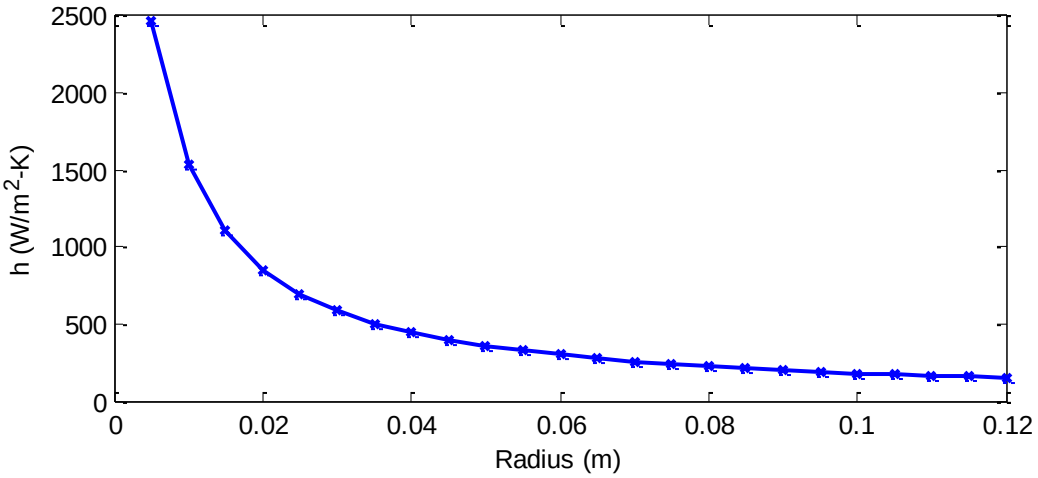

Figure 88: Convective heat transfer coefficient as a function of pipe radius

Aluminum T7451 Foam Properties		
Porosity	0.9	(-)
Pores per inch	30	(ppi)
Volume	5	(L)
Mass	1.42	(kg)
Diameter	0.230	(m)
Surface area	19.43	(m^2)
Density	2845	(kg/m^3)
Convective coefficient	157.5	(W/m^2-K)
Metal conductivity	164	(W/m-K)
Specific heat capacity	1040	(J/kg-K)

Table 19: Aluminum alloy metal foam properties

Simulation Results at 10 kW Expansion

We select the metal foam volume based on the available space in the constant volume chamber. Table 19 outlines the properties of the metal foam we use for the thermally boosted accumulator simulation. It should be noted that the volume of the metal (in this case 0.5 L) reduces the amount of gas volume, which in turn causes a decrease in the energy storage. This effect is accounted for in our results below.

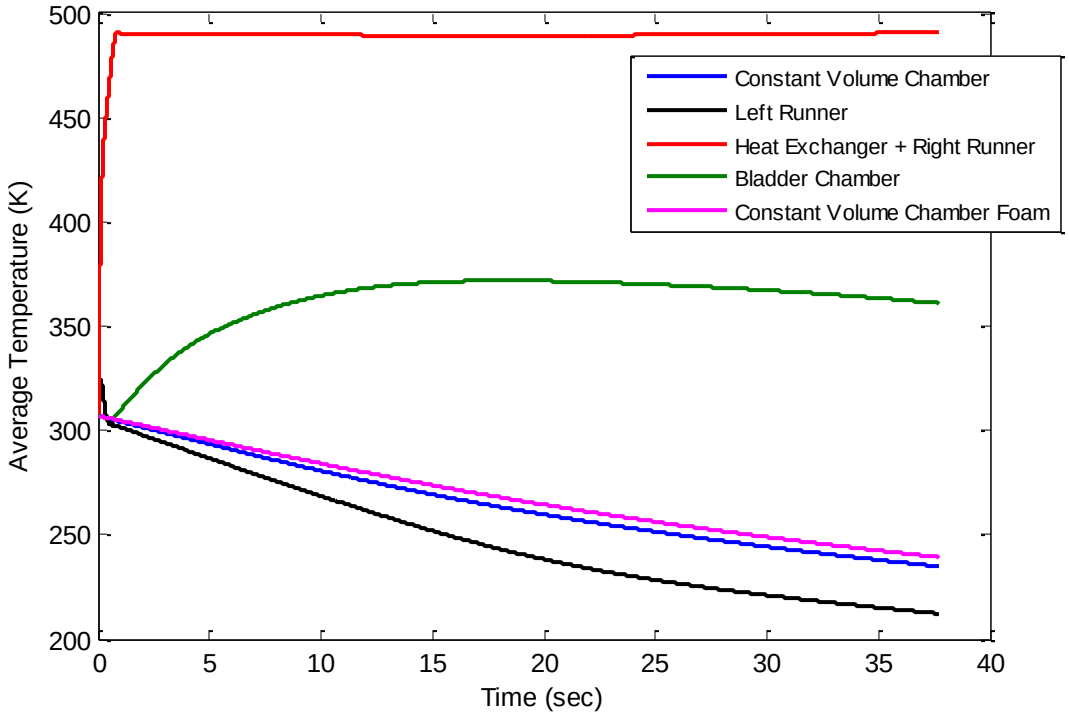

Figure 89: Average temperature distribution for a thermally boosted accumulator with foam insert

By inserting the metal foam in the constant volume chamber, the gas temperature can be increased from 200 K to about 240 K, as shown in Figure 89. This improved temperature behavior is a result of the increased heat capacity of the system in the presence of the metal foam, which improves the pressure drop rate and allows more fluid to pass through the heat exchanger. In comparison,

44.6% of the fluid mass now interacts with the heat exchanger as opposed to 30% from the previous thermally boosted accumulator design. Table 20 demonstrates how input heat and work out have increased with the addition of the aluminum metal foam. It is interesting to note that this system is capable of slightly higher energy storage than an isothermal nitrogen accumulator (see Table 14), but it is still less than the isothermal argon accumulator. The pressure versus volume curve for this thermally boosted accumulator can be seen in Figure 90, along with the accumulator cycles.

Thermally Boosted Accumulator		
Work Out	377.4	(kJ)
Heat In	431.3	(kJ)
Metal Foam Heat In	98.7	(kJ)
Energy Storage Improvement	42.6	(%)
Effected Fluid Mass by Heat Exchanger	44.6	(%)

Table 20: Thermally boosted accumulator energy storage capacity with aluminum alloy foam insert at 10 Kw expansion

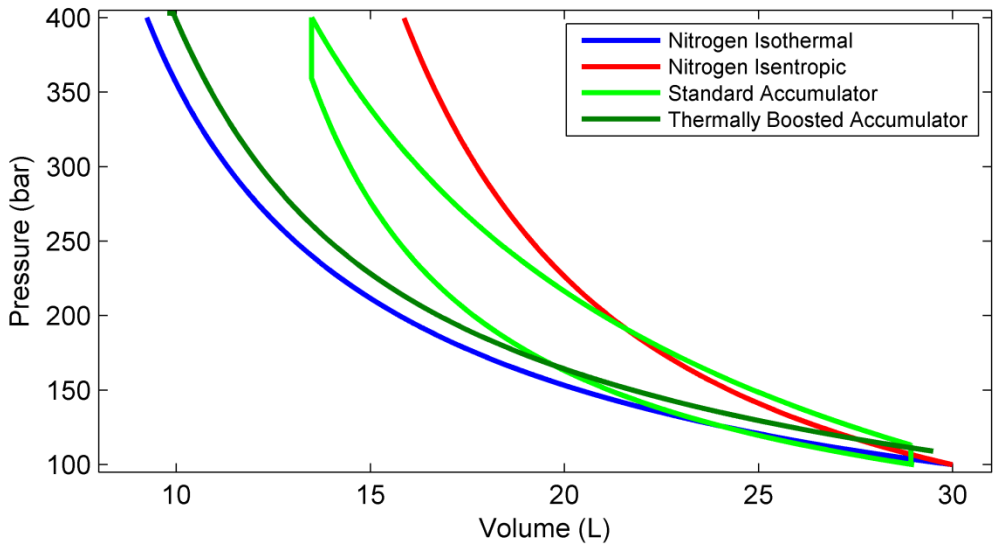

Figure 90: Thermally boosted accumulator with metal foam insert pressure comparison

Accumulator Shell Heat Sink

Adding the aluminum metal foam is an effective way to increase the heat capacity of the accumulator, however the additional metal volume displaces the gas volume, thus reducing the overall energy storage capacity. To resolve this issue, we proposed to use the metal accumulator shell as a heat sink for our system. This approach can significantly increase the heat capacity of the system due to the significant thickness of the accumulator shell required to safely contain the gas at high pressures.

$$\frac{r_o}{r_i} = \sqrt{1 + \frac{p}{\sigma_a}} \tag{2.7}$$

Heat Capacity Parameter Values		
Steel Alloy Fatigue Strength	400	(MPa)
Maximum Operating Pressure	50	(MPa)
Inner Radius	0.155	(m)
Outer Radius	0.122	(m)
Inner Volume	7.87	(L)
Steel Volume	1.43	(L)
Steel Density	7.85	(kg/L)
Steel Mass	11.19	(kg)
Steel Heat Capacity	450	(J/kg-K)

Table 21: Constant volume chamber geometrical and steel parameters

To calculate the accumulator metal mass, a maximum stress and maximum operating pressure values must be obtained. Table 21 shows the values selected with the fatigue strength value being used as a conservative estimate of the maximum stress value. Equation (2.7) is then used to calculate the outer to inner radius ratio. From the previous sections, we know the inner

radius of an accumulator, and the outer radius can be easily calculated. The spherical and cylindrical volume equations are used to calculate the total volume of the constant volume chamber (including the shell volume). This volume is then subtracted from the inner gas and aluminum foam volumes to obtain the steel volume. The steel density multiplied by the volume leads to the total steel mass.

In this thermally boosted accumulator implementation the heat capacity of the aluminum foam is 3.4 times smaller than the heat capacity of the steel shell. However, the metal foam greatly facilitates the heat transfer between the gas and the metal shell. We combine these features and use a lump capacity model to predict the performance of the new thermally boosted accumulator.

Simulation Results at 10 kW Expansion

The thermally boosted accumulator simulation with lump capacity demonstrates that the fluid temperatures in the constant volume chamber are significantly higher than previous results. Figure 91 illustrates the average fluid temperature in the constant volume chamber to be around 375 K after the total expansion at a constant rate of 10 kW. In contrast, the thermally boosted accumulator average fluid temperature for the same region without the added heat capacity is 200 K. In addition, the figure below demonstrates a significant difference between the constant volume chamber and the metal foam. This occurs because the metal foam in the constant volume chamber only affects part of the available volume. The volume without the metal foam is not influenced by heat transfer, and therefore, suffers a significant temperature drop. This behavior

is verified with the low average fluid temperatures on the hot runner to the left of the heat exchanger (labeled left runner in Figure 91).

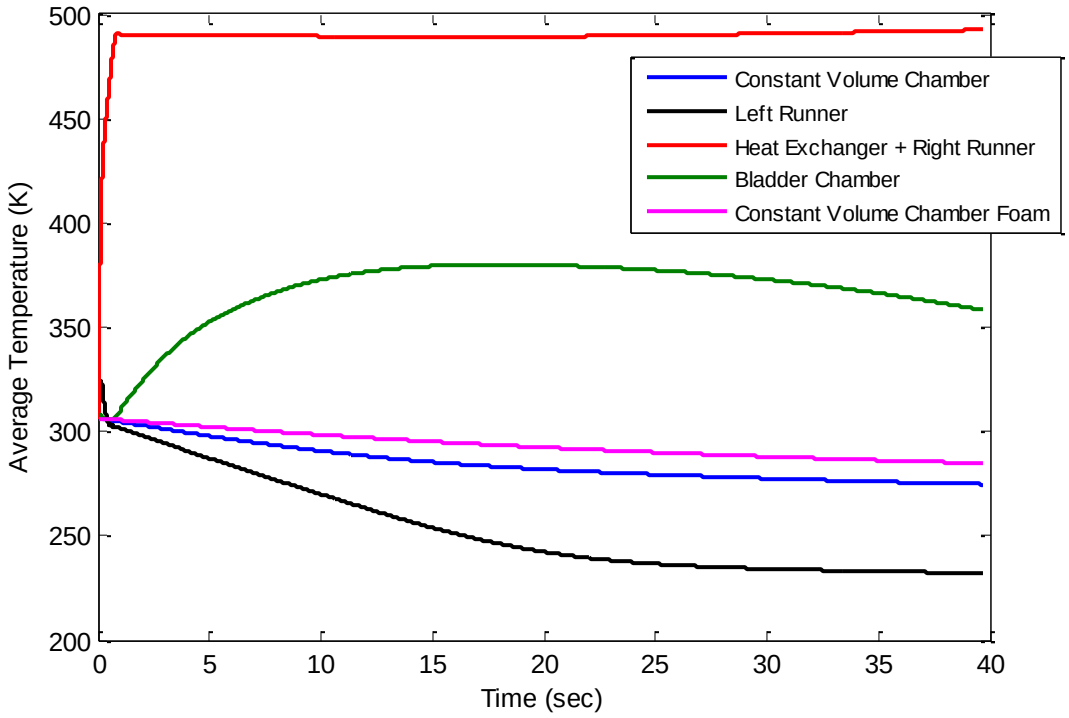

Figure 91: Average temperature distribution of thermally boosted accumulator with lump heat capacity (steel shell + aluminum foam)

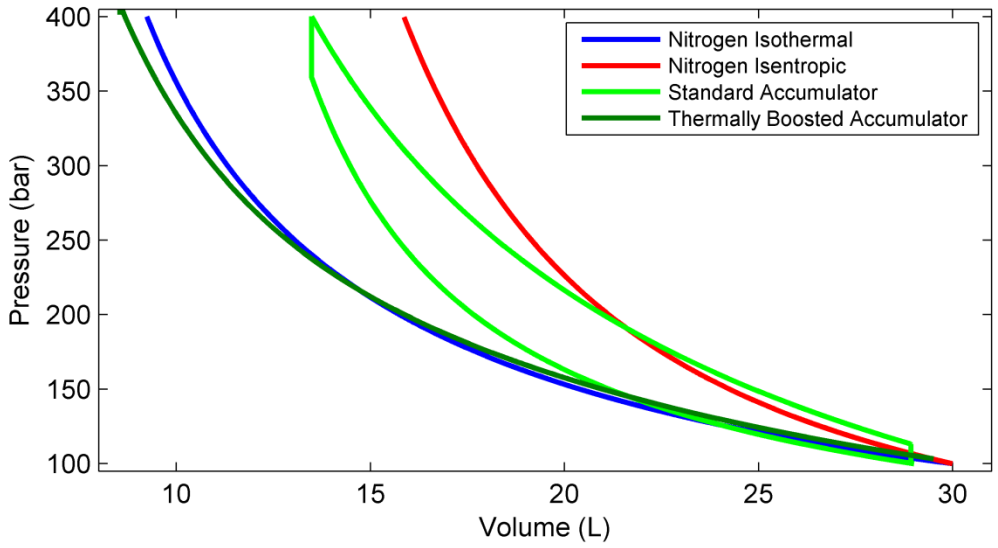

Figure 92: Thermally boosted accumulator heat capacity

The pressures versus volume curves suggest that the thermally boosted accumulator is operating isothermally, as seen in Figure 92. With the additional heat capacity, the accumulator energy storage value increases, leading to a 39% improvement over the standard accumulator. From Figure 93 we can conclude that the accumulator has reached close to the maximum energy storage. This is the case since the addition of heat will only cause the accumulator to operate over a higher temperature isothermal line.

Thermally Boosted Accumulator Expansion at 10 kW		
Work Out	397.3	(kJ)
Heat In	437.0	(kJ)
Lump Capacity Heat In	137.6	(kJ)
Energy Storage Improvement	39.2	(%)
Effected Fluid Mass by Heat Exchanger	53.5	(%)

Table 22: Thermally boosted accumulator energy storage capacity with lump heat capacity

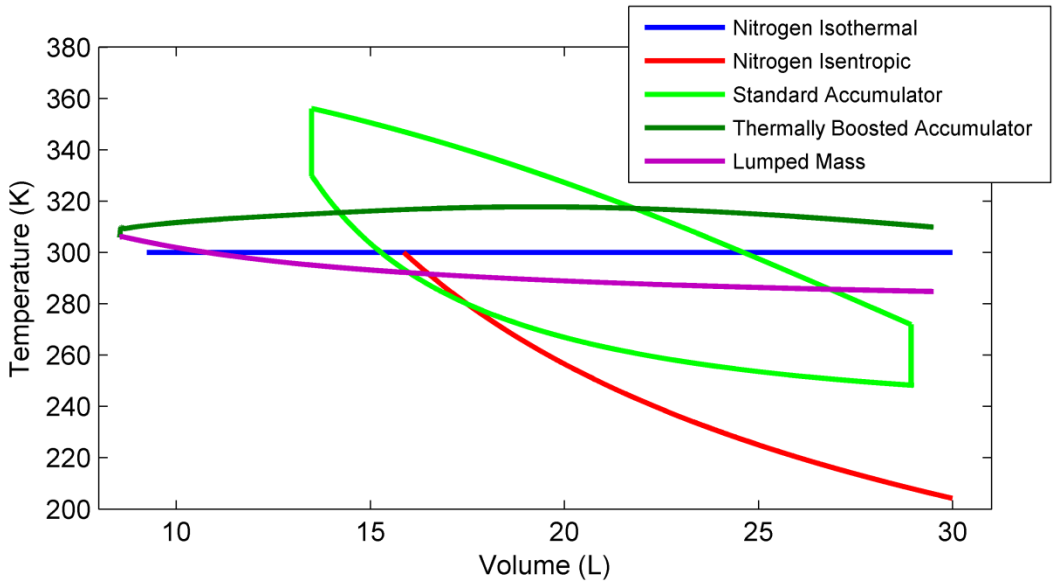

Figure 93: Accumulator bulk temperature comparison

Simulation Results at 10 kW Compression

All of the results shown so far correspond to the analysis of the thermally boosted accumulator during expansion. However, in order to evaluate the complete impact of the system, the compression phase must be also taken into consideration. We simulate the accumulator during the compression and present our results in Table 23, Figure 94, and Figure 95.

Thermally Boosted Accumulator Compression at 10 kW		
Work In	399.5	(kJ)
Heat Out	341.0	(kJ)
Lump Capacity Heat Out	182.6	(kJ)
Effected Fluid Mass by Heat Exchanger	48.3	(%)

Table 23: Thermally boosted accumulator energy storage capacity with lump heat capacity

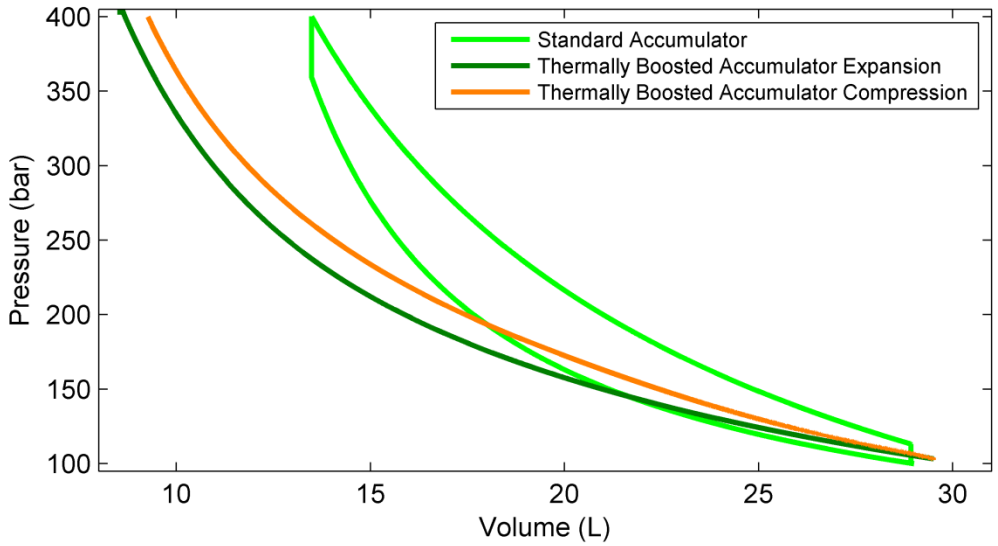

Figure 94: Thermally boosted accumulator expansion and compression pressure comparison

When comparing the compression results to the expansion data above, some interesting behavior is observed. At first sight, the compression results appear to imply that the thermally boosted accumulator has some inefficiency

due to the higher compression work into the system versus the work out during the expansion process (see Table 22). An analysis of the total heat transfer of the system paints a different picture. Indeed, only 91% of the total heat in the system is removed from the accumulator. This causes the bulk temperature of the accumulator to be higher than during expansion, as can be observed on Figure 95. It is this effect that causes the gas to compress along a different pressure curve and result in higher work values.

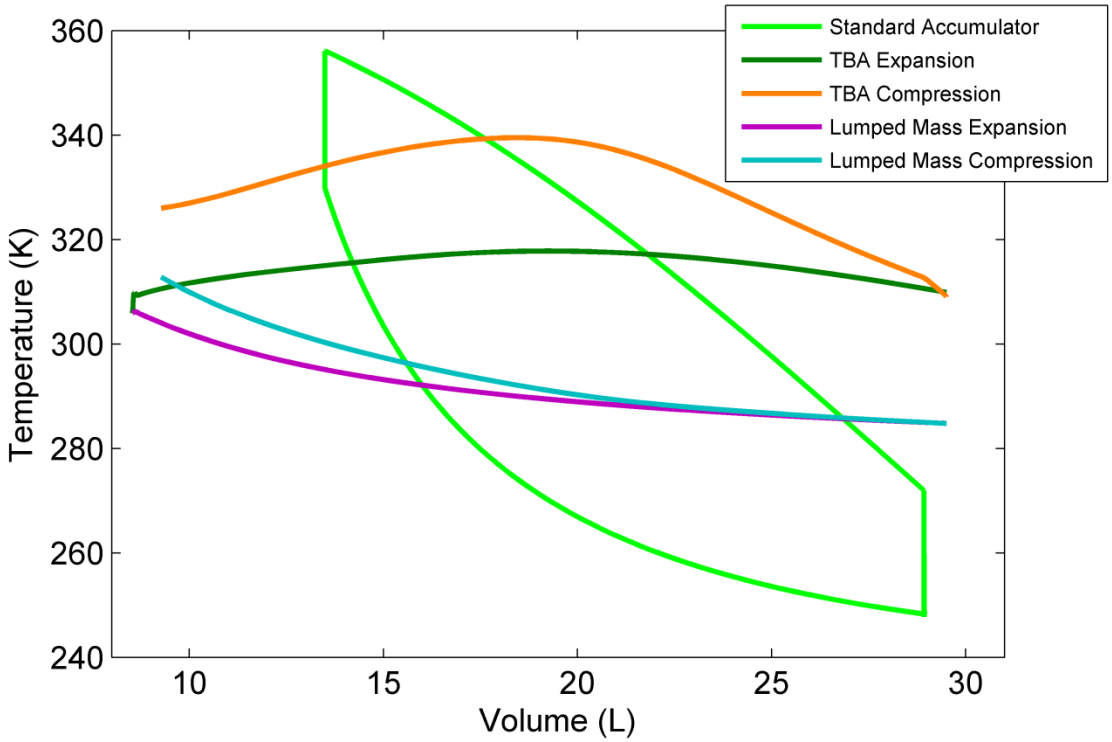

Figure 95: Thermally boosted accumulator expansion and compression bulk temperatures comparison

Simulation Results at 60 kW Expansion and Compression

From previous analysis we conclude that the power demand has a significant impact on the accumulator energy storage. To understand the consequences of high power demands for the new thermally boosted

accumulator design, a new simulation is performed with a constant 60 kW power demand. The results of this simulation (see Table 24) show that the thermally boosted accumulator is effective at storing energy as the work out during the expansion is 99.5% of the work value obtained during the 10 kW operation (see Table 22). Furthermore, the energy storage improvement of 61% can be expected when comparing a thermally boosted accumulator versus a normal accumulator operating at 60 kW. Figure 96 and Figure 97 further illustrate that the thermally boosted accumulator performance is almost independent of the power demand requested.

Standard Nitrogen Accumulator at 60 kW		
Work In	281.7	(kJ)
Work Out	238.3	(kJ)
Efficiency	85	(%)
TBA Expansion at 60kW		
Work Out	385.2	(kJ)
Hot Heat Exchanger Heat In	410.4	(kJ)
Lump Mass Heat In	138.2	(kJ)
Effected Fluid Mass by Heat Exchanger	54.26	(%)
Energy Storage Improvement	61.6	(%)
TBA Compression at 60kW		
Work In	387.7	(kJ)
Cold Heat Exchanger Heat Out	289.9	(kJ)
Lump Mass Heat Out	186.7	(kJ)
Effected Fluid Mass by Heat Exchanger	46.5	(%)

Table 24: Thermally boosted accumulator energy storage capacity with lump heat capacity

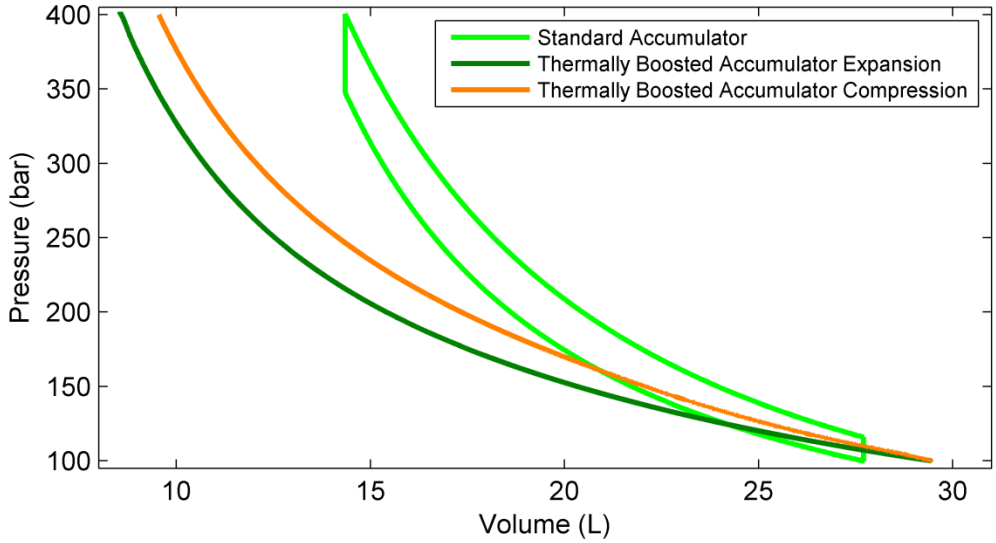

Figure 96: Thermally boosted accumulator expansion and compression pressure comparison

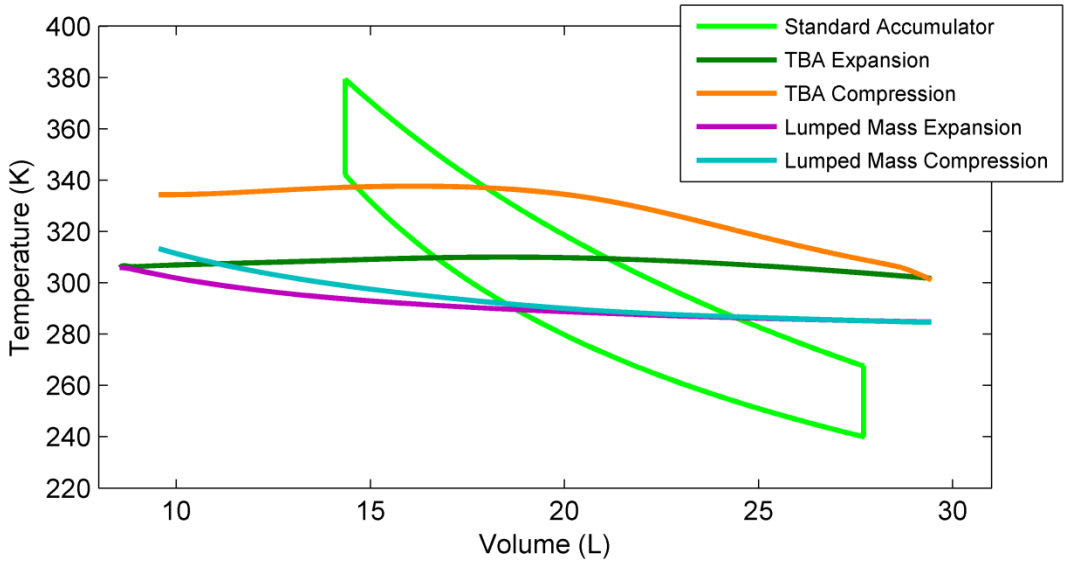

Figure 97: Thermally boosted accumulator expansion and compression bulk temperatures comparison

Fluid Heat Transfer Considerations

In the analysis above, heat is only transferred in and out of the fluid via a metal foam heat exchanger. However, other modes of heat transfer may exist that could affect the thermally boosted accumulator performance. To investigate the potential for unaccounted heat transfer effects, we use the data presented in

Figure 98. The detailed discussion of the heat transfer behavior for all illustrated components from left to right follows.

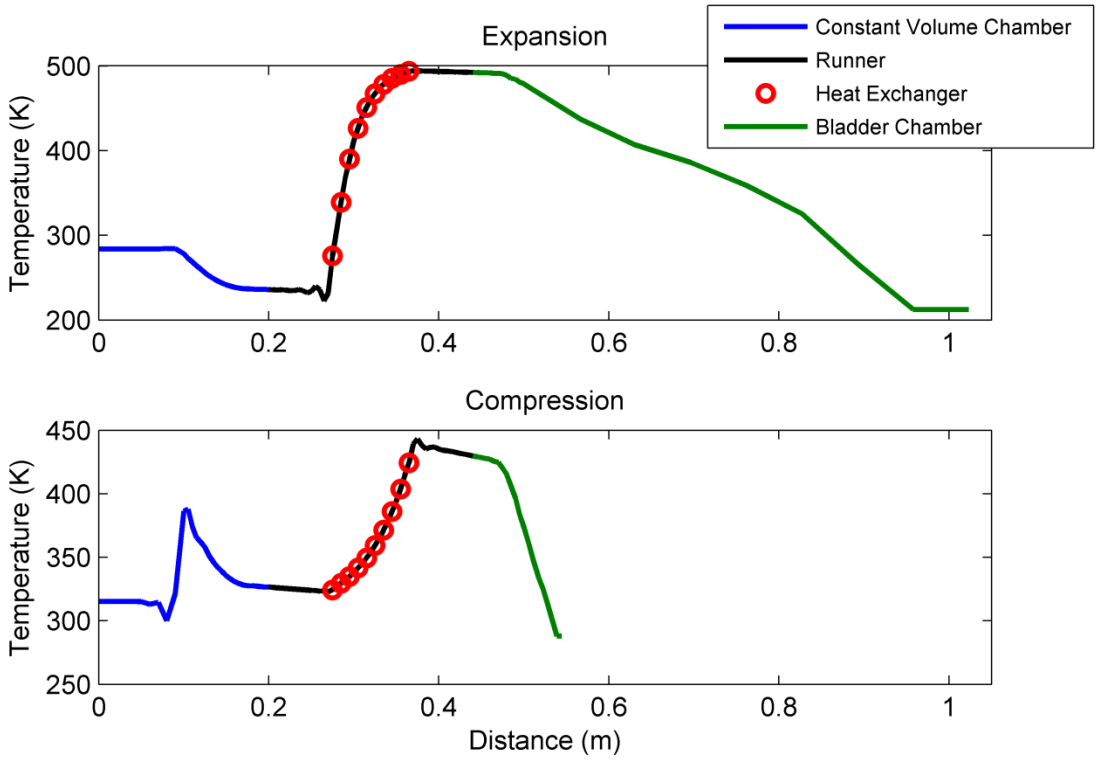

Figure 98: Temperature distribution across accumulator at the end of expansion and compression

Constant Volume Chamber Natural Convection to Ambient

In the constant volume chamber, the metal foam heat transfer is calculated based on the sophisticated 2D heat transfer models discussed previously. This model captures the heat flows in and out of the fluid to the metal shell of the accumulator. However, the interaction between the accumulator shell and ambient is not considered. To address this problem, equation (6.3) was developed by Morgan [**53**] in order to calculate the natural convection around a horizontal isothermal cylinder. From Figure 98 we estimate the metal surface temperature to be plus or minus 20 K from an ambient temperature of 300 K. Using the equations below, the convection coefficient is estimated to be 4 W/m^2-

K. This coefficient demonstrates that heat transfer out of the accumulator shell is insignificant and can be neglected during the simulation.

$$\overline{Nu}_D = \frac{\bar{h} \cdot D}{k} = C \cdot Ra_D^n \tag{6.3}$$

$$Ra_D = \frac{g\beta(T_s - T_\infty)D^3}{v\alpha} \tag{6.4}$$

$$C = 0.125 \qquad n = 0.333 \quad for\ 10^7 \leq Ra_D \leq 10^{12} \tag{6.5}$$

Ideal Air Constants @ 300 K		
Kinematic Viscosity, ν	15.89e-6	(m^2/s)
Thermal Diffusivity, α	22.5e-6	(m^2/s)
Thermal Conductivity, k	12.6e-3	(W/m-K)
Expansion Coefficient, β	$1/T_S$	(1/K)

Table 25: Air properties for natural convection

Constant Volume Chamber Axial Natural Convection

The next heat transfer behavior to be investigated is the effect of temperature difference in the constant volume chamber. In Figure 98, a large temperature difference occurs after the metal foam and before the runner, which can lead to mixing of the gas due to the density difference at this region. Chapter I describes how the heat transfer in a normal accumulator occurs due to this density difference effect. However, the natural convection in standard accumulators occurs in the radial direction, while this particular scenario occurs in the axial direction.

$$\overline{Nu}_L = \frac{\bar{h} \cdot L}{k} = 0.22\left(\frac{Pr}{0.2 + Pr} Ra_L\right)^{0.28} \left(\frac{H}{L}\right)^{-\frac{1}{4}} \tag{6.6}$$

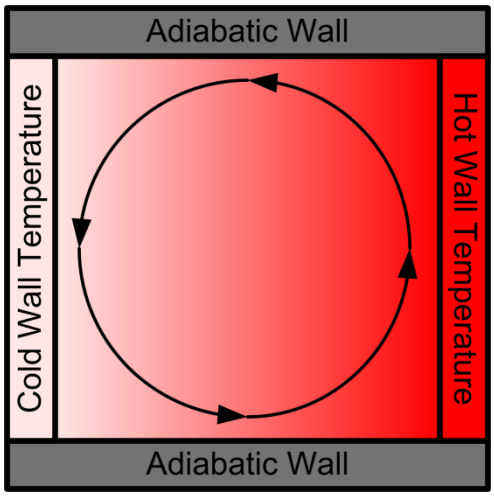

Figure 99: Idealized natural convection across a fluid with

A heat transfer correlation was first suggested by Catton [**54**], see equation (6.6), in order to calculate the axial heat transfer across a fluid separated by two walls with different temperatures. Figure 99 gives a visual representation of this phenomenon. In the context of the thermally boosted accumulator, equation (6.6) is used to obtain a crude heat transfer estimation between the two control volumes. The large temperature difference region of the compression test results of Figure 98, in the constant volume chamber, are used to calculate the heat transfer parameters, shown in Table 26.

Argon Constants @ 350 K		
Kinematic Viscosity, ν	7.75e-8	(m^2/s)
Thermal Diffusivity, α	1.00e-7	(m^2/s)
Thermal Conductivity, k	38.3e-3	(W/m-K)
Expansion Coefficient	1/350	(1/K)
Prandtl Number	0.775	(-)

Table 26: Argon properties for natural convection

The Rayleigh number is calculated based on equation (6.4) with the distance between the desired control volumes, “L”, replacing the diameter value

“D”. In addition, the temperature difference across the control volume is required to calculate the Rayleigh number. Based on the compression results presented in Figure 98, we use a value of 86 K. With the Rayleigh number now acquired, the Nusselt number must be obtained. For this purpose, we use a height over distance (“H/L”) value of 10, which is approximately equal to the diameter over distance value.

All parameters are now obtained, and the convection coefficient is estimated to be 95.5 W/m^2-K. This estimate is significantly high and suggests that axial heat transfer due to mixing can impact the temperature distribution across the control volumes. Furthermore, the likelihood of mixing increases when radial effects, discussed in chapter I , are coupled with the axial mechanism.

In the constant volume chamber, mixing only improves the thermally boosted accumulator operation by increasing the amount of gas exposed to the metal foam heat sink. This behavior leads to the favorable operating conditions, which maintain a uniform temperature distribution. However, mixing will most likely not yield significant improvement towards the energy storage capacity of the accumulator due to the small amount of gas currently unaffected by the heat sink.

Fluid Runner Heat Transfer

In Figure 98, we observe that the temperatures in the hot and cold runners are always higher and lower than 300 K, respectively. This implies that some form of heat transfer occurs between the fluid and the pipe, especially since the mass flow rate can be significantly high. However, this process only occurs

temporally as the low heat capacity of the pipe (due to its small mass) causes it to be quickly heated and cooled to match the temperature of the fluid. Heat transfer from the pipe to the ambient occurs via natural convection. From equation (6.3) it can be concluded that this effect is relatively small and can be considered to be an adiabatic process. Given the conclusions above, no considerations are needed to accurately predict the heat transfer between the fluid and runners.

Bladder Chamber Heat Transfer

Heat transfer effects in the bladder chamber are similar to those discussed in the constant volume chamber section. The large temperature differences that can be seen in Figure 98 most likely lead to mixing, as it is observed in the Constant Volume Chamber Axial Natural Convection section. This mechanism has no effect on the energy storage capacity since the fluid has the same amount of mass and energy inside the bladder chamber. The same cannot be said for the radial heat transfer effects discussed below.

Gas interaction with the bladder causes radial mixing to occur as explained in Chapter I. This radial mixing results in heat being from the gas to the accumulator shell, since the shell temperature is usually cooler than the fluid for both expansion and compression scenarios (see Figure 98). Similar to axial convection, the radial heat transfer causes a uniform temperature distribution. However, unlike axial convection, heat is now leaving the system, which could cause a significant impact on the energy storage capacity. Therefore, the

thermally boosted accumulator simulation must be modified to investigate the significance of this phenomenon.

The bladder chamber is the only part of the thermally boosted accumulator that acts like a normal accumulator. For this reason, heat transfer assumptions made for the standard accumulator are also applied to the bladder chamber section. Another reason for doing this is to ensure a fair comparison between the thermally boosted accumulator and the standard accumulator.

TBA Expansion at 10kW		
Work Out	385.4	(kJ)
Heat from Hot Heat Exchanger	485.2	(kJ)
Heat from Lump Mass	162.8	(kJ)
Heat Transferred to Ambient	97.3	(kJ)
Effected Fluid Mass by Heat Exchanger	53.3	(%)
Energy Storage Improvement	45.6	(%)
TBA Compression at 10kW		
Work In	389.1	(kJ)
Heat Into Cold Heat Exchanger	103.4	(kJ)
Heat Into Lump Mass	211.3	(kJ)
Heat Transferred to Ambient	202.9	(kJ)
Effected Fluid Mass by Heat Exchanger	48.6	(%)

Table 27: Thermally boosted accumulator energy and heat values with ambient heat transfer losses (10 kW operating conditions)

Some interesting results can be observed after running the thermally boosted accumulator model with the thermal losses. First, the pressure distribution is similar to that of the thermally boosted accumulator without the thermal losses (see Figure 94 and Figure 95).This is true because the bulk temperature of the accumulator is still operating around 300 K, making the operating condition nearly isothermal, as shown in Figure 100. Table 27 confirms

that even though 97.3 kJ of heat is lost to the ambient, the energy storage remains 385.4 kJ. This behavior is obtained by increasing the initial gas volume (which increases the amount of gas in the system) to ensure that the accumulator expands to about 100 bar at 29.5 L (the other 0.5 L is lost due to the presence of the metal foam mass in the constant volume chamber).

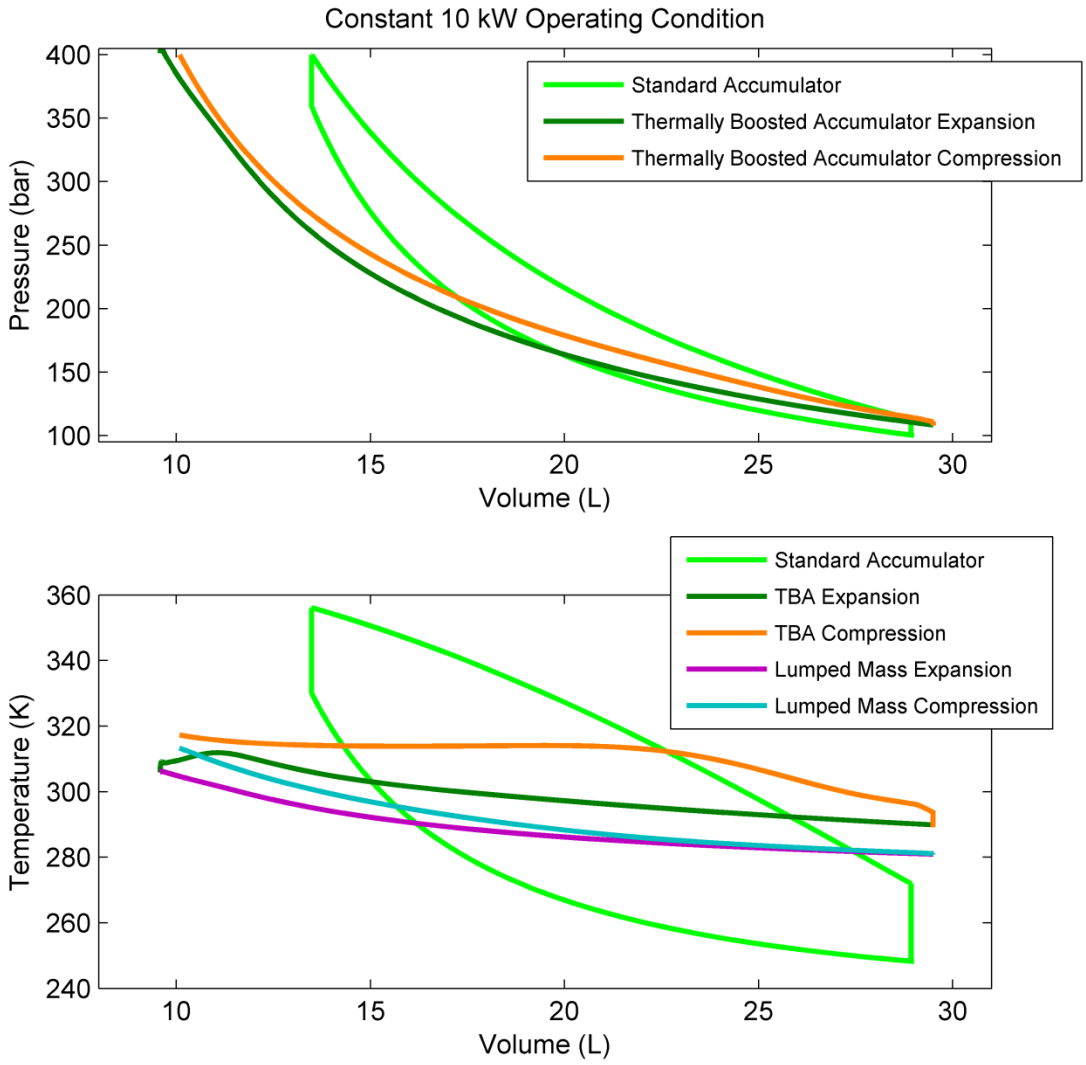

Figure 100: Thermally boosted accumulator pressure and bulk temperature behavior with thermal losses (10 kW operating condition)

Almost identical behavior can be observed in thermally boosted accumulator simulations with higher operating conditions (see Figure 101). The

main difference is that during the high rates of discharge not enough time passes for heat transfer to significantly affect the system during expansion. During compression, the decrease in volume causes an increase in temperature and results in more heat being transferred to the ambient. However, these effects appear negligible as the energy storage values remain the same (see Table 28).

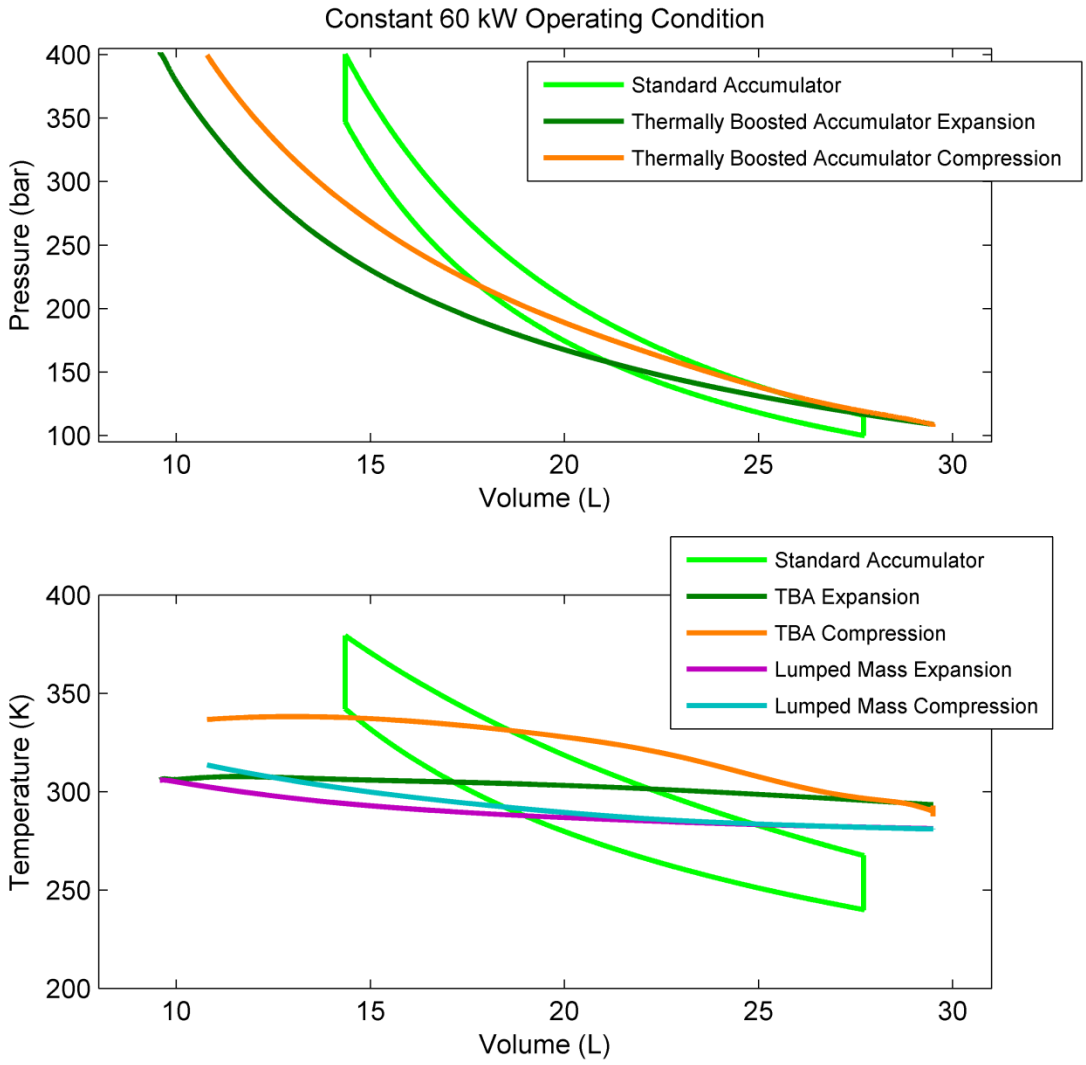

Figure 101: Thermally boosted accumulator pressure and bulk temperature behavior with thermal losses (60 kW operating condition)

TBA Expansion at 60kW		
Work Out	388.0	(kJ)
Heat from Hot Heat Exchanger	439.2	(kJ)
Heat from Lump Mass	164.1	(kJ)
Heat Transferred to Ambient	47.6	(kJ)
Effected Fluid Mass by Heat Exchanger	53.3	(%)
Energy Storage Improvement	62.8	(%)
TBA Compression at 60kW		
Work In	385.9	(kJ)
Heat Into Cold Heat Exchanger	155.2	(kJ)
Heat Into Lump Mass	211.9	(kJ)
Heat Transferred to Ambient	95.0	(kJ)
Effected Fluid Mass by Heat Exchanger	47.1	(%)

Table 28: Thermally boosted accumulator energy and heat values with ambient heat transfer losses (60 kW operating conditions)

Materials Selection for Thermal Improvement

The component materials can have significant impact on the thermal performance of the thermally boosted accumulator. In this section, material considerations are presented for high pressure gas containment, heat exchanger metal foams, and high temperature phase change materials. Figure 102 illustrates the many components of the proposed thermally boosted accumulator and the required materials.

Most commercially available accumulators are made of steel due to the material's high strength and low cost. Table 29 and Table 30 of Appendix C show various metals with sufficiently high tensile strength to be used in high pressure applications. From these tables it becomes apparent that low alloy steel is an excellent choice due to its economic cost and high volumetric heat capacity. This

is particularly true for the constant volume chamber with its shell acting as a heat sink (see Accumulator Shell Heat Sink section). However, two different materials may be required for the construction of the hot runner to account for the thermal considerations discussed below.

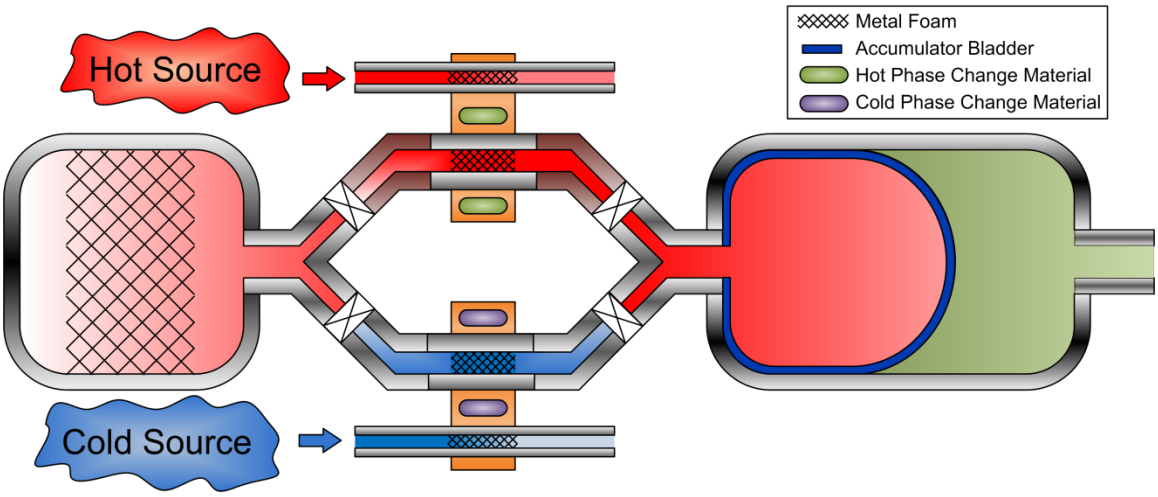

Figure 102: Thermally boosted accumulator final design

In the hot runner section, which houses the metal foam (see Figure 102), a material with thermal conductivity higher than steel should be used to improve the heat transfer rate between the fluid and the phase change material. Table 29 demonstrates that tungsten alloys or molybdenum alloys could be used to potentially increase the thermal conduction by more than 150% in comparison to steel. These materials should also be used in the cold runner pipe housing the metal foam. However, manufacturing pipes with these alloys is more costly due to higher melting temperatures and tensile strength.

The remaining section of the hot runner should be made from the materials with low thermal conductivity, in order to minimize heat leaving the hot heat exchanger area towards other sections of the thermally boosted accumulator. The materials listed in Table 30 indicate that alloys containing

nickel may be effective at lowering the conductivity. Among these metals we also have an iron based super-alloy with excellent cost, or a more exotic choice, such as a titanium alloy that offers better conductivity properties.

Selecting a material for metal foams is a difficult task, since materials with the best thermal conductivity, such as gold, silver, diamond, and copper, are extremely expensive and/or have low maximum operating temperatures. Table 32 shows some potential metals that can be used when the maximum temperature of the heat exchanger is below 550K. From these materials, a copper zirconium alloy appears to offer the best thermal conductivity and volumetric heat capacity. When higher temperatures are expected, a silicon metal foam appears to be the next best choice. Regardless of the material choices, the metal foams must be tested to understand how well they sustain the inertial forces of the fluid during operation of the accumulator. The impact of welding or co-sintering the metal foams to the outer pipe must also be considered.

Phase change materials should be used to successfully maintain the cold and hot heat exchangers at constant temperatures. This is possible since materials usually require a large amount of heat to switch between phases. Table 32 lists several metals that can be used for this purpose with the melting temperatures around 500 Kelvin. Among them, lead Babbitt metal alloy has an extremely high volumetric latent heat of fusion, making it an ideal choice. If this material is chosen 0.4 L (4 kg) of metal should be used to achieve 440 kJ of heat

storage. When higher temperatures are encountered, cadmium could be a practical choice as long as measures are taken to mitigate its toxic effects.

Selecting a phase change material for the cold heat exchanger presents a bigger problem due to the lack of substances that change phases at room temperature. Alfa Aesar and ChemSpider provided over 10,000 elements and their melting points, which was curated by Bradley et al. [**55**] and made available online. Most of the substances with melting temperatures around 300 K appear to be organic substances. One particular example is Malononitrile, $C_3H_2N_2$ which has an enthalpy of fusion of 150 kJ/kg. Using these types of compounds might be problematic due to the corrosion effects and/or low flash point temperatures.

Conclusion

In the beginning of this chapter we discuss how the initial design of the thermally boosted accumulator does not yield the expected energy storage improvements. This is mainly due to the one directional nature of convective heat transfer, which only allows heat to flow from the hot heat exchanger to the bladder chamber. Operating in this manner leads to isentropic conditions in the constant volume chamber causing the pressure to drop rapidly. The working fluid selected further exacerbates this problem due to its low heat capacity. To mitigate these problems we suggest two possible accumulator modifications.

The first design modification is to integrate a throttle to generate oscillating fluid motion back towards the constant volume chamber. Simulation results showed that throttling the accumulator induces high frequency fluid motions

between control volumes without generating a sufficiently large overall backward flow. To fully utilize the advantages of throttling, we propose the use of a dissipative device to convert the fluids kinetic energy into thermal energy at the end of the constant volume chamber.

The next design features a more passive approach to improving the thermodynamics of the fluid. This is achieved with the addition of a metal foam, which effectively increases the heat capacity of the system. This approach yields significant improvements to the energy storage capacity of the accumulator and stabilizes its operation regardless of power demand. This concept is further improved by connecting the metal foam to the constant volume chamber shell effectively increasing the heat capacity of the system.

Some heat transfer considerations are made with regards to the natural convective heat transfer unaccounted for by the one-dimensional computational fluid dynamics code. We concluded that most of these modes of heat transfer only cause a more uniform temperature distribution. The exception is the heat transfer between the fluid and the bladder chamber, which causes a significant temperature drop. To overcome this problem, the constant volume chamber is increased in size to increase the fluid mass. From the simulation results we observe that increasing the fluid mass is extremely effective at reducing the impact of heat loss to the ambient.

Lastly, we present a preliminary analysis for the material selection process for various components of the thermally boosted accumulator. In particular, special care should be taken when selecting metal foam material due to possible

maximum operating temperature issues. High pressure pipes housing the heat exchanger may be manufactured using metals with high thermal conductivity. It is also recommended to select materials for the hot runners with low thermal conductivity to minimize heat losses towards the other accumulator parts.

CHAPTER VII

Conclusion

One of the greatest challenges in today's world of automotive engineering is the ongoing pursue to drastically improve vehicle fuel economy and engine emissions. Hybrid vehicles play an important role in this challenge, facilitating the decrease of fuel consumption and carbon dioxide discharge. In particular, hydraulic hybrids are the powertrain of choice for heavy duty vehicles due to their notable system efficiency, low cost and high power density. In such powertrain, hydraulic accumulators are used to store excess energy by compressing a fluid, which is usually a nitrogen gas. However, these accumulators have poor energy storage capacity as a result of the nonlinear thermodynamics behavior of the working gas. In addition, heat transfer exacerbates this condition even further by introducing hysteresis between the expansion and compression cycles.

To understand the theoretical potential of storing energy via fluid compression, we perform a fundamental thermodynamic analysis presented in this thesis. This analysis illustrates that isobaric operation yields the best possible energy storage capacity. To achieve this behavior, heat is added to the accumulator fluid during the expansion, while heat is removed from the system during the compression. Our simulation of this process yields significant energy

storage improvement of the hydraulic hybrid system even though the isobaric operation is maintained only temporarily, limited by the available heat transfer rates and attainable temperatures of the heat source and heat sink. An energy storage improvement of 107% is shown as the theoretical limit for an accumulator with a 500 K constant temperature heat source.

The key intellectual contribution of this dissertation is the presented modeling of an innovative device, the thermally boosted accumulator. Our modeling of the proposed system is done via a specialized one-dimensional computational fluid dynamics code with advanced thermodynamic state models and innovative heat exchanger metal foam. This code is essential to capture the high density properties of the gas, and predict the convective heat transfer to the fluid due to its low velocity motion. The detailed analysis of the thermodynamics and heat transfer behavior of the thermally boosted accumulator illustrates the strengths and weaknesses of this device. The new accumulator design is able to improve the energy storage capacity by more than 60% over current systems, with consistent performance across all power demand levels.

Future Work

In the future work we plan to study the heating and cooling circuits required to provide a constant temperature heat source and heat sink to the accumulator. The low temperature side of the heat exchanger most likely will need to be cooled using the engine cooling system. Another possible solution that is worth investigating in the future is the idea of routing ambient air that flows

around the vehicle into the accumulator area, such that the constant volume chamber shell and the cold runner heat exchanger can be cooled using the forced convection. This design may also require the use of heat exchanger fins to increase the heat transfer surface area.

To maintain the high temperature of the other side of the heat exchanger, we propose a future study of the use of hot coolant coming from the engine. The other possibility is to use exhaust gases as a means to heat the accumulator. This method will most likely require the use of a phase change material to absorb the exhaust thermal energy since the accumulator expansion will not coincide with the period in which hot gases are produced by the engine. The rate of heat transfer between the phase change material and its container must be studied to understand how quickly heat can be withdrawn.

Exhaust and coolant temperatures acquired during engine testing, as well as vehicle speed information, can be used to model the cooling and heating circuit. These models will then have to be connected to a thermally boosted accumulator and hybrid vehicle simulation to provide a realistic estimate of the accumulator's true potential. Other applications of this device should be considered including its use for stationary energy storage.

APPENDIX A – Energy Storage Results Summary

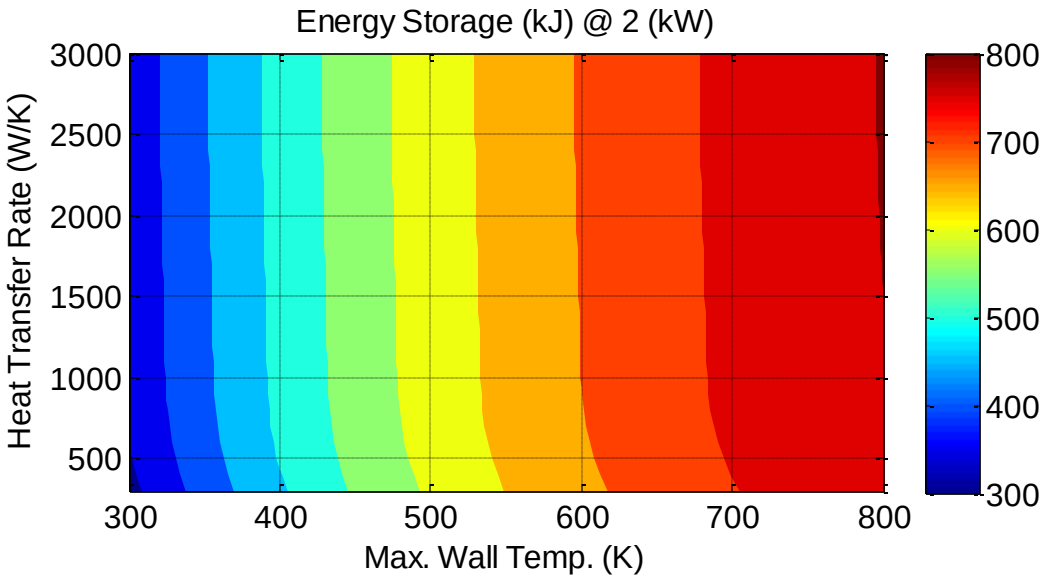

Figure 103: Accumulator energy storage for a power demand of 2 (kW)

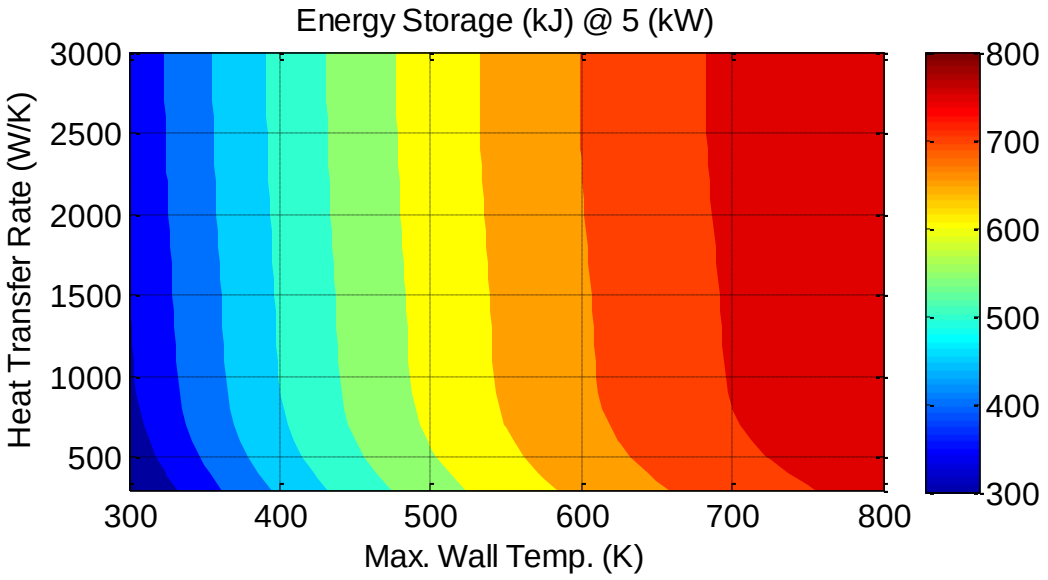

Figure 104: Accumulator energy storage for a power demand of 5 (kW)

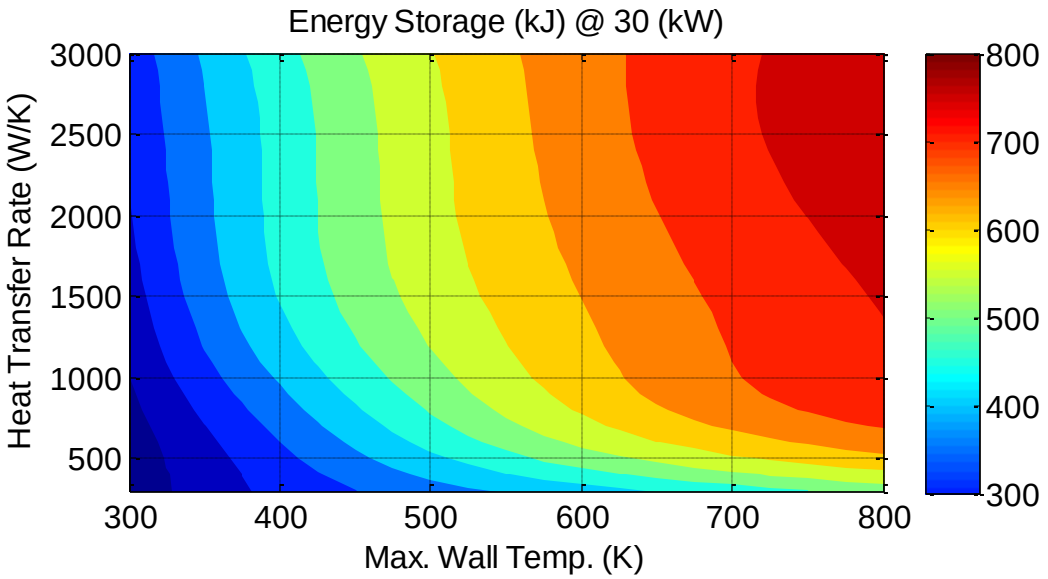

Figure 105: Accumulator energy storage for a power demand of 30 (kW)

APPENDIX B – Accumulator Thermal Efficiency

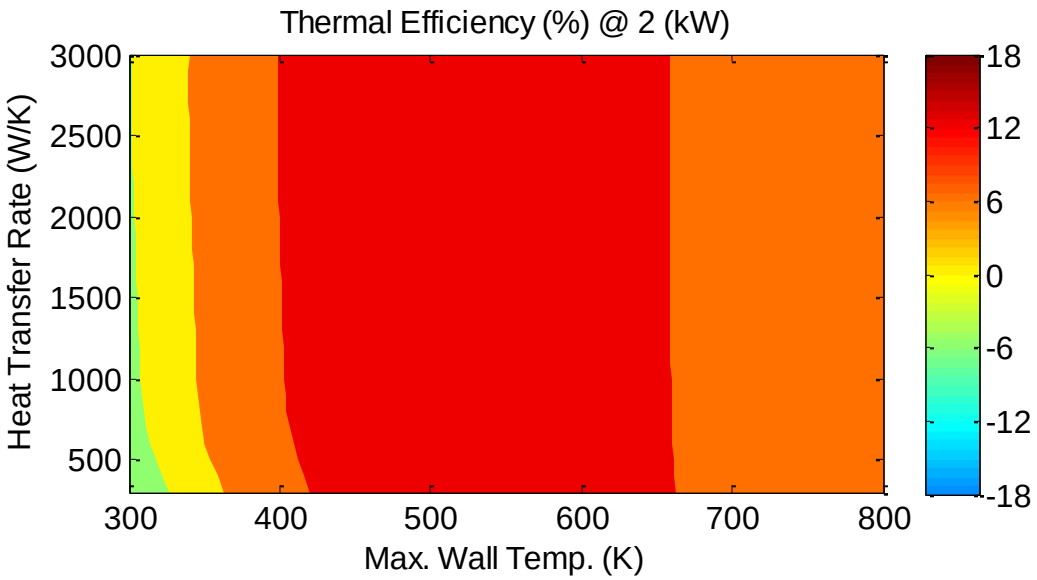

Figure 106: Exhaust work efficiency for a power demand of 2 (kW)

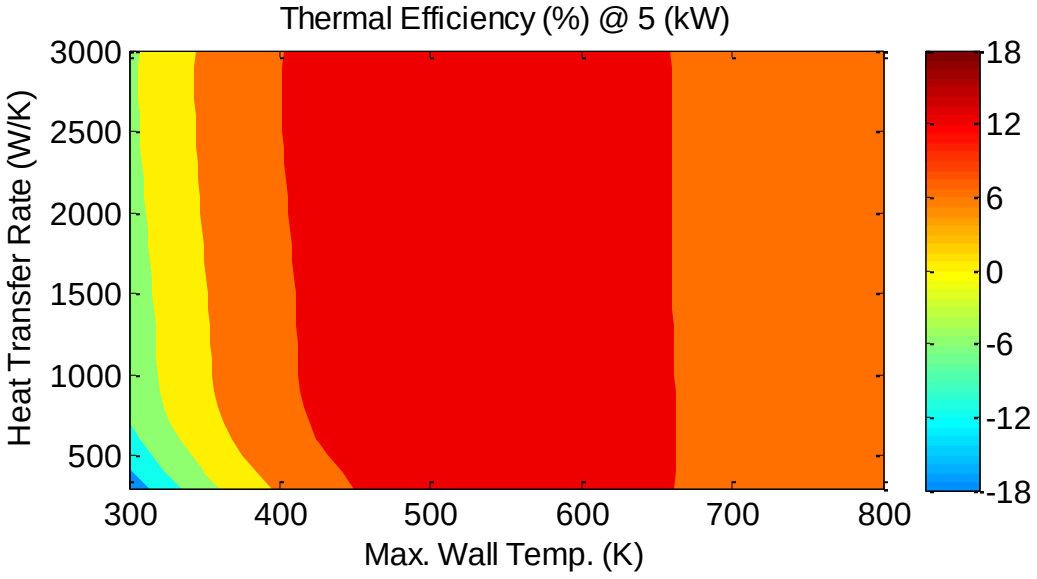

Figure 107: Exhaust work efficiency for a power demand of 5 (kW)

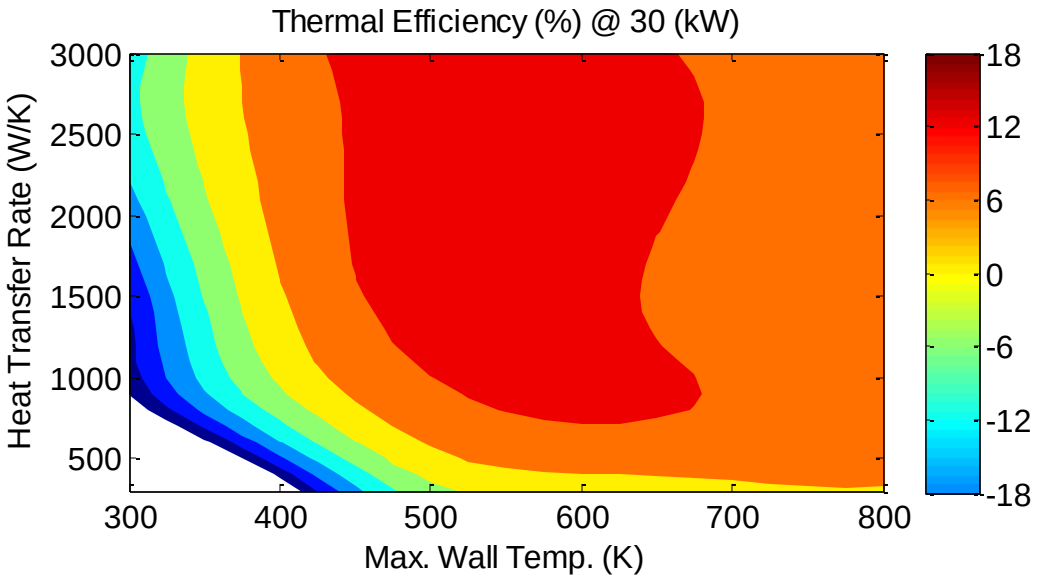

Figure 108: Exhaust work efficiency for a power demand of 30 (kW)

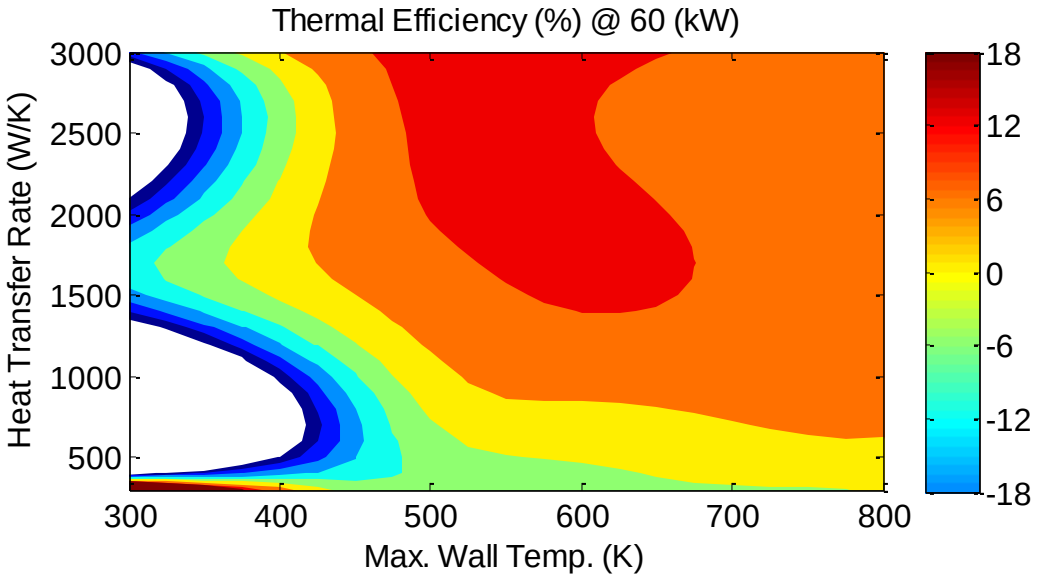

Figure 109: Exhaust work efficiency for a power demand of 60 (kW)

APPENDIX C – Material Tables

	Price ($/kg)	Density (kg/m^3)	Thermal Conductivity (W/m-K)	Specific Heat Capacity (J/kg-K)	Volumetric Heat Capacity (J/L-K)	Max. Service Temperature (K)	Tensile Strength (MPa)
Tungsten-Ni-Cu-Mo alloy	22.90	16950	90	135	2290	1205	968
Molybdenum alloy	26.65	10200	138	265	2700	1361	968
Pure Tungsten	23.40	19350	173	138	2670	1290	1860
Low Alloy Steel	1.14	7850	49	450	3530	927	908

Table 29: Possible containment materials with high thermal conductivity [52]

	Price ($/kg)	Density (kg/m^3)	Thermal Conductivity (W/m-K)	Specific Heat Capacity (J/kg-K)	Volumetric Heat Capacity (J/L-K)	Max. Service Temperature (K)	Tensile Strength (MPa)
Titanium alloy	54.5	4450	4.8	555	2470	778	1030
Cobalt base-super alloy	21.3	8050	9	453	3640	1297	925
Nickel-Cr-Fe	20.6	8250	11.25	458	3770	1623	723
Stainless Steel	8.85	7960	11.75	450	3580	1100	605
Iron-base super alloy	5.75	7940	13	471	3740	1673	943

Table 30: Possible containment materials with low thermal conductivity [52]

	Price ($/kg)	Density (kg/m^3)	Thermal Conductivity (W/m-K)	Specific Heat Capacity (J/kg-K)	Volumetric Heat Capacity (J/L-K)	Max. Service Temperature (K)	Tensile Strength (MPa)
Molybdenum alloy 366	25.85	1190	115	215	2560	1362	825
Copper-zirconium	5.23	8945	394	385	3440	598	310
Cobalt	33.2	8850	96	440	3890	593	1135
Silicon	12.11	2330	160	691.5	1610	828	173
Tungsten	23.4	19350	172.5	138	2670	1291	1860
Iron	0.64	7870	75.5	450	3540	608	263
Duralcan Aluminum alloy	7.26	2770	192.5	837.5	2320	563	325

Table 31: Material selections for metal foams [52]

	Price ($/kg)	Density (kg/m^3)	Thermal Conductivity (W/m-K)	Specific Heat Capacity (J/kg-K)	Latent Heat of Fusion (kJ/kg)	Volumetric Latent Heat (kJ/L)	Melting Temperature (K)
Lead, Babbitt Metal alloy	3.01	10000	24	150	110	1103	527.5
Lead tin alloy	4.72	10300	37	160	31.5	323	503.0
Lithium	87.15	535	77.5	3525	435	233	452.5
Selenium	12.97	4800	1.3	330	60	324	489.5
Tin	13.55	7295	60.7	222	55	438	505.0
Cadmium	3.93	8645	97	232.5	42	475	592.5

Table 32: Possible phase change materials for high temperature heat storage [52]

REFERENCES

[1] Z. Filipi, L. Louca, B. Daran, C-C. Lin, U. Yildir, B. Wu, M. Kokkolaras, D. Assanis, H. Peng, P. Papalambros, J. Stein, D. Szkubiel, and R. Chapp, "Combined optimisation of design and power management of the hydraulic hybrid propulsion system for the 6X6 medium truck," *International Journal Heavy Vehicle Systems*, vol. 11, pp. 372-402, 2004.

[2] Z. Filipi and Y. J. Kim, "Hydraulic Hybrid Propulsion for Heavy Vehicles: Combining the Simulation and Engine-in-the-Loop Techniques to Maximize the Fuel Economy and Emission Benefits," in *Les Rencontres Scientifiques de l'IFP - Advances in Hybrid Powertrains*, 2008.

[3] F. T. Tavares, R. Johri, and Z. Filipi, "Simulation study of advanced variable displacement engine coupled to power-split hydraulic hybrid powertrain," in *Proceedings of the ASME Internal Combustion Engine Division Spring Technical Conference*, Milwaukee, 2009.

[4] B. Wu, C-C. Lin, Z. Filipi, H. Peng, and D. Assanis, "Optimal power management for a hydraulic hybrid delivery truck," *Vehicle System Dynamics*, vol. 42, pp. 23-40, 2004.

[5] A. H. Levine and D. R. Otis, "Free convection in a piston cylinder enclosure with sinusoidal piston motion," in *ASME National Heat Transfer Conference*, Orlando, 1980, pp. 73-77.

[6] A. Pourmovahed and D. R. Otis, "Experimental thermal time-constant correlation for hydraulic accumulators," *Journal of Dynamic Systems, Measurement and Control, Transactions ASME*, vol. 112, pp. 116-121, 1990.

[7] D. R. Otis and A. Pourmovahed, "An algorithm for computing nonflow gas processes in gas springs and hydropneumatic accumulators," *Journal of Dynamic Systems, Measurement and Control, Transactions ASME*, vol. 107, pp. 53-9, 1985.

[8] A. Pourmovahed, "Modeling the transient natural convection in gas-filled, variable volume cylindrical enclosures with applications to hydraulic accumulators," University of Wisconsin-Madison, Ph. D. Thesis 1985.

[9] A. Pourmovahed, N. H. Beachley, and F. J. Fronczak, "Modeling of a hydraulic energy regeneration system. Part I. Analytical treatment," *Journal of Dynamic Systems, Measurement and Control, Transactions of the ASME*, vol. 114, pp. 155-159, 1992.

[10] P. Y. Li, J. D. Van, and C. Sancken, "Open accumulator concept for compact fluid power energy storage," in *Proceedings of the ASME International Mechanical Engineering Congress and Exposition*, vol. 4, 2008, pp. 127-140.

[11] A. Pedchenko and E. Barth, "Design and validation of a high energy density elastic accumulator using polyurethane," in *ASME/Bath Fluid Power Symposium: Pump Design, Analysis and Appliation*, 2009.

[12] C. L. Gray and K. H. Hellman, "Accumulator Engine," Patent 5,579,640, December 3, 1996.

[13] S. K. Andersen, H. Carlsen, and P. G. Thomsen, "Control volume based modelling in one space dimension of oscillating, compressible flow in reciprocating machines," *Simulation Modelling Practice and Theory*, vol. 14, pp. 1073-86, 2006.

[14] D. Winterbone and R. Pearson, *Theory of Engine Manifold Design*.: Professional Engineering Publishing, 2000.

[15] H. W. Xiang and U. K. Deiters, "A new generalized corresponding-states equation of state for the extension of the Lee-Kesler equation to fluids consisting of polar and larger nonpolar molecules," *Chemical Engineering Science*, vol. 63, pp. 1490-6, 2008.

[16] W. Lu, C. Y. Zhao, and S. A. Tassou, "Thermal analysis on metal-foam filled heat exchangers. Part I: Metal-foam filled pipes," *International Journal of Heat and Mass Transfer*, vol. 49, pp. 2751-61, 2006.

[17] W. F. Riley, L. D. Sturges, and D. H. Morris, *Mechanics of materials*.: John Wiley, 1999.

[18] G. Eichelberg, "Some new investigations on old combustion engine problems," *London Engineering*, no. 148, pp. 463-547, 1934.

[19] W. Nusselt, "Die Warmeubergang in den Verbrennugskraftmaschinen," *Z. Ver. Dt. Ing.*, no. 67, pp. 692-708, 1923.

[20] J. E. Bennethum, O. A. Uyehara, P. S. Myers, and V. D. Overbye, "Unsteady heat transfer in engines," *SAE transactions*, p. 70, 1961.

[21] W. D. Annand and T. H. Ma, "Instantaneous heat transfer rates to the cylinder head surface of a small compression-ignition engine," *Proceedings of the Institution of Mechanical Engineers*, vol. 185, pp. 976-987, 1970.

[22] G. Woschni, "Universally applicable equation for instantaneous heat transfer coefficient in internal combustion engine," *Society of Automotive Engineers -- Papers*, no. 670931, pp. 3065-3077, 1967.

[23] B. Lawton, "Effect of compression and expansion on instantaneous heat transfer in reciprocating internal combustion engines.," *Proceedings of the Institution of Mechanical Engineers, Part A: Power and Process Engineering*, vol. 20, pp. 75-186, 1987.

[24] H. Pfriem, "Periodic heat transfer at small pressure fluctuations," National Advisory Committee for Aeronautics, Technical Memorandum 1048, 1943.

[25] AA. Kornhauser and J. S. J.L., "Application of a complex Nusselt number to heat transfer during compression and expansion," *Transactions of the ASME. Journal of Heat Transfer*, vol. 116, pp. 536-42, 1994.

[26] K. P. Lee, "A simplistic model of cyclic heat transfer phenomena in closed spaces," in *Proceedings of the 18th Intersociety Energy Conversion Engineering*, 1983, pp. 720-723.

[27] R. Courant, K. Friedrichs, and H. Lewy, "Über die partiellen Differenzengleichungen der mathematischen Physik," *Mathematische Annalen*, vol. 100, pp. 32-74, 1928.

[28] R. W. Fox, A. T. McDonald, and P. J. Pritchard, *Introduction to Fluid Mechanics*, 6th ed.: John Wiley & Sons, Inc., 2004.

[29] L. F. Moody, "Friction factors for pipe flow," *Transactions of the ASME*, vol. 66, no. 8, pp. 671-684, November 1944.

[30] H. D. Kühl and S. Schults, "Modelling of thermal regenerator losses due to axial flow dispersion," in *Proceedings of the 7th International Conference on Stirling Cycle Machines*, 1995.

[31] D. Gedeon, "Numerical advection errors in stirling cycle nodal analyses," in *Proceedings of the Intersociety Energy Conversion Engineering Conference*, 1984, pp. 1898-1904.

[32] (2010, November) Wikipedia. [Online]. http://en.wikipedia.org/wiki/Runge%E2%80%93Kutta_methods#Explicit_Runge.E2.80.93Kutta_methods

[33] P. D. Lax, "Weak solutions of nonlinear hyperbolic equations and their numerical computation," *Communications on Pure and Applied Mathematics*, vol. 7, pp. 159-193, 1954.

[34] P. D. Lax and B. Wendroff, "Difference schemes for hyperbolic equations with high order accuracy," *Communications on Pure and Applied Mathematics*, vol. 17, pp. 381-398, 1964.

[35] R. D. Richtmyer, "Survey of difference methods for non-steady fluid dynamics," National Center for Atmospheric Research, Colorado, 1962.

[36] R. Courant, E. Isaacson, and M. Rees, "On the solution of non-linear hyper differential equations by finite differences," *Communications on Pure and Applied Mathematics*, vol. 5, pp. 243-249, 1952.

[37] E. F. Toro, *Riemann Solvers and Numerical Methods for Fluid Dynamics*.: Springer, 2009.

[38] R. Liska and B. Wendroff, "Composite schemes for conservation laws," *SIAM Journal on Numerical Analysis*, vol. 35, pp. 2250-2271, 1998.

[39] (2005) The Engineering ToolBox. [Online]. http://www.engineeringtoolbox.com/spesific-heat-capacity-gases-d_159.html

[40] C. R. Hammond, *The Elements*.: CRC Press, 2000.

[41] (2011, March) Wikipedia. [Online]. http://en.wikipedia.org/wiki/Argon#Occurrence

[42] C. Tegeler, R. Span, and W. Wagner, "A new equation of state for argon covering the fluid region for temperatures from the melting line to 700 K at pressures up to 1000 MPa," *Journal of Physical and Chemical Reference Data*, vol. 28, pp. 779-850, 1999.

[43] NB. Vargaftik, *Tables on the thermophysical properties of liquids and gases: in normal and dissociated states*, 2nd ed.: Hemisphere Pub. Corp., 1975.

[44] T. Kunugi, K. Muko, and M. Shibahara, "Ultrahigh heat transfer enhancement using nano-porous layer," in *Eurotherm 75: Microscale Heat Transfer 2*, vol. 35, 2004, pp. 531-542.

[45] K. Boomsma, D. Poulikakos, and F. Zwick, "Metal foams as compact high performance heat exchangers," *Mechanics of Materials*, vol. 35, pp. 1161-76, 2003.

[46] K. Vafai and CL. Tien, "Boundary and inertia effects on flow and heat transfer in porous media," *International Journal of Heat and Mass Transfer*, vol. 24, pp. 195-203, 1981.

[47] VV. Calmidl and RL. Mahajan, "Forced convection in high porosity metal foams," *Transactions of the ASME. Journal of Heat Transfer*, vol. 122, pp. 557-65, 2000.

[48] V. V. Calmidi, "Transport phenomena in high porosity fibrous metal foams," Univesity of Colorado, Ph.D. Thesis 1998.

[49] C. Y. Zhao, "Thermal transport phenomena in Porvair metal foams and sintered beds," University of Cambridge, Ph.D. Thesis 2001.

[50] K. Boomsma and D. Poulikakos, "On the effective thermal conductivity of a three-dimensionally structured fluid-saturated metal foam," *International Journal of Heat and Mass Transfer*, vol. 44, pp. 827-36, 2001.

[51] A. A. Zukauskas, "Convective heat transfer in cross-flow," in *Handbook of Single-Phase Convective Heat Transfer*, S. Kakac and R. K. Shah, Eds. New York: Wiley, 1987.

[52] CES EduPack Version 6.2.0, 2011.

[53] V. T. Morgan, "The overall convective heat transfer from smooth circular cylinders," *Advances in heat transfer*, vol. 11, pp. 199-264, 1975.

[54] I. Catton, "Natural convection in enclosures," in *Proceedings 6th International Heat Transfer Conference*, vol. 6, 1978, pp. 13-31.

[55] JC. Bradley, A. Lang, and A. Williams. (2011, April) Open Melting Point Data. [Online]. http://lxsrv7.oru.edu/~alang/meltingpoints/download.php